Production and Measurement of H_2 in Rovibrationally Excited States

By

Ilhan Candan

A thesis submitted to University College London
in partial fulfilment of the requirements for the
degree of Master of Philosophy

Department of Physics and Astronomy
University College London
January 8, 2016

I, Ilhan Candan, confirm that the work presented in this thesis is my own. Where information has been derived from other sources, I confirm that this has been indicated in this thesis.

Signed ..... Date .....

Abstract

This work describes experiments conducted to achieve a stimulated Raman pumping (SRP) scheme for the state-selective detection of decelerated H_2 molecules from a molecular beam. An optical Stark deceleration technique is proposed consisting of trapping H_2 molecules in optical lattices. To achieve SRP, two separate experiments were carried out: a $(2+1)$ resonance enhanced multiphoton ionization (REMPI) scheme and a coherent anti-Stokes Raman spectroscopy (CARS) scheme. The $(2+1)$ REMPI experiment was conducted in a non-equilibrium DC glow discharge where ro-vibrationally excited H_2 molecules at $v = 1$ are produced. We successfully measure the H_2 $(2+1)$ REMPI spectra at $v = 1$ vibrational state in this non-equilibrium discharge. In a separate CARS experiment, in which one of the lattice beams is used as a Stokes beam, we verify the pump laser wavelength for the SRP scheme. The outcome of both CARS and REMPI experiments shows good verification of the pump and probe wavelengths respectively. Furthermore, radial temperature measurements for H_2 molecules are conducted in the non-equilibrium DC glow discharge using the $(2+1)$ REMPI process. In this experiment, radial vibrational temperature of hydrogen molecules is measured to be over thousands of Kelvin for the first time. The rotational and translational temperatures are determined to be hundreds of Kelvin in these measurements as well.

Contents

List of Tables

List of Figures

Acknowledgements

Firstly, I would like to thank my supervisors; Dr. Jonathan Underwood and Professor Peter Barker for their support and insightful discussions about my research. Their enthusiasm and guidance have been invaluable to me throughout my research at UCL.

Secondly, I would like to express my gratitude to my colleagues in our research group. A special thanks should go to Dr. James Millen for his help with my work and patience with proofreading my thesis. Also, a huge thanks goes to Lia Han for all her support and encouragement. I should not forget both present and former group members; Dr. Peter Edmunds, Dr. Alexandros Gerakis, Manish, Giacomo... Thank you all!

I should also mention my lunch friends, thank you for making my time at UCL joyful. I highly encourage them to continue having our customary dinners in our favourite Turkish restaurant in London. Additionally, I want to thank my dear flatmates; Yi-da(Sting), Shadia, Wei... for making homelike environment and supporting me during my studies. Another thanks is for all my Turkish friends for organizing enjoyable gatherings, especially to those in my department Hilal and Meliz for their encouragement and support. Last, but certainly not least, a very special thanks goes to Zehra Ersahin for always being there for me and helping me go through everything including my hardest times.

Finally, I would like to express my deepest gratitudes and love to my family. I thank my dear cousin Jandan for not making me homesick here far away from home. I certainly would not get to this stage without my family's love and support; emotionally or otherwise.

Dedicated to my Mother.

Chapter 1

Introduction

1.1 Motivation

The control of the translational motion of atoms, molecules and ions [1, 2], through the use of electric, magnetic [3, 4] or optical [5, 6] fields and mechanical means such as a rotating nozzle [7, 8], is an active area of research. Such control allows the creation of highly monoenergetic beams of atoms and molecules with low energy for applications involving collisional and reactive scattering experiments [9, 10], atomic nano-fabrication [11, 12] and atomic optics [13]. In the case of molecules, deceleration from a high-speed molecular beam would achieve such control. Such a deceleration of molecular beams would provide a tool for studying ultracold chemistry, long-range atomic and molecular interactions [14], and tunnelling and resonance phenomena, which are usually disguised by the wide energy spread of typical molecular beams [2, 15, 16]. Chemical reactions are governed by both the internal state and the translational energy of the active species. Although considerable work has gone into using the optical phase and intensity of laser fields to manipulate internal motion [14, 17], no common optical techniques for controlling molecules' translational motion over a wide range have been demon-

strated. Optical Stark deceleration is a promising technique for manipulating the translational motion of molecules and is the focus of our current work.

1.2 Optical Stark deceleration

Optical Stark deceleration is a technique employing intense, pulsed, optical fields to rapidly decelerate molecules emitted from a beam source. In this technique a far detuned optical field and the induced dipole moment of a molecule interact resulting in a potential well. In an optical Stark deceleration experiment, two nearly counter-propagating intense laser pulses (with an intensity greater than 10^{11} Wcm^{-2}) are spatially overlapped to create an interference pattern. The resulting interference pattern is collinear with the molecular beam propagation direction so as to produce a deep periodic optical lattice potential. In addition, a probe beam, which is orthogonal to the propagation direction of the molecular beam and lattice beams, is needed to detect the molecules in the lattices. This is illustrated in figure 1.1.

In this scheme, the potential experienced by a polarisable particle is quasi-electrostatic [18] and given by $U = -\frac{1}{2}\alpha_{\text{eff}} \mid E \mid^2$. This trapping potential is very general and can be applied to any polarisable particle whether that can be an atom, molecule or some mesoscopic particle. The force on a particle in this potential, $F = -\nabla U$, is dependent on the intensity gradient of the optical field, which stems from the interference pattern of two intense, nearly counter-propagating laser beams. This results in the intensity gradients being much steeper than in a single beam field. Overlapping the interference pattern with polarisable particles creates a periodic one-dimensional potential along the z direction, known as an optical lattice (figure 1.1, inset), of the form:

$$U(z,t) = -\frac{2\alpha_{\text{eff}}}{\epsilon_0 c}\sqrt{[I_1(t)I_2(t)]}\cos^2(\frac{1}{2}[kz - \Delta\omega t]), \tag{1.1}$$

where $k = \frac{4\pi \sin\varphi}{\lambda}$ is the lattice wavenumber, λ is the wavelength of the light used, φ is the half-

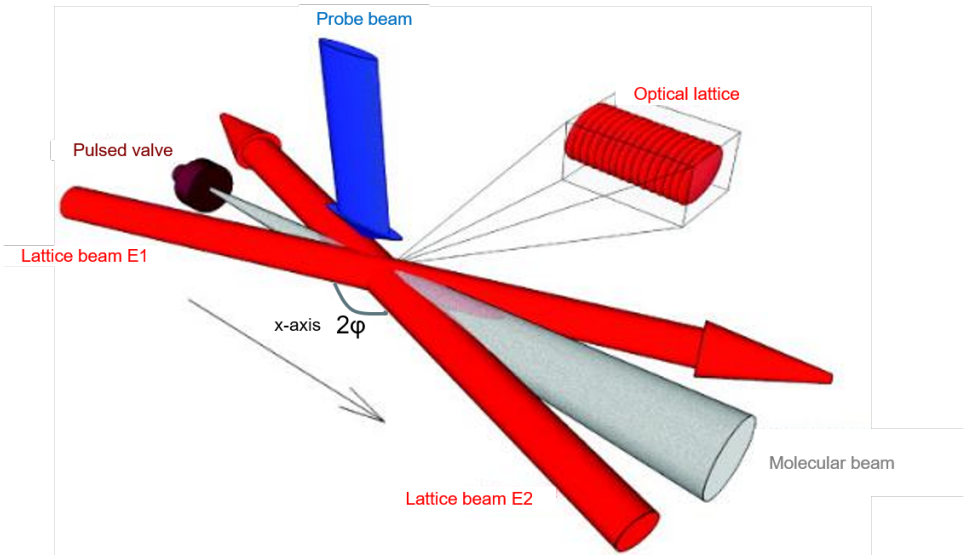

Figure 1.1: The creation of an optical lattice, produced by the interference of two nearly counter-propagating optical fields E_1 and E_2, for deceleration of molecules in a molecular beam. Also shown is a probe laser that is used to detect the velocity changes induced by the lattice (figure taken from reference [19]).

angle between the two beams, $\Delta\omega = \omega_2 - \omega_1$ is the angular frequency difference between the two lattice beams, α_{eff} is the polarizability of the particle and $I_{1,2}(t)$ are the beam intensities. A non-zero frequency difference creates a travelling lattice with a velocity $v_{\text{L}} = \frac{\Delta\omega}{k}$. By varying $\Delta\omega$ one can control motion of lattice and confined particles.

Molecular deceleration can be achieved using either a constant-velocity lattice generated with a fixed $\Delta\omega$ [8] or a decelerating lattice which is produced by rapidly sweeping, or chirping, the frequency difference between two beams [20, 21]. Previous experiments on laser deceleration and acceleration of supersonic beams of molecules (for instance, deceleration of nitric oxide [8, 22]) deployed a deep lattice potential travelling at a constant velocity (with fixed $\Delta\omega$) which was half that of the beam velocity. Deceleration and acceleration of a molecular beam was achieved by exploiting a half oscillation in the deep optical potential in which the trapped

molecules undergo a half phase-space rotation. The final velocity was determined by the potential depth, with the gradient of the potential determining the magnitude of the force. Therefore, tailoring the final velocity with this technique necessitates absolute control over both the intensity and duration of the lattice beams. This is technically challenging. The challenge is also to control the frequency, even for fixed $\Delta\omega$. In addition, the deep potential implies that the final velocity spread of the decelerated packet cannot be narrower than the width of the original molecular beam and the large intensity prevents its use on easily ionized species. On the other hand, controlling the velocity is simpler when using an accelerating/decelerating lattice [23] as the beam intensity and duration stay fixed whereas only their relative frequency $(\Delta\omega)$ is changed (chirped). A chirped optical lattice is generated by rapidly changing the frequency difference between two laser beams which results in an acceleration or deceleration of the lattice. Particle acceleration with a chirped lattice is achieved by trapping particles in the potential wells of the lattice and carrying them with potential as it accelerates. In order to do this the lattice is switched on with a velocity equal to that of the particles and than accelerates them to the desired final velocity. The same principle applies to a decelerating lattice as well where the lattice is switched on with a velocity equal to the that of the particles and than decelerated to rest in the lab frame. As this method does not rely on the oscillatory motion of the trapped particles, acceleration or deceleration can be carried out over longer durations and requires lower intensities. In addition, employing a chirped lattice removes the fundamental limit on the velocity width of the acceleration/deceleration distribution which prohibits the use of constant velocity acceleration in certain applications [24]. Since the decelerating lattice approach is more advantageous compared to the constant-velocity lattice approach, we use the former. By using the chirping lattice approach, argon atoms are accelerated from rest up to 191 m s^{-1} with an acceleration of 10^8 times that of gravity within our research group [23]. In this study, argon atoms were initially laser cooled to a temperature of 70 μK. The acceleration took place over a distance of 10 μm and a timescale of 70 ns. This state of the art chirped optical Stark

acceleration/deceleration technique is unique and has been developed by our research group at UCL.

A significant requirement to achieve the decelerating lattice is the ability to produce two strong optical fields, the intensity and frequency of which can be independently controlled over hundreds of nanoseconds. Furthermore, we require their intensities to remain sufficiently low so that they do not ionise or powerfully perturb the internal states of the particles. Such a laser system has been developed by our research group that is able to temporarily produce flat-top intensity profiles (10^{14} Wm^{-2}) and frequency chirps up to 1.1 GHz [25]. The amplifier in the laser system is capable of producing pulse energies of 700 mJ for μs pulse durations. At pulse duration $100-200$ ns the output pulse energies are typically $350-400$ mJ. Focusing these output pulses to beam waists of 100 μm or less generates intensities on the order of 10^{14} Wm^{-2}.

In addition, we require a probe which is able to detect the decelerated molecules in the optical lattices. However, probing the decelerated molecules in the molecular beam is highly challenging because the volume of the optical lattice is relatively small compared to the molecular beam volume. This difficulty arises from the fact that there is a background ionization signal caused by the probe beam ionising molecules from outside of the optical lattice but in the probe beam's path, see figure 1.2a. This is because all molecules in the molecular beam are at $v = 0$ vibrational state and ground rotational state as the temperature in the molecular beam is around 1 K. To overcome this challenge, one can tag only the molecules in the optical lattice by excitation to a specific excited rovibrational quantum state with subsequent detection via state-selective ionisation. Tagging process essentially means preparing molecules in an excited rovibrational state, thus they would be distinguished from the rest in the molecular beam. To merely tag the molecules in the optical lattices, we can employ one of the non-linear optical approaches. Stimulated Raman pumping (SRP) is widely used as a method to prepare molecules in specific rovibrational states. In SRP, two laser beams are used whose energy difference is tuned to a Raman allowed transition.

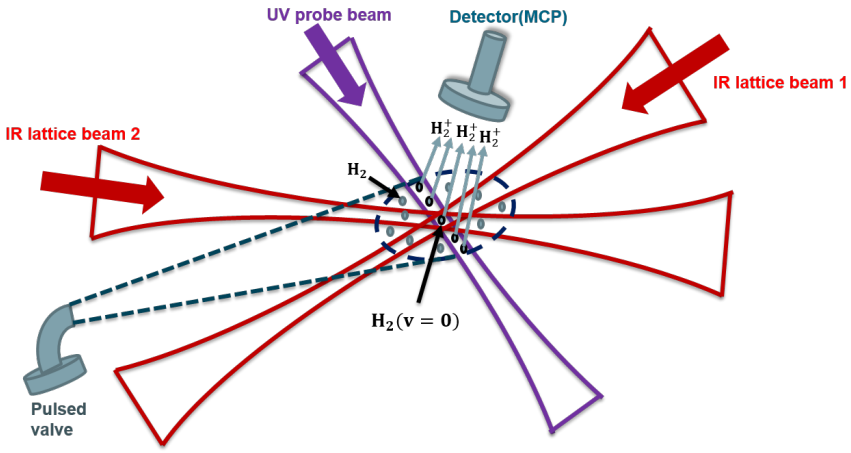

(a) Probing H_2 molecules at $v = 0$.

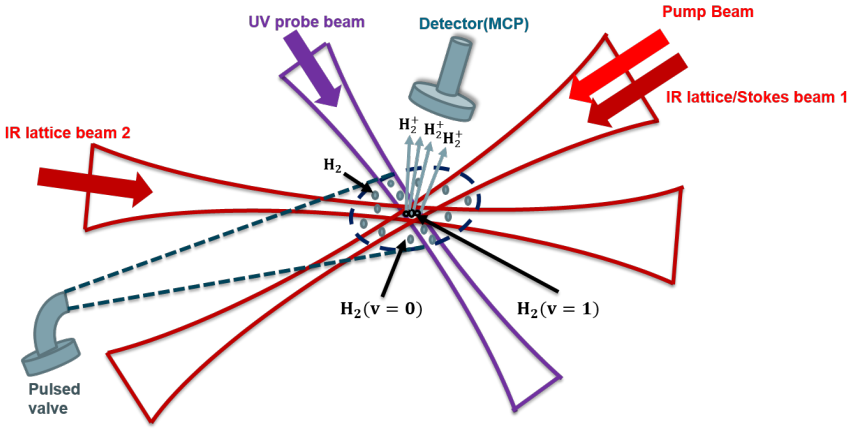

(b) Probing only the tagged H_2 molecules at $v = 1$ in the optical lattice.

Figure 1.2: (a) The position of the H_2 molecular beam with respect to the pulsed optical lattices. The UV probe beam, used to ionize and detect the H_2 molecules perturbed by the lattice, is also shown. (b) The position of the H_2 molecular beam with the optical lattice and stimulated Raman pumping beams. The pump beam propagates in the same path as the lattice beam, which is also deployed as the Stokes beam for achieving SRP. The ultraviolet probe beam is used to ionize and detect the molecules perturbed by the lattice. $v = 0$ and $v = 1$ are the ground and excited vibrational state respectively.

In order to achieve this tagging process via SRP, we use one of the lattice beams as stokes beam in the SRP for detecting the molecules in the lattice. Therefore, we propose using the SRP to overcome the challenge of probing the slowed molecules.

This thesis will focus on the progress towards achieving a stimulated Raman pumping scheme, which will be employed to detect H_2 molecules decelerated in chirped optical lattices. The aim of the SRP is to tag the molecules that have been decelerated in the optical lattices. Previous experiments in our laboratory have used direct ultraviolet photoionization to detect H_2 molecules within an optical lattice [26]. However, deceleration of H_2 molecules has not been attempted with this scheme because it is highly challenging to distinguish the ionization signal of the slowed molecules from the rest in the molecular beam. Hence, we decided to employ the SRP scheme to solve the detection issue. By means of the SRP scheme, the molecules in the optical lattices are excited to the $J = 1$, $v = 1$ rovibrational state and detected in that specific rovibrational state by state selective UV photoionization. In order to accomplish the SRP, two laser beams, a pump beam and a Stokes beam, are required. In addition, a UV photoionisation beam (probe) is required to ionise the excited molecules in the $v = 1$ in the optical lattice. We use one of the lattice beams as the Stokes beam and have the pump beam co-propagating with it. Subsequently, only H_2 molecules in the $v = 1$ vibrational state where the two lattice beams cross can be ionized and detected by a UV probe beam without ionizing the background molecules outside of the optical lattice. This is illustrated in figure 1.2b.

SRP allows the preparation of a single rovibrational quantum level in the ground electronic state of a molecule. Various experiments employing SRP can be found in the literature [27–29]. In our study, the SRP scheme is applied to H_2 molecules. A detailed explanation of this scheme is as follows. Firstly, a pump beam excites H_2 molecules from the $v = 0$, $J = 1$ ro-vibrational level in the ground electronic state $X^1\Sigma_g^+$ to a virtual state. A red shifted Stokes beam simultaneously takes these molecules down to the $v = 1$, $J = 1$ ro-vibrational level in the ground electronic state. Following that, a pulsed UV probe beam ionises the molecules in

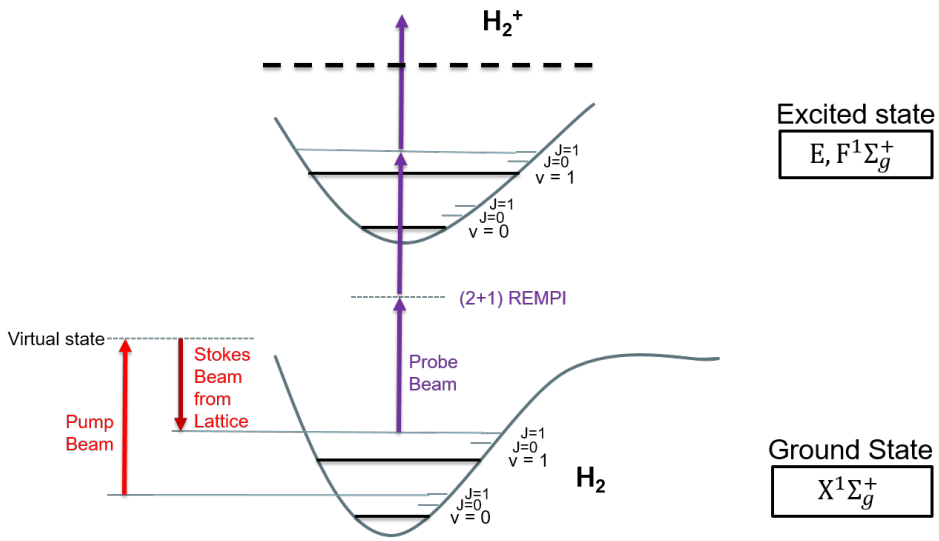

Figure 1.3: Figure showing the proposed stimulated Raman pumping and REMPI detection of H_2 $(v = 1)$ molecules. In the SRP scheme, a pump beam and the lattice beam (used as a Stokes beam) excites H_2 molecules from the $v = 0$, $J = 1$ to $v = 1$, $J = 1$ ro-vibrational level in the ground electronic state $X^1\Sigma_g^+$ via a virtual state. From this level, a UV probe beam state-selectively ionizes the molecules at this specific state by a $(2+1)$ REMPI process via the $E, F^1\Sigma_g^+$ electronically excited state. The $E, F^1\Sigma_g^+$ state is the lowest electronically excited level that can be reached by absorption of two photons from the ground state $X^1\Sigma_g^+$ according to the symmetry selection rules.

this particular state using a $(2+1)$ REMPI process via the $E, F^1\Sigma_g^+$ electronically excited state, as illustrated in figure 1.3. In our SRP scheme, the Stokes beam is one of the lattice beams at ~ 1064 nm. In the SRP, the energy difference between the two beams is tuned to correspond to a particular ro-vibrational transition. Although the wavelength for the pump beam and the probe beam are known in theory, previously they had not been experimentally confirmed using our experimental setup in our laboratory. In order to achieve SRP and $(2+1)$ REMPI, we needed three laser beams which are pump, stokes/lattice and probe beams respectively as shown in

figure 1.3. Amongst these three beams, the Stokes/lattice beam wavelength was known but the others were not. Since it was highly challenging to achieve the SRP scheme and $(2+1)$ REMPI process with two unknown wavelengths, we decided to divide the former and the latter process into two different experiments. This allowed us to confirm independently the two unknown wavelengths through two different experiments and also assess the feasibility of the tagging scheme. Firstly, a coherent anti-Stokes Raman scattering(CARS) experiment was conducted to obtain the pump wavelength. CARS uses multiple photons to address the molecular vibrations, and produces a coherent signal. In CARS experiment, the Stokes beam was one of the lattice beams. In a separate experiment, a non-equilibrium plasma was produced in a static gas cell to generate vibrationally excited molecules in the $v = 1$. Thus, by using the $(2 + 1)$ REMPI process in the non-equilibrium plasma, the excited molecules in the $v = 1$ was detected and the probe beam wavelength was confirmed.

Chapter 2

Production of excited H_2 in non-equilibrium plasmas

Non-equilibrium plasmas can be used to produce ro-vibrationally excited states in gases [30–33]. Non-equilibrium discharge is defined as charged species having much higher kinetic energy than neutral species. The most distinct characteristic that differentiates non-equilibrium discharge plasma from other discharge plasmas is the electron temperature (T_e), i.e. average electron energy $(1$ to 10 eV$)$ in the plasma is about two orders of magnitude higher than ion temperature (T_i) and neutral or gas temperature (T_g). Since there is a large difference in mass, merely a fraction of the electron energy is imparted into neutrals and ions through elastic collisions. Most of the energy losses of electrons are caused by inelastic collisions such as electronic and vibrational excitation of atomic and molecular species [34, 35]. Development of the $(2 + 1)$ REMPI detection scheme of $v = 1$ tagged molecules can be achieved by using the naturally produced vibrationally excited molecules within the non-equilibrium plasma. Using these vibrationally excited H_2 molecules, we can determine the probe beam wavelength experimentally and confirm the detection capability of our probe laser.

The field of gas discharge plasmas has expanded primarily due to the exotic non-equilibrium aspects of such a plasma. High T_e and low T_g in non-equilibrium discharge plasma result in the production of highly reactive species such as free radicals as a consequence of the frequent excitation and disassociation of atomic and molecular species. Thus, non-equilibrium discharge plasmas provide chemically active space in which the reactions that may not occur in thermal equilibrium readily arise. A wide range of chemical, non-equilibrium conditions are possible since external parameters can easily be modified [36]. Firstly, the input gas can be changed and this defines the species in the plasma such as atoms, molecules etc. Secondly, the pressure range from approximately 0.1 Pa to atmospheric pressure. A high pressure (i.e. above atmospheric pressure) typically implies frequent collisions in the plasma, which means a short collision mean free path compared to the discharge length $(0.1 - 1\ \mathrm{m})$, and thus pushes the plasma toward thermal equilibrium where the temperature of all species (electrons, ions, neutral species) is the same. Some other parameters that can modify the non-equilibrium conditions can define the electromagnetic field structure, the discharge configuration, the discharge volume and the temporal behaviour (e.g. by pulsing the plasma). In order to match the requirement for our purpose which is to generate vibrationally excited molecules, we decided to produce a DC glow discharge plasma to create vibrationally excited H_2 molecules in its non-equilibrium positive column region where the vibrational temperature is much greater than the gas temperature [37].

This chapter will begin with a literature review about commonly used plasma and discharge studies with a particular emphasis on non-equilibrium plasmas. Next, an introduction to the state selective detection of H_2 molecules by $(2+1)$ REMPI process will be presented. The main outcome of this experiment is to independently confirm the probe beam wavelength, which will be employed in the $(2 + 1)$ REMPI process to detect vibrationally excited molecules via the SRP scheme as stated in the previous chapter.

2.1 Introduction to plasma and discharges

The word 'plasma' was introduced into the physics literature by Langmuir [38, 39] to describe the region of a gas discharge in which the number of electrons and ions is equal. Plasmas are ionised gases consisting of positive/negative ions and electrons as well as neutral species. The ionisation degree can differ from 100% (fully ionized gases) to 10^{-4} – $10^{-6}\%$ (partially ionized gases) [36]. Plasma behaviour can be observed either in the solid [40], liquid [41], or gas phases [42]. However, this thesis focuses on the generation of collisional gas phase plasmas, created by ionising a neutral gas. A number of techniques have been developed to cause gas ionisation, including ionisation by external sources of radiation such as X-rays [43, 44], electron beams [45, 46], photo-ionising radiation [43, 44] and through use of a gas discharge [47, 48]. Amongst these techniques, gas discharges are by far the most common approach. There has recently been a great interest in studying atmospheric pressure plasmas. Examples of conventional sources for atmospheric plasmas are arcs, corona discharges and dielectric barrier discharges (DBDs)[49–55]. The creation of spatially uniform, atmospheric pressure non-equilibrium plasma discharges [56] (also known as atmospheric pressure glows (APG)) are desirable due to their potential industrial applications [57]. A number of other approaches for APG formation are also known, such as direct current, radio frequency (RF) and microwave discharges [58]. We will here focus on low pressure DC glow discharges, since these are relatively easy to produce experimentally compared to the other approaches.

The basic plasma process in a glow discharge can be explained as follows. A few electrons are initially emitted from electrodes due to the omnipresent cosmic radiation. If a voltage difference is not applied between the electrodes, the emitted electrons will not be able to create a discharge. However, when a sufficiently high potential difference is applied between two electrodes placed in a gas; as the voltage increases to the ionisation point, Townsend discharge happens [59]. The Townsend discharge is a gas ionization process where free electrons,

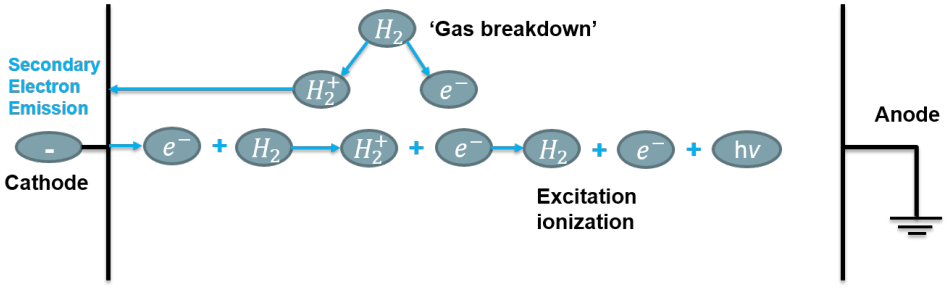

Figure 2.1: Schematic overview of the basic plasma process in a glow discharge. When a potential difference is applied between two electrodes, the gas (e.g. hydrogen) will break into electrons and ions. The latter can cause secondary electron emission at the cathode. The emitted electrons give rise to collisions in the plasma. One result of these collisions is excitation, which is typically followed by de-excitation with emission of radiation, hence the name of 'glow' discharge. Some collisions result in ionisation which creates new electrons and ions, therefore making the glow discharge a self-sustaining plasma.

accelerated by a sufficiently strong electric field, give rise to electrical conduction through a gas by avalanche multiplication caused by the ionization of molecules by ion impact. After this, the gas will break down into ions and electrons. Then, the resultant ions will be accelerated towards the cathode where they release more electrons by ion-induced secondary electron emission. These newly emitted electrons give rise to further ionisation collisions. As a result, this process will create new ions and electrons and leads to an avalanche process. The most important collisions are inelastic collisions, initiating excitation and ionisation as shown in figure 2.1. The excitation collisions are followed by de-excitations via spontaneous emission, which are responsible for the 'glow' . Consequently, electron emission at the cathode and ionisation in the plasma make the glow discharge a self-sustaining plasma [36].

The DC glow discharge contains several different characteristic regions. The potential difference applied between the two electrodes is typically not equally distributed between cathode and anode, but it decreases almost entirely in the first millimetres in front of the cathode be-

cause the voltage current characteristic of the glow discharge is highly non-linear. This region adjacent to the cathode, which is thus characterized by a strong electric field, is called the 'cathode dark space' or 'sheath'. In the largest part of the discharge, called the 'negative glow', the potential known as the 'plasma potential' is nearly constant and slightly positive with a very small electric field. Regions described as 'glow' emit significant light whereas those labelled as 'dark spaces' do not. When the distance between cathode and anode is relatively long (e.g. a few centimetres), two more regions can be present known as the 'Faraday dark space' and the 'positive column' [36]. They are characterized by a slightly negative electric field which conducts electrons toward the anode. These two regions are generally present in glow discharges used as lasers ('positive column lasers') and as fluorescence lamps. Below the ionisation voltage or breakdown voltage there is no glow, but as the voltage increases to the ionisation point the Townsend discharge occurs just as the glow discharge becomes visible. This is the start of the normal glow range. As the voltage is increased above the normal glow range, abnormal glow begins. If the voltage is increased to the point where the cathode glow covers the entire cathode, arc discharge begins. On the voltage versus current diagram, normal glow discharge corresponds to the region between Townsend discharge and the arc discharge, where the discharge voltage remains essentially constant for varying plasma current [60, 61].

In order to get the discharge to be non-equilibrium ($T_{\text{vib}} > T_{\text{trans}}$), the energy gained in vibrational excitation should be greater than the energy lost by vibrational to translational (V – T) relaxation. This special non-equilibrium regime, where vibrationally excited molecules are present, occurs in the positive column of normal DC glow discharge. Hence, the H_2 discharge experiment was conducted in the positive column of the normal DC glow discharge. In the next section, a detailed explanation for the vibrational excitation of H_2 molecules in non-equilibrium plasmas will be discussed.

2.2 Non-equilibrium Glow Discharge

The determination of the vibrational (T_{vib}), gas (T_{trans}), and rotational (T_{rot}) temperatures in non-equilibrium conditions is of significant importance for the study of low temperature plasmas and plasma interactions with a surface [62–64]. The translational or gas kinetic temperature in a gas discharge is a parameter of wide importance in the field of plasma chemistry.

A number of diagnostic technique exist to determine the vibrational, translational, and rotational temperature of the gas discharges, such as pyrometry, interferometry [65], Coherent Anti-Stokes Raman Scattering (CARS) [66, 67], Laser Induced Fluorescence (LIF) [68, 69] and Optical Emission spectroscopy (OES)[68, 70–74].

The rotational temperature, T_{rot}, of an excited state may have physical meaning if the characteristic time of rotation-translation relaxation, τ_{RT}, for the vibronic state in question is much shorter than the characteristic time of population and deactivation processes [32]. In this condition, the rotational population distribution in this rovibronic state follows the Boltzmann distribution with rotational temperature equal to translational temperature [75]. However, in a completely opposite condition, if the radiative lifetime is much smaller than τ_{RT}, rotational collisional mixing of neutral species during the lifetime of the excited rovibronic state is not efficient enough to ensure equilibrium of the rotational distribution with the gas temperature. The degree of relation between the rotational population density distribution in the excited rovibronic state and the population of the ground electronic state can be calculated with the excitation-deactivation balance equation that can be found in the literature [76].

It is known that at low rotational levels $J = 0 - 5$, the relaxation rates between the rotational and translational degrees of freedom of the Hydrogen molecules are high [64]. Thus, experimental studies have showed that the measured rotational temperature, T_{rot}, can be considered to be equal to the gas temperature in the total pressure range investigated in a radio frequency inductive H_2 discharge plasma [31].

On the other hand, in the same study, a large difference between the vibrational and rotational temperatures has been observed. This finding is a result of the non-equilibrium kinetic processes between electrons and Hydrogen molecules, atoms and ions as reported by several theoretical studies [63, 77–81]. Consequently, a satisfactory agreement was achieved by a comparison between their and corresponding theoretical results based on the kinetic model developed in reference [80]. The model explains the relaxation of vibrationally excited H_2 molecules due to the action of several inelastic processes involving $e - V$ (electron-vibration), $V - V$ (vibration-vibration), and $V - T$ (vibration-translation) energy transfers. A significant role in the deactivation of vibrationally excited H_2 molecules is played by $V - T$ transfer from atomic Hydrogen, whose rate is approximately three orders of magnitude bigger than the corresponding $V - T$ rates from Hydrogen molecules [31]. As a result, the concentration of atomic Hydrogen, which is controlled by heterogeneous recombination in the previously mentioned experiment, plays a significant role in determining the vibrational temperatures particularly at low pressure. In that experiment, the measurements of the rotational, gas and vibrational temperatures in H_2 rf inductive discharge plasma at total pressure of $0.5 - 8$ torr using CARS spectroscopy. However, at high pressure, $V - T$ deactivation from molecules and $V - V$ energy transfer start being dominant [71].

Although many studies show that vibrational excitation of pure H_2 molecules can be achieved in non-equilibrium discharge plasmas, a mixture of H_2 and a noble gas at few torr pressure in which H_2 is only a few percent, proved to be more effective in producing the vibrational excitation [82, 83]. This is because the electron temperature is greater compared to pure H_2, hence the electrons can more effectively populate highly excited vibrational states of H_2. In addition, the diffusion loss of electrons, H^- and vibrational states of H_2 to the tube wall can be decreased due to the presence of a buffer gas. A metal cathode can act as a sink for Hydrogen atoms because of their high sticking coefficient on a metal surface, which reduces the Hydrogen density. Therefore, the destruction rate of highly excited H_2 vibrational states via

$V - T$ relaxation collisions with H atoms can be significantly decreased. Furthermore, in the case of the Hollow Cathode Discharge (HCD) configuration, the electron beam component of the HCD additionally yields population of the H_2 vibrational state because of a two-step process, in which excitation of B and C levels of the H_2 molecule and radiative decay to several vibrational states occur.

For these reasons, our study investigates the generation of vibrationally excited states in a mixture of a noble gas and H_2. Although there are models that look at a variety of pure H_2 discharges [37, 80, 84–92], only a few kinetic models for a noble gas and H_2 mixture have been studied. There exists one comprehensive kinetic model for an Ar – H_2 mixture [82] and two models, which investigate a Ne – H_2 mixture [93, 94]. Both models for the Ne – H_2 mixture emphasize the kinetics of Ne excited states. However, a thorough investigation of the H_2 vibrational kinetics and the impact of Ne on the vibrational kinetics of H_2 has not been addressed in these studies. A comprehensive study by Petrov and Petrova showed an unusually high population of vibrationally excited Hydrogen molecules in a Ne – H_2 mixture [83]. In their study, the researchers investigated the formation of negative Hydrogen ions in a conventional HCD with a mixture of Ne – H_2. The model employed in their work involved coupling the solution of the steady-state spatially averaged electron Boltzmann equation with a system of balance equations for Neon and Hydrogen neutral and charged particles. Comprehensive information for the kinetic processes occurring in Ne – H_2 plasma was presented in their work.

The vibrational kinetics of H_2 is known to play a crucial role in non-equilibrium plasma processes, and substantial theoretical efforts have been made to calculate the vibrational distribution function (VDF) [78, 95–100]. The vibrational kinetics are coupled with electron Boltzmann equations and the heavy particle kinetics in a self-consistent way [96, 97]. The coupling between internal plasma and input parameters is not only because of electron impact excitation and super-elastic collisions with H_2 vibrationally excited states, but also because of loss of electrons through dissociative attachment.

The bound vibrational levels have energies $E_v = \omega_e(v+\frac{1}{2}) - \omega_e\chi_e(v+\frac{1}{2})^2$, $0 \le v \le 14$, where $\omega_e = 4401.21$ cm^{-1} and $\omega_e\chi_e = 121.336$ cm^{-1} [96]. The processes related to the vibrational kinetics of H_2 are summarized as follows:

- $e - V$ relaxation and $E - V$ relaxation

  $H_2(v) + e \xrightarrow{k_{vw}} H_2(w) + e$

  $H_2(0) + e \xrightarrow{k_{BC}} H_2(B^1\Sigma_u^+, C^1\Pi_u) + e \xrightarrow{\xi_v k_{BC}} H_2(v) + e + h\nu$

- $V - T$ relaxation

  $H_2(v) + H \xrightarrow{P^{H}_{v,v-1}} H_2(v-1) + H, \qquad H_2(v-1) + H \xrightarrow{P^{H}_{v-1,v}} H_2(v) + H$

  $H_2(v) + H_2 \xrightarrow{P^{H_2}_{v,v-1}} H_2(v-1) + H_2, \quad H_2(v-1) + H_2 \xrightarrow{P^{H_2}_{v-1,v}} H_2(v) + H_2$

  $H_2(v) + Ne \xrightarrow{P^{Ne}_{v,v-1}} H_2(v-1) + Ne, \quad H_2(v-1) + Ne \xrightarrow{P^{Ne}_{v-1,v}} H_2(v) + Ne$

- $V - V$ relaxation

  $H_2(v) + H_2(w-1) \xrightarrow{P^{w-1,w}_{v,v-1}} H_2(v-1) + H_2(w)$

- Wall deactivation

  $H_2(v) \xrightarrow{\nu_{wall}} H_2(0)$

- Dissociative attachment

  $H_2(v) + e \xrightarrow{k_{att}} H^- + H$

where k_{vw} the relaxation rate coefficient from v to w vibrational state where the former and latter are upper and lower vibrational states. k_{BC} is the excitation rate coefficient and ξ_v is the fractional contribution to each vibrationally excited state "v". $P^{H}_{v,v-1}$, $P^{H_2}_{v,v-1}$ and $P^{Ne}_{v,v-1}$ are the rate coefficients for $V-T$ relaxation for H atoms, H_2 and Ne atoms respectively. $P^{H}_{v-1,v}$, $P^{H_2}_{v-1,v}$ and $P^{Ne}_{v-1,v}$ are the rate coefficients for the excitation from $v-1$ to v vibrational state. $P^{w-1,w}_{v,v-1}$

is the rate coefficient for $V - V$ processes involving vibrationally excited H_2. ν_{wall} is the wall deactivation in which the diffusion of the $H_2(v \geq 1)$ molecules and their deactivation at cathode wall are a major loss mechanism. Lastly, k_{att} represents the dissociation rate coefficient.

The cross sections and rate coefficients have been extensively studied by Loureiro et. al. [96]. Cross sections for electron impact vibrational excitation are available merely from v = 0 to w = 1, 2, and 3 [101–103]. The cross sections from level v to level $w = v + 1,\ v + 2,\ v + 3$ are assumed to be the same, but with shifted threshold according to the energy difference between levels "w" and "v" [98]. Vibrational excitation of H_2 also occurs through electron impact excitation to electronic states H_2 $(B^1\Sigma_u^+)$ and H_2 $(C^1\Pi_u)$, followed by radiative decay to $H_2(v)$ $X^1\Sigma_g^+$. The excitation cross sections to both electronic states "B" and "C" are known in the literature [101, 102, 104, 105]. Approximately 60% of the excitation to state B and 99% of the excitation to state C decays back to discrete vibrational levels "v" of H_2 (X, v) in the ground electronic states as shown in table 2.1 [106]. The fractional contribution ξ_v to each vibrational state "v" is also provided in reference [106].

v	0	1	2	3	4	5	6	7
B → X	0.083	0.048	0.039	0.036	0.034	0.034	0.035	0.035
C → X	0.160	0.100	0.096	0.097	0.100	0.096	0.085	0.071
v	8	9	10	11	12	13	14	
B → X	0.036	0.038	0.040	0.044	0.023	0.043	0.025	
C → X	0.056	0.042	0.030	0.021	0.011	0.009	0.005	

Table 2.1: Fraction of the excitations to states $H_2(B)$ and $H_2(C)$ which decay back to vibrationally excited H_2 in the $X^1\Sigma_g^+$ state [106].

The excitation and de-excitation of molecular rotations have been treated in the continuous approximation in a study carried out by Frost and Phelps [107]. This study reported that rota-

tional excitation and momentum transfer cross sections for low-energy electrons in hydrogen and nitrogen are obtained from a comparison of theoretical and experimental values for the mobility and the diffusion coefficient. The theoretical values of the transport coefficients were obtained by calculating accurate electron energy distribution functions using an assumed set of elastic and inelastic cross sections. The discrete nature of the energy loss occurring in a rotational or vibrational excitation collision was included in the theory, as were collisions of the second kind with thermally excited molecules.

2.3 The electronic spin and Hund's cases

In molecules, as in atoms, magnetic interactions couple the spin and orbital angular momenta. The most important of these interactions is the one between the electronic spin **S** and the electronic orbital momentum **L**. This can be defined by an effective interaction of the form $\bar{A}\mathbf{L}\cdot\mathbf{S}$, where $\bar{A}$ is a constant for a given multiplet, called spin-orbit coupling constant. The rotation of the molecule as a whole also creates a magmatic field that interacts with the magnetic moments of the electrons. That spin-orbit coupling can also be expressed as an effective interaction of the form $\bar{\Gamma}\mathbf{N}\cdot\mathbf{S}$, where $\bar{\Gamma}$ is a constant. In addition, the nuclear spins also interact with **L**, **S** and **N**. However, the interaction with the nuclear spins has a negligible effect on the energy levels, even though, the symmetry of the nuclear spin wave functions can be crucial in the spectra of homonuclear diatomic molecules which will be explained in the case of H_2 in details. If the nuclear spins are neglected, the total angular momentum operator **J** for a diatomic molecule is expressed as [108]:

$$\mathbf{J} = \mathbf{L} + \mathbf{N} + \mathbf{S} = \mathbf{K} + \mathbf{S} \tag{2.1}$$

where **N**, the orbital angular momentum of the relative motion of the nuclei, is in a direction at right angles to the internuclear line. In the absence external electric and magnetic fields,

molecular wave functions must be eigenfunctions of $\mathbf{J}^2$ with eigenvalues $J(J+1)\hbar^2$ and of J_z with eigenvalues $M_J\hbar$ where J_z is the component of **J** in an arbitrary direction in the space-fixed coordinate frame. An analysis of the couplings between the vectors **L**, **N** and **S** which add to form **J** and their effect on energy levels was given by F. Hund who defined five limiting cases (a) to (e). These cases depend on the relative strength of the electrostatic, spin-orbit and spin-rotation energies. The electrostatic interaction between the electrons and nuclei restricts the electronic wave function to rotate as the molecule rotates. A measure how important this interaction is the magnitude of the difference in energy $\mid \Delta E \mid$ between two adjacent electronic levels with different values of Λ. The magnitude of the spin-orbit interaction is expressed by the absolute value of $A = \bar{A}\hbar^2$, while the importance of the spin-rotation coupling is dictated by the rotational constant $B = \frac{\hbar^2}{2\mu R_0^2}$. Hund's cases are related to different limiting values of the three energies, $\mid \Delta E \mid$, $\mid A \mid$ and B.

Hund's case (a), $\mid \Delta E \mid \gg \mid A \mid \gg \boldsymbol{B}$

In this case, the electronic interaction is much greater than spin-orbit interaction that in turn is much greater that rotational energy. An instance can be given by the AΠ term of CO^+. The nearest level with a different value of Λ is the $X^2\Sigma^+$ ground state, from which it is calculated that $\Delta E = 20733$ cm^{-1} while the spin-orbit constant is $A = -117$ cm^{-1} and $B = 1.6$ cm^{-1} [108].

The electrostatic interaction has axial symmetry and, this causes **L** to precess about the internuclear axis, which means that $L_{\bar{z}} = \pm\Lambda\hbar$ and $\langle L_{\bar{x}} \rangle = \langle L_{\bar{y}} \rangle = 0$. As in this case, the rotation of the molecule is slow, and the spin-orbit interaction is large compared to the rotational energy, the spin angular momentum **S** will also tend to precess about the internuclear axis. This indicates that the spin should be quantised along the internuclear axis (the body-fixed $\overline{OZ}$ axis). Simultaneous eigenfunctions of $\mathbf{S}^2$ and $S_{\bar{z}}$ can be found with eigenvalues $S(S+1)\hbar^2$ and $\Sigma\hbar$ respectively. The quantum number Σ used here should not be confused with the symbol Σ

denoting the electronic term with $\Lambda = 0$. Denoting these eigenfunctions by $|S, \Sigma\rangle$ we have that:

$$\mathbf{S}^2 |S, \Sigma\rangle = S(S+1)\hbar^2 |S, \Sigma\rangle \tag{2.2}$$

and

$$S_{\bar{z}} |S, \Sigma\rangle = \Sigma\hbar |S, \Sigma\rangle \tag{2.3}$$

where the quantum number Σ can take the $(2S+1)$ values $-S,\ -S+1,\ \ldots,\ S-1,\ S$. Since $\mathbf{S}^2$ and $S_{\bar{z}},\ L_{\bar{z}},\ \mathbf{J}^2$ and $J_{\bar{z}}$ can be found specified by the quantum numbers $S,\ \Sigma,\ \pm\Lambda,\ J$ and M_J. Since $\mathbf{N}$ is perpendicular to the internuclear axis, $N_{\bar{z}} = 0$ and therefore, see the figure 2.2 (a)

$$J_{\bar{z}} = L_{\bar{z}} + S_{\bar{z}} \tag{2.4}$$

It follows that the molecular wave function is also an eigenfunction of $J_{\bar{z}}$ corresponding to the eigenvalues $\Omega\hbar$, where

$$\Omega = \pm\Lambda + \Sigma \tag{2.5}$$

It should be stated that $\mathbf{N}^2$ does not commute with $S_{\bar{z}}$, this neither $\mathbf{N}$ nor $\mathbf{K}(= \mathbf{N} + \mathbf{L})$ are conserved quantities. If we write the normalized eigenvectors of the molecular Hamiltonian as $|S,\ \Sigma,\ \pm\Lambda,\ J,\ \Omega,\ M_J\rangle$, the additional energy due to the spin-orbit coupling is E_{LS}, where

$$E_{LS} = \bar{A} \langle S,\ \Sigma,\ \pm\Lambda,\ J,\ \Omega,\ M_J \mid \mathbf{L}\cdot\mathbf{S} \mid S,\ \Sigma,\ \pm\Lambda,\ J,\ \Omega,\ M_J\rangle = A\Lambda\Sigma \tag{2.6}$$

To obtain this result, we recollect that as $\mathbf{L}$ and $\mathbf{S}$ are quantized along the body-fixed axis $\langle L_{\bar{x}}\rangle = \langle L_{\bar{y}}\rangle = \langle S_{\bar{x}}\rangle = \langle S_{\bar{y}}\rangle = 0$. Then, the total electronic energy is:

$$E_S^T(R_0) = E_S(R_0) + A\Lambda\Sigma \tag{2.7}$$

For a given value of Λ the energy levels are split into $(2S+1)$ multiplet components, which are equally spaced in energy. The corresponding electronic terms are labelled by a subscript

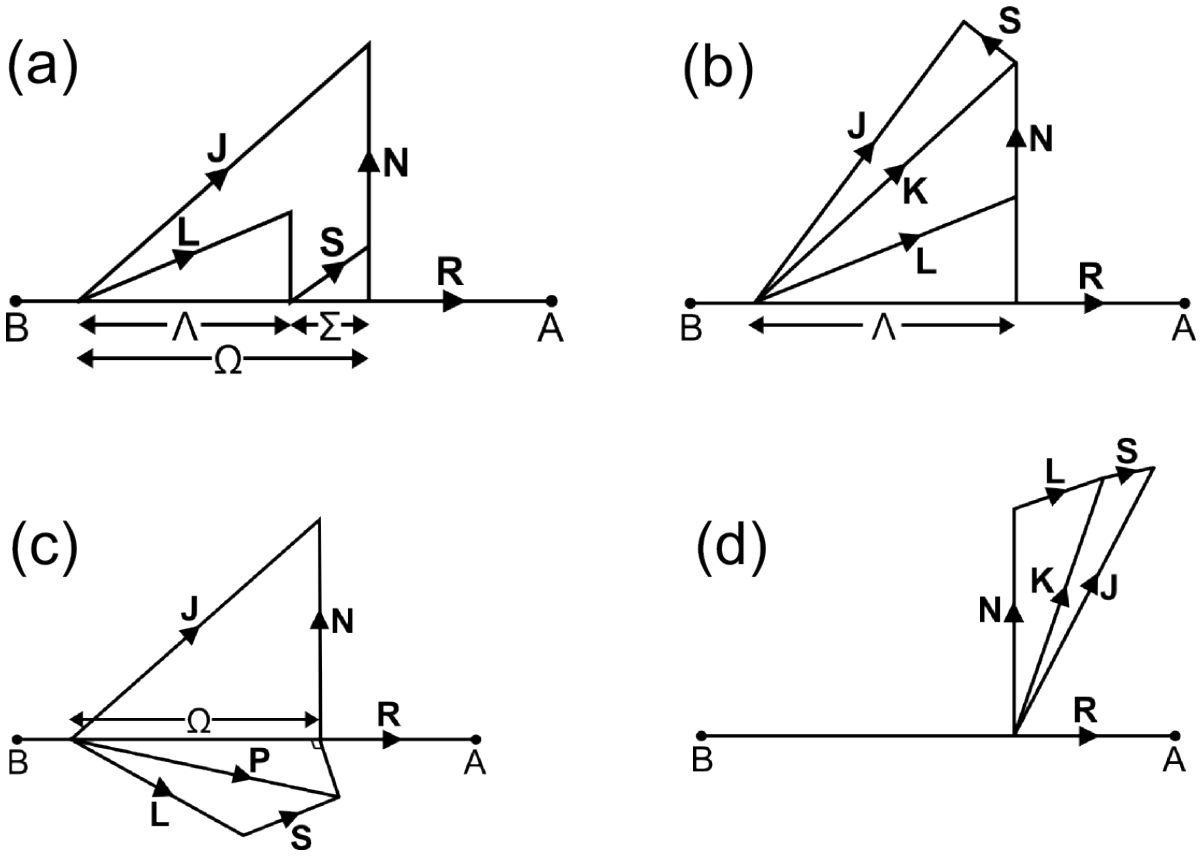

Figure 2.2: Hund's coupling cases: (a) **L** and **S** precess about **R** with well-defined components Λ and Σ, respectively, along **R**. **N** couples with $\Omega\hat{\mathbf{R}}$ to form **J**, where $\Omega = \Lambda + \Sigma$. (b) **L** precesses about **R** with well-defined component Λ along **R**. **N** couples with $\Lambda\hat{\mathbf{R}}$ to form **K** and **K** couples with **S** to form **J**. (c) **L** and **S** couple to form **P** which precess about **R**. The component of **P** along **R**, Ω, is well defined. **N** couples with $\Omega\hat{\mathbf{R}}$ to form **J**. (d) **L** and **N** couple to form **K**. **J** results from coupling **K** to **S**.

giving the value of Ω. For instance, in a $^3\Pi$ state with $\Lambda = 1$ and $S = 1$, the allowed values Ω are $\Omega = 0,\ 1,\ 2$ and the corresponding terms are written as $^3\Pi_0,\ ^3\Pi_1,\ ^3\Pi_2$. Each of these multiplets gives rise to a series of rotational levels.

To obtain the rotational energy spectrum we need to introduce the approximation where

R is set equal to the equilibrium separation R_0 of the nuclei. The rotational kinetic energy operator is then $\frac{\mathbf{N}^2}{2\mu R_0^2}$ and the rotational energy in Hund's case (a) is thus $E_{\mathrm{r}}^{'}$, where

$$E_{\mathrm{r}}^{'} = \frac{1}{2\mu R_0^2} \langle S,\ \Sigma,\ \pm\Lambda,\ J,\ \Omega,\ M_J \mid \mathbf{N}^2 \mid S,\ \Sigma,\ \pm\Lambda,\ J,\ \Omega,\ M_J \rangle \tag{2.8}$$

Let us introduce a vector $\mathbf{\Omega}$ by setting

$$\mathbf{\Omega} = \Omega\hbar\hat{\mathbf{R}} \tag{2.9}$$

where $\hat{\mathbf{R}}$ is a unit vector along the body-fixed $\overline{OZ}$ axis (the internuclear line), we have (see figure 2.2)

$$\mathbf{N} = \mathbf{J} - \mathbf{\Omega} \tag{2.10}$$

From 2.8 and 2.10, we find that:

$$E_{\mathrm{r}}^{'} = B[J(J+1) - \Omega^2] \tag{2.11}$$

Since $\mid \mathbf{J} \mid \geq J_{\bar{\mathrm{z}}}$, the result of equation 2.11 is subject to the important restriction that $J \geq \Omega$. The observation that spectral lines with lower values of J are missing provides an significant method of determining the value of Ω when it is not known. The quantum numbers J can take integer values when the spin has integer values or half-odd integer values if the spin is a half-odd integer. The value of $-B\Omega^2$ only depends on the electronic state thus this quantity can be combined with the energy $E_s^T(R_0)$, producing [108]:

$$E_s^{'}(R_0) = E_s^T(R_0) - B\Omega^2 \tag{2.12}$$

in this case the rotational energy becomes:

$$E_{\mathrm{r}} = BJ(J+1), \qquad J = \Omega,\ \Omega+1,\ \Omega+2,\ \cdots \tag{2.13}$$

In Hund's case (a) each level remains twofold degenerate with the two states with $L_{\bar{\mathrm{z}}} = \pm\Lambda\hbar$ $(\Lambda \neq 0)$ having the same energy, and indeed in the absence of external fields the $(2J+1)$ substates with different values of M_J are always degenerate.

Hund's case (b), $|\,\Delta E\,| \gg \boldsymbol{B} \gg |\,A\,|$

In Hund's case (b), the spin-orbit interaction is either zero or is so small that it can be neglected. When this occurs the most important spin interaction is the one with the rotational motion of the nuclei. That can be expressed by the effective interaction $\bar{\gamma}\mathbf{K}\cdot\mathbf{S}$, where $\mathbf{K} = \mathbf{L} + \mathbf{N}$. The energy shift is very small and can be determined from first-order perturbation theory [108]. The unperturbed Hamiltonian contains no spin interaction. The rotational energies are given by:

$$E_{\mathrm{r}} = BK(K+1), \qquad K = \Lambda,\ \Lambda+1,\ \Lambda+2,\ \cdots \tag{2.14}$$

The uncoupled wave function for the unperturbed system is the product of the spin function $|S,\ M_S\rangle$ which is an eigenfunction of $\mathbf{S}^2$ and S_{z} and spatial functions $|\pm\Lambda,\ K,\ M_K\rangle$ that are eigenfunctions of $L_{\bar{\mathrm{z}}}(=\ K_{\bar{\mathrm{z}}})$, $\mathbf{K}^2$ and K_{z}. If the interaction $\bar{\gamma}\mathbf{K}\cdot\mathbf{S}$ is added to the Hamiltonian, the wave function is no longer eigenfunction ofS_{z} and K_{z}, however the total angular momentum $\mathbf{J} = \mathbf{K}+\mathbf{S}$ is always conserved as seen the figure 2.2 case (b). For this reason, an appropriate basis for perturbative calculations is a simultaneous eigenfunction of $\mathbf{S}^2,\ \mathbf{K}^2,\ K_{\bar{\mathrm{z}}}, J^2$ and J_{z} which can be written as $|S,\ K, \pm\Lambda,\ J,\ M_J\rangle$. This function can be defined as a linear combination of the uncoupled functions as:

$$|S,\ K, \pm\Lambda,\ J,\ M_J\rangle = \sum_{M_K M_S} \langle KSM_K M_S|J,\ M_J\rangle\,|S,\ M_S\rangle\,|\pm\Lambda,\ K,\ M_K\rangle \tag{2.15}$$

where $\langle KSM_K M_S|J,\ M_J\rangle$ is a Clebsch-Gordan coefficient (ref. the book). The possible values of J for given values of K and S are:

$$J = |\,K-S\,|,\ |\,K-S\,|+1,\ \cdots,\ K+S \tag{2.16}$$

with the restriction $J \geq 0$. The additional energy due to the spin-rotational coupling is given by:

$$\Delta E_{\mathrm{r}} = \bar{\gamma}\,\langle S,\ K,\ \pm\Lambda,\ J,\ M_J|\mathbf{K}\cdot\mathbf{S}|S,\ K,\ \pm\Lambda,\ J,\ M_J\rangle \tag{2.17}$$

where $\bar{\gamma}$ is called the spin-rotation constant. Since $\mathbf{K}\cdot\mathbf{S} = (\mathbf{J}^2 - \mathbf{K}^2 - \mathbf{S}^2)/2$, we obtain:

$$\Delta E_{\mathrm{r}} = \frac{\gamma}{2}[J(J+1) - K(K+1) - S(S+1)] \tag{2.18}$$

where $\gamma = \bar{\gamma}\hbar^2$. The total rotational energy is:

$$E_{\mathrm{r}} = BK(K+1) + \frac{\gamma}{2}[J(J+1) - K(K+1) - S(S+1)]. \tag{2.19}$$

For instance, if the total spin is $S = 1/2$, there are two possible values of J, $J = K \pm 1/2$ $(K > 0)$. The degeneracy in J is removed and the rotational energies are:

$$E_{\mathrm{r}} = BK(K+1) + \frac{\gamma}{2}K, \quad J = K + 1/2 \tag{2.20}$$

$$= BK(K+1) - \frac{\gamma}{2}(K+1), \quad J = K - 1/2 \tag{2.21}$$

For diatomic molecules consists of light atoms, for instance CH, OH and SiH, Hund's cases (a) and (b) are useful approximations; case (a) is better approximation than (b) when the spin-orbit energy is larger than about twice the rotational energy. As the number of electrons increases, so does the spin-orbit energy and for diatomic molecules consists of heavy atoms Hund's case (c) is a more useful approximation.

Hund's case (c), $|A| \gg |\Delta E| \gg \boldsymbol{B}$

In this case the spin-orbit coupling, and usually the spin-spin coupling, is so strong that Λ and Σ are no longer good quantum numbers. In order to form a basis the vectors **L** and **S** can be combined to produce a vector **P**. Provided that the rotation of the molecule as a whole is slow, **P** will precess about the internuclear axis and the basis states will be in eigenstates $P_{\bar{z}}$, the component of **P** along the body-fixed $\overline{OZ}$ axis as seen in figure 2.2 case (c). The eigenvalues of $P_{\bar{z}}$ can be expressed by $\Omega\hbar$ and the basis states must be simultaneous eigenstates of $P_{\bar{z}}$, $\mathbf{J}^2$ and $J_{\bar{z}}$. Since the total angular momentum is $\mathbf{J} = \mathbf{P} + \mathbf{N}$ and **N** is at right angles to the internuclear line, $J_{\bar{z}}$ has the same eigenvalues as $P_{\bar{z}}$ and the basis states can be denoted as $|\Omega,\ J,\ M_J\rangle$. An

example of Hund's case (c) is the HgH molecule for which the spin-spin coupling constant is around 4000 cm^{-1} and the $X^2\Sigma$ and $A^2\Pi$ states are strongly mixed(ref the book). For such heavy molecules a relativistic treatment is required and a detailed account of the theory has been given elsewhere [109]. Despite the difficulty of calculating the energy shifts, the rotational energy is easy to obtain, because a vector $\mathbf{\Omega} = \Omega\hbar\hat{\mathbf{R}}$ can be introduced, as in Hund's case (a). As $\mathbf{N} = \mathbf{J} - \mathbf{\Omega}$, we again find the result the equation 2.11.

Hund's case (d), $\boldsymbol{B} \gg |\,\Delta E\,| \gg |\,A\,|$

In this case the electronic interaction is so weak that the electronic wave function is not constrained to rotate with the molecule. This indicates that **L** and **S** can be quantised along the space-fixed OZ axis. The electronic orbital angular momentum **L** can be coupled with **N** to form the orbital angular momentum **K**. In turn**K** can be coupled with **S** to form the angular momentum **J** as seen in figure 2.2 case (d). The lower lying states od diatomic molecules do not conform to these conditions, however the Rydberg states may do so. In these states a valance electron is excited to an orbit that is very far from the centre of mass of the molecule that the remainder of the molecule behaves like a centre of force on the valance electron and the axial symmetry is lost.

Hund's case (e), $|\,A\,| \gg \boldsymbol{B} \gg |\,\Delta E\,|$

This case is similar to case (d), however as there are no examples among the bound states of diatomic molecules we will not consider it.

Spin uncoupling and Λ - doubling

As has been pointed out above, Hund's coupling cases are idealisations, to which many molecules approximately adjust. However, deviations from these idealisations may happen, which repre-

sents a partial uncoupling or decoupling of some of the angular momenta. This uncoupling may increase as J increases because in that case the electrons may not follow the nuclear motion. Therefore, a molecule may fall approximately in one coupling case for low J, but in another case for high J, while for intermediate rotational states one has intermediate coupling. One usual example of intermediate coupling is provided by the transition from Hund's case (a) to (b). For low J, the spin **S** is coupled to the molecular axis, according to the coupling case (a). However, as J increases and the rotational frequency gets larger, **S** uncouples from the molecular axis (spin uncoupling) and eventually couples with **K**, as in Hund's case (b). Another type of uncoupling, generated by an interaction between the rotational and electronic motions, is one which decouples the electronic orbital angular momentum **L** from the molecular axis. This uncoupling has the effect of splitting the two otherwise degenerate levels corresponding to $\Lambda \neq 0$ and known as Λ-doubling.

2.4 The Influence of Nuclear Spins on the Rotational Structure

In the rotational and rotational-vibrational spectrum of homonuclear diatomic molecules such as H_2, N_2 and O_2 and in general in the spectra of molecules with a centre of inversion symmetry, such as CO_2, characteristic intensity differences are observed in the lines originating from levels with an even rotational quantum number J as compared to those stemming from levels with an odd value of J. This is due to the influence of the nuclear spins on the spectra [110]. In molecules with two identical nuclei, the intensity distribution in the spectrum is a result of the influence of the nuclear spins on the symmetry of the overall wavefunction of the molecular state. It is due to the Pauli exclusion principle, which states the overall wavefunction of fermions, i.e. particles with half-integral spins, must be antisymmetric with respect to

exchange of the particles.

Here, we will consider the H_2 molecule for explaining this effect. The two protons in the molecule are fermions with spin $1/2$. The spins of the protons may be parallel; in this case, the molecule has a total nuclear spin quantum number of $I = 1$. The spin wavefunction is symmetric with respect to particle exchange, as the particles are identical when their spins are parallel. This type of hydrogen is called ortho hydrogen, o-H_2. However, the two nuclear spins also be antiparallel, and then the total spin quantum number would be 0. In that case, the spin wavefunction is antisymmetric with respect to exchange of nuclei, and this configuration is called para hydrogen, p-H_2. The statistical weight of the two configurations is $3 : 1$ as shown in Table 2.2.

	I	M_I	Wavefunction	Character
o-H_2	1	1	$\uparrow\uparrow$	
		0	$\frac{1}{\sqrt{2}}(\uparrow\downarrow + \downarrow\uparrow)$	triplet
		-1	$\downarrow\downarrow$	
p-H_2	0	0	$\frac{1}{\sqrt{2}}(\uparrow\downarrow - \downarrow\uparrow)$	singlet

Table 2.2: o- and p-H_2.

The overall wavefunction of the molecule is the product of the spatial functions (including rotation) and the spin functions. Exchange of the nuclei means in the case of a dumbbell molecule simply a reversal of the dumbbell, equivalent to an inversion in space. Under such operation, the rotational eigenfunctions for $J = 1,\ 3,\ 5,\ \cdots$ change their signs; they have negative parity and are antisymmetric with respect to exchange. The rotational functions with $J = 0,\ 2,\ 4,\ \cdots$ remain unchanged; they have positive parity and are symmetric.

The overall parity is the product of the parities of the functions contributing to the total system. For particles with half-integral spin, this must be negative. Then o-H_2, i.e. hydrogen

molecules with $I = 1$ and therefore positive parity of the function, must have rotational states with negative parity, i.e. $J = 1,\ 3,\ 5,\ \cdots$ with the statistical weight 3, if the remaining spatial function have positive parity, as indeed the case for the ground state of hydrogen. This is true of the state denoted by $^1\Sigma_g^+$, the ground state of hydrogen molecule [110]. Para hydrogen, with $I = 0$ and negative parity of the spin function, must have rotational functions with $J = 0,\ 2,\ 4,\ \cdots$, so that the overall product gives a negative parity for the total wavefunction. Between these two kinds of hydrogen, which can be separated from each other macroscopically, transitions are rather strictly forbidden. Only transitions within term system with even J and within that with odd J are possible, if the nuclei are completely uncoupled. The weak coupling between the nuclear spins and the electronic shells does, however, make transitions between the two systems probable, with a very small transition probability.

At the lowest temperatures, only p-H_2 is stable; o-H_2, due to its $J = 1$, i.e. because a rotational quantum is excited, is metastable. The spontaneous conversion of o-H_2 into p-H_2 by flipping of a nuclear spin occurs very slowly, over a time of years. This process can be accelerated by addition of paramagnetic materials or other catalysts, thus pure p-H_2 can be prepared at low temperatures [111–113]. Normally, thermal equilibrium is established between the two H_2 modifications. Hydrogen is a mixture of p-H_2 and o-H_2 in the ratio of $1:3$.

2.5 Multiphoton spectroscopy of molecular species

The realisation that an atom or molecule must be capable to undergo a coherent (i.e. simultaneous) multiphoton transition when placed in a sufficiently intense radiation field goes back as further as the beginning of quantum mechanics [114]. In fact, Raman scattering in one well-known example of a multiphoton process which dates back that time. However, experimental demonstration of multiphoton absorption in an isolated molecule had to wait until the development of the laser which produces a sufficient intensity to compensate for the intrinsic weakness

of such transitions.

Although there are many variants of the multiphoton spectroscopy experiment, the vast majority of such experiments use the resonance-enhanced multiphoton ionisation (REMPI) technique. As will be explained in the next section, the figure 2.3 outlines one of the simplest and most practised types of REMPI experiment. In this particular example, the molecular species of interest needs to absorb a minimum of three photons in order for it to be excited from its ground state $|1\rangle$ to an energy above its ionisation limit. The probability of such a three-photon excitation can be greatly enhanced when there a real excited state of the neutral molecule resonant at the energy of one ot two absorbed photons. The particular case shown assumes that there is an excited state $|2\rangle$ resonant at the energy $2\mathrm{h}\nu$. Resonance is necessary, however not enough for state $|2\rangle$ to cause enhanced ionisation following excitation. The other requirements are that the $|2\rangle \leftarrow |1\rangle$ two-photon excitation has a nonzero transition probability and the state $|2\rangle$ needs to be sufficiently long lived that the subsequent one-photon ionisation step has reasonable probability. Once these conditions are fulfilled, the spectrum attained by measuring the ion yeild (or the yield of the accompanying photoelectrons) as a function of excitation wavelength will produce a signature of the $|2\rangle \leftarrow |1\rangle$ two-photon transition in the neutral molecule.

Now, let us consider what determines two-photon (or high-order) transition probabilities. Just as with the more traditional one-photon spectroscopy, symmetry considerations are paramount. A multiphoton transition between two states $|1\rangle$ and $|2\rangle$ will be allowed if the transition moment [115]:

$$\langle 2|\mathrm{T}_q^k(\hat{\mathrm{O}})|1\rangle \tag{2.22}$$

is nonzero, i.e. if the product of the irreducible representations for the wavefunctions of state $|1\rangle$ and $|2\rangle$ and of $\mathrm{T}_q^k(\hat{\mathrm{O}})$- the qth component of the spherical tensors of rank k representing the multiphoton transition operator $\hat{\mathrm{O}}$- includes the totally symmetric representation. Symmetry

considerations impose that only spherical tensors of either odd or even rank will contribute to any one-colour multiphoton excitation. Therefore, for instance, as one-photon electric-dipole transitions must be carried by components of rank one, only components of rank k = 0 and/or 2 can contribute to two-photon transitions induced employing photons of identical frequency and polarization. The k = 0 component (a scalar) can merely contribute to a two-photon transition linking states of the same symmetry. The identification of $k \neq 0$ components in two-photon excitation spectra is generally quite straightforward since they are forbidden, and thus not appears when the spectrum is recorded employing circularly polarized light. Sensitivity to the polarisation state of the exciting radiation is one important feature differentiating one-photon and multiphoton transitions [116]. As tables 2.3 and 2.4 illustrates, for all but the least symmetric molecules, at least some of the $k \neq 1$ components will span representations different from, or additional to, those of the dipole moment operator. Resultantly, multiphoton excitations can provide a means of populating excited states via transitions not allowed in traditional one-photon absorption spectroscopy.

Less selective selection rules are merely one of several advantages stems from the use of multiphoton excitation methods; operational convenience is another one. A multiphoton excitation achieved employing visible or near ultraviolet photons can frequently provide a ready means of populating an excited state lying energies which, in one-photon absorption, would corresponds to technically more demanding vacuum ultraviolet spectral region. On the other hand, multiphoton excitation cross-sections are relatively small; representative values for two- and three-photon absorption cross-sections are 10^{-50} cm^4 s^{-1} and 10^{-84} cm^4 s^{-2}, respectively [117]. Whereas these values are typically around 10^{-17} cm^2 for the cross section for an electric dipole allowed one-photon excitation between two bound states of a molecule. Multiphoton transitions are observed by using high laser intensities to compensate for the small cross section. For most spectroscopic applications, the required intensities are generated by focusing the output of conventional tunable dye lasers with nanosecond pulse duration. The interaction is

concentrated in a localized volume, which is the focal volume of the beam, therefore rendering the technique potentially matched for use with supersonic molecular beams.

According to the selection rules for electric dipole transitions, as shown in table 2.3 and 2.4, conventional one-photon absorption spectroscopy will never disclose the entire manifold of excited electronic states of a molecule. Additional information can often be determined if it is possible to study these same systems in emission. Whereas, multiphoton excitation spectra can reveal much more information about the system. This is most obvious in the case of homonuclear diatomic molecules such as H_2, N_2, O_2 and halogens; these all have *gerade* electronic ground state. As a result, one photon spectroscopy has tended to discriminate in favour of their *ungerade* excited states. Two-photon spectroscopy, in contrast, will excite g $\Leftrightarrow$ g and u $\Leftrightarrow$ u transitions; new spectroscopic data on the *gerade* excited states of each of the above homonuclear diatomics has been derived in this way [118–120]. REMPI technique is increasingly finding applications outside the spectroscopic community. For instance, multiphoton ionisation of H_2, resonance enhanced at the the two-photon energy by the levels of the E,F double minimum state, is being employed to detect H_2 products arising in the H + H_2 reactions [121, 122].

	Rank transition tensor k			
Quantum number and property of interest	0	1	2	3
Atoms; orbital angular momentum, l, of electron being excited	$\Delta l = 0$	$\Delta l \pm 1$	$\Delta l = 0, \pm 2$ (but s $\not\Leftrightarrow$ s)	$\Delta l = \pm 1, \pm 3$ (but s $\not\Leftrightarrow$ p)
Linear molecules [case (a)/(b)]; axial projection of electronic orbital momentum, Λ	$\Delta\Lambda = 0$	$\Delta\Lambda = 0, \pm 1$	$\Delta\Lambda = 0, \pm 1, \pm 2$	$\Delta\Lambda = 0,$ to ± 3
Linear molecules [case (c)]; axial projection of total electronic angular momentum, Ω	$\Delta\Omega = 0$	$\Delta\Omega = 0, \pm 1$	$\Delta\Omega = 0, \pm 1, \pm 2$	$\Delta\Omega = 0,$ to, ± 3
Centrosymmetric molecules; inversion symmetry, u/g	u $\Leftrightarrow$ u g $\Leftrightarrow$ g	u $\Leftrightarrow$ g	u $\Leftrightarrow$ u; g $\Leftrightarrow$ g	u $\Leftrightarrow$ g
Atoms and molecules; total angular momentum, J	$\Delta J = 0$	$\Delta J = 0, \pm 1$ (but $J = 0 \not\Leftrightarrow J = 0$)	$\Delta J = 0, \pm 1, \pm 2$ (but $J = 0 \not\Leftrightarrow J = 0, 1$)	$\Delta J = 0, \pm 3$ (but $J = 0 \not\Leftrightarrow J = 0, 1, 2$; $J = 1 \Leftrightarrow J = 1$)
Total parity, $+/-$	$+ \Leftrightarrow +$	$+ \Leftrightarrow -$	$+ \Leftrightarrow +$	$+ \Leftrightarrow -$
Electron spin, S	$\Delta S = 0$	$\Delta S = 0$	$\Delta S = 0$	$\Delta S = 0$

Table 2.3: Allowed changes in some of the more important quantum numbers and symmetry descriptors for atoms and molecules undergoing one-colour multiphoton transition. These transitions involve one ($k = 1$), two ($k = 0$ and 2), and three ($k = 1$ and 3) photons [115].

Number of photons, n	k	q	$D_{\infty h}$(a)	D_{6h}	D_{3h}(b)
1	1	0	Σ_u^+	A_{2u}	A_2''
	1	±1	Π_u	E_{1u}	E'
2	0	0	Σ_u^+	A_{1g}	A_1'
	2	0	Σ_u^+	A_{1g}	A_1'
	2	±1	Π_g	E_{1g}	E''
	2	±2	Δ_g	E_{2g}	E'
3	1	0	Σ_u^+	A_{2u}	A_2''
	1	±1	Π_u	E_{1u}	E'
	3	0	Σ_u^+	A_{2u}	A_2''
	3	±1	Π_u	E_{1u}	E'
	3	±2	Δ_u	E_{2u}	E''
	3	±3	Φ_u	$B_{1u} + B_{2u}$	$A_1' + A_2'$

Table 2.4: Representation of the spherical tensor components $T_q^k(\hat{O})$ of the one-colour, n-photon (n = 1 – 3) transition operator [115].

2.6 State selective detection via REMPI

In this section, state selective detection via the $(2+1)$ REMPI process will be discussed. Molecular hydrogen, having only two electrons, is the simplest neutral diatomic molecule. The determination of the internal state distribution of H_2 is of fundamental importance in numerous applications, ranging from H atom recombination on surfaces [123], H + H_2 reactive scattering [124] to hydrogen plasmas [125]. Molecular hydrogen shows only a weak quadrupole-allowed infrared spectrum and its lowest-lying electronic states are located in the deep vacuum ultraviolet range (≤ 100 nm) [126]. Consequently, standard methods for determining the internal

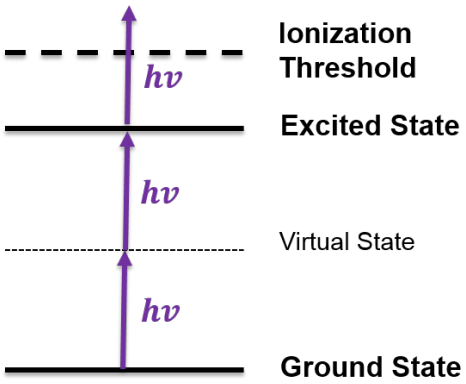

Figure 2.3: $(2+1)$ REMPI process energy diagram. The REMPI technique typically involves either a resonant single photon, or multiple photon absorption via a virtual (intermediate) state, to an electronically excited state, followed by another photon which ionises the atom or molecule.

state distribution of the molecule, such as infrared chemiluminescence [127] or Laser-induced fluorescence (LIF) [128] are either inapplicable or present formidable technical challenges. Although it is possible to detect H_2 in a quantum-state-specific manner by Raman or Coherent Anti-Stokes Raman Scattering (CARS) spectroscopy [129], signal-to-noise limitations prevent the use of these techniques at low densities (below 10^{12} molecules/cm^3) . On the other hand, Resonant Enhanced Multiphoton Ionization (REMPI) has very high sensitivity because the ions produced can be collected with high efficiency. Thus, this method can be applied to the measurement of highly rarefied gas flows below number densities of 10^{12} molecules/cm^3. This is too small to detect by conventional methods like LIF [130]. Therefore, REMPI is the most suitable method for our attempt to detect the vibrationally excited H_2 molecules in the non-equilibrium plasma discharge.

REMPI is a well-known technique in laser spectroscopy [132, 133]. In this method, two or more photons are used to excite and ionise the molecule, starting from specific ro-vibrational

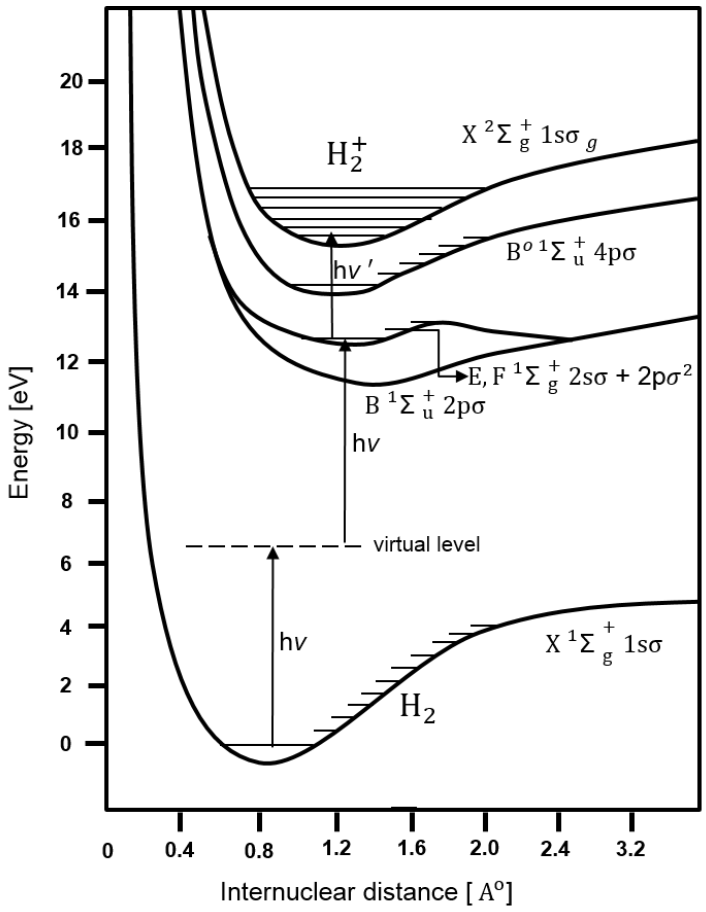

Figure 2.4: Potential energy curves for some electronic states of H_2 and H_2^+. The excitation and ionization steps for the $(2 + 1)$ REMPI process used in our work are also shown (Figure adapted from reference [131]).

levels. If the energy of one or more photons corresponds to the energy difference between the electronic ground state level and an allowed real excited level (resonant process), then the cross section for ionisation is much larger than for non-resonant multiphoton ionisation. If more than one photon is necessary for the excitation process, two-photon absorption occurs via so called virtual (intermediate) states as shown in Figure 2.3 [131]. For such a process to occur, since

the lifetime of the molecule in the virtual state is short ($\sim 10^{-15}$ s) and two photons have to be absorbed within that period of time, it requires a sufficiently high laser intensity. By tuning the laser wavelength and measuring the produced ion signals as a function of the wavelength, information about the population of the different quantum states in the electronic ground state can be obtained [134].

The particular REMPI process applied for the hydrogen molecule in our work is demonstrated in the potential energy level diagram [131] in Figure 2.4. The E, $F^1\Sigma_g^+$ state is the lowest electronically excited level that can be reached by absorption of two identical photons (UV) from the ground state $X^1\Sigma_g^+$ according to the symmetry selection rules as shown in table 2.3. Since the energy difference between these states is of the order of 12.5 eV, the wavelength of the laser has to be around 200 nm. For subsequent ionisation of the excited molecule, one photon from the same source is sufficient. Such an excitation process is described as a $(2 + 1)$ REMPI process. For a $(1 + 1)$ REMPI process, excitation in to the $B^1\Sigma_u^+$ state is possible according to the selection rules, however laser radiation of around 100 nm is required [135]. For a change of vibrational quantum number during the electronic excitation, Franck-Condon factors [136] govern the transition strength. Franck-Condon principle states that when an electronic transition takes place, the time scale of this transition is so fast compared to nucleus motion that it is considered that the nucleus to static, and the vibrational transition from one vibrational state to another one is more likely to occur if wave functions of these states have a large overlap. The degree of overlap of the wave functions for the ground state and excited state of the oscillator give us the Franck-Condon factors. Whereas the rotational quantum number has to change according to $\Delta J = 0, \pm 1$ for a one-photon process. That means that for the two-photon process employed in this work, the change of the rotational quantum number has to be -2, 0 or $+2$ [137] shown in table 2.3. Excitations of these kinds are represented as O-branch, Q-branch and S-branch transitions respectively. A Q-branch transition from an initial vibrational state v_i and rotational state J in the electronic ground state, to the final vibrational state v_f in the

electronically excited E, F state, is then labelled $Q_J(v_f, v_i)$. In the next section, the extraction of the rovibrational populations from $(2+1)$ REMPI process will be discussed.

2.7 Extracting ro-vibrational populations from $(2+1)$ REMPI measurements

The population of the rovibrational levels in the electronic ground state can be determined from the ion yield. Operating far from the saturation of the $(2+1)$ process, the ion yield N_i is approximately given by [138]:

$$N_i = C N_0 \sigma_{2ph} I_{ex}^2 \frac{\sigma_{ion} I_{ion}}{\sigma_{ion} I_{ion} + A}, \tag{2.23}$$

where N_0 denotes the ground rovibronic state number density and C is the instrumental ion detection efficiency. σ_{2ph} and σ_{ion} are the cross sections for the two-photon excitation process and the ionisation process respectively. Typical cross sections for single-photon excitation are 10^{-17} to 10^{-18} cm^2 and for two-photon processes 10^{-30} – 10^{-36} cm^{4}W^{-1} [139]. I_{ex} and I_{ion} are the photon flux densities for excitation (200 nm radiation) and ionisation and A is the spontaneous fluorescence decay rate from the excited E, F state. The spontaneous decay rate for the E, F state is of order 10^7 s^{-1} corresponding to a lifetime of ≈ 100 ns [131]. If the two-photon excitation proceeds without saturation, a quadratic energy dependence on the intensity of 200 nm light should be observed according to Equation 2.23. The ionisation step is assumed saturated. Hence, we can use ion yield as a measure of the ground rovibrational state populations.

The rovibrational state population for a thermalized gas at temperature T is given by:

$$N(J,v) = \frac{g_n(2J+1)\exp\left(\frac{-E_{rot}(J,v)-E_{vib}(v)+E_{vib}(0)}{k_B T}\right)}{\Sigma_{J,v} N(J,v)}, \tag{2.24}$$

with:

$$E_{\text{rot}}(J,v) = \left[B_e - \alpha\left(v+\frac{1}{2}\right)\right] J(J+1) - DJ^2(J+1)^2, \tag{2.25}$$

$$E_{\text{vib}}(v) = \omega\left(v+\frac{1}{2}\right) - \omega_x(v+\frac{1}{2})^2. \tag{2.26}$$

According to Huber and Herzberg [140], the constants for hydrogen molecules (in cm^{-1}) are: B_e = 60.85, α = 3.062, D = 4.71×10^{-2}, ω = 4401.21, ω_x = 121.34. Here g_n denotes the spin degeneracy and is equal to 3 for odd numbers and 1 for even J – numbers.

In order to avoid excessive indices, in the spectroscopy literature the upper state $(v_{\text{f}}, J_{\text{f}})$ is always labelled with a prime as (v', J'), whereas the lower state $(v_{\text{i}}, J_{\text{i}})$ is labelled with a double prime as (v'', J''). In the rest of this Thesis the corresponding transitions will be labelled accordingly.

In Table 2.5 the calculated relative ro-vibrational state population for the levels v'' = 0, J'' = 0 – 9 and v' = 1, J' = 0 – 9 at T = 300 K are compiled. At room temperature and in equilibrium, v' = 1 vibrational level populations are not significant compared to the v'' = 0 vibrational level. In addition, the photon wavelength for the specific two-photon resonant excitation from the electronic ground state to the E, F state is quoted. The transition wavelengths are calculated using term values as described below. Just as in the ground electronic state, a molecule may vibrate and rotate in the excited states. The term value S for a molecule with an electronic term value T_e, corresponding to an electronic transition between equilibrium configurations and with vibrational and rotational term values $\text{G}(v)$ and $\text{F}(J)$ respectively, is given by [141]:

$$\text{S} = \text{T}_\text{e} + \text{G}(v) + \text{F}(J). \tag{2.27}$$

$Q_{J''}(v', v'')$	λ(nm)	$N(J'', v'')$
$Q_0(0,0)$	201.67	0.1287
$Q_1(0,0)$	201.78	0.6564
$Q_2(0,0)$	202.00	0.1177
$Q_3(0,0)$	202.33	0.0919
$Q_4(0,0)$	202.77	0.0043
$Q_5(0,0)$	203.32	0.0010
$Q_6(0,0)$	203.96	0.0000
$Q_7(0,0)$	204.69	0.0000
$Q_8(0,0)$	205.52	0.0000
$Q_9(0,0)$	206.42	0.0000
$Q_0(1,1)$	205.46	0.0281×10^{-8}
$Q_1(1,1)$	205.57	0.1473×10^{-8}
$Q_2(1,1)$	205.79	0.0280×10^{-8}
$Q_3(1,1)$	206.12	0.0239×10^{-8}
$Q_4(1,1)$	206.55	0.0013×10^{-8}
$Q_5(1,1)$	207.09	0.0003×10^{-8}
$Q_6(1,1)$	207.73	0.0000×10^{-8}
$Q_7(1,1)$	208.45	0.0000×10^{-8}
$Q_8(1,1)$	209.26	0.0000×10^{-8}
$Q_9(1,1)$	210.15	0.0000×10^{-8}

Table 2.5: Ro-vibrational state population $N(J'', v'')$ of H_2, calculated for v'' = 0, J'' = 0 – 9 and v'' = 1, J'' = 0 – 9 at T = 300 K, and the corresponding laser wavelengths necessary for the $(2 + 1)$ REMPI process.

The vibrational term values for any electronic state, ground or excited, can be expressed as:

$$\mathrm{G}(v) = \omega_\mathrm{e}\left(v+\frac{1}{2}\right) - \omega_\mathrm{e}x_\mathrm{e}\left(v+\frac{1}{2}\right)^2, \tag{2.28}$$

where the vibration wavenumber ω_e and the anharmonic constants $\omega_\mathrm{e}x_\mathrm{e}$ vary from one electronic state to another. The rotational term values for any Σ state are given by:

$$\mathrm{F}(J) = B_v J(J+1) - D_\mathrm{e}J^2(J+1)^2, \tag{2.29}$$

where B_v is the rotational constant, D_e is the centrifugal distortion constant, and the superscript "v" indicates the vibrational dependence.

Only the v – dependence of B_v is important here and it is given by:

$$B_v = B_\mathrm{e} - \alpha_\mathrm{e}\left(v+\frac{1}{2}\right), \tag{2.30}$$

as for the ground state. The constants B_e, α_e and D_e are characteristic of a particular electronic state in the ground or excited state. The corresponding diatomic constants of H_2 molecules for the ground electronic state $X^1\Sigma_g^+$ and the excited electronic state $\mathrm{E,F}^1\Sigma_g^+$ are given in Table 2.6 [142].

State	T_e	ω_e	$\omega_\mathrm{e}x_\mathrm{e}$	B_e	α_e	D_e
$X^1\Sigma_g^+$	0	4401.20	121.33	60.853	3.062	0.0471
$\mathrm{E,F}^1\Sigma_g^+$	100082.3	2588.9	130.5	32.68	1.818	0.0228

Table 2.6: The diatomic constants of H_2 molecules for the ground electronic state and the excited electronic state. All of the constants are given in wavenumber units $[\mathrm{cm}^{-1}]$.

If the rotational energy distribution follows the Maxwell-Boltzmann distribution, the rotational line intensity in the H_2 molecule $(2+1)$ REMPI spectra is given by [143]:

$$I_{J',J''} = Ag(J'')S(J',J'')\exp\left(\frac{-E_\mathrm{rot}}{k_\mathrm{B}T_\mathrm{rot}}\right). \tag{2.31}$$

Here A is a constant independent of the rotational quantum number J'' of the ground state and J' of the excited (resonance) state, but including laser flux, number density and vibrational strength (Franck-Condon factor). Here $g(J'')$ is the nuclear spin degeneracy depending on the parity of J'' and the spin I_s of the nuclei [75]. For H_2 $(I_s = 1/2)$, it takes the values 3 and 1 for odd and even J'' respectively. $S(J', J'')$ is the rotational transition strength (two-photon Honl-London factor). The two-photon Honl-London factors for the ${}^1\Sigma_g^+ \leftarrow {}^1\Sigma_g^+$ transition [144] are shown in Table 2.7, with the assumption that the ratio of the transition dipole factor is $(\mu_s/\mu_l) = 1$ [143].

Branch	$S(J', J'')$
O$(J' - J'' = -2)$	$\frac{J''(J''-1)}{30(2J''-1)}$
P$(J' - J'' = -1)$	0(forbidden)
Q$(J' - J'' = 0)$	$\frac{2J''+1}{9}\left\{1 + \frac{J''(J''+1)}{5(2J''-1)(2J''+3)}\right\}$
R$(J' - J'' = 1)$	0(forbidden)
S$(J' - J'' = 2)$	$\frac{(J''+1)(J''+2)}{30(2J''+3)}$

Table 2.7: Two-Photon Honl-London factors for the ${}^1\Sigma_g^+ \leftarrow {}^1\Sigma_g^+$ transition using linearly polarized light.

The transition probability via P or R-branch transition is zero, because the transition of $J' - J'' = \pm 1$ is forbidden for ${}^1\Sigma_g^+ \leftarrow {}^1\Sigma_g^+$ by two-photon absorption. The term $\exp(-E_{rot}/k_B T_{rot})$ indicates the Maxwell-Boltzmann distribution at the rotational temperature T_{rot}. k_B is the Boltzmann constant and E_{rot} the rotational energy of the ground state. E_{rot} is a function of J'' as given in Equation 2.25. In the next section, the simulation of H_2 $(2 + 1)$ REMPI spectra at room temperature will be explained.

2.8 Simulation of H_2 $(2+1)$ REMPI spectra

This section presents simulations of the H_2 rovibrational spectra. Calculating H_2 spectrum involves two main parts. The first part is to calculate the transition wavelengths for the corresponding rovibrational states. The second is to determine the corresponding line intensities including the line profiles, to take into account of line broadening mechanisms.

2.8.1 Transition wavelengths for H_2 $(2+1)$ REMPI spectra

As discussed in section 2.7, the transition wavelengths are calculated using the term values for the H_2 molecule. Our study investigates the $(2+1)$ REMPI process in H_2 by excitation from the ground electronic state $X^1\Sigma_g^+$ to the excited electronic state $E, F^1\Sigma_g^+$ and subsequent ionisation. Therefore, we need to establish the term values for the ground and excited states of H_2 molecule.

The rotational term value for the ground electronic state is given as:

$$F(J'') = \left[B_e - \alpha_e\left(v'' + \frac{1}{2}\right)\right] J''(J''+1) - D_e J''^2 (J''+1)^2. \tag{2.32}$$

The vibrational term value for the ground electronic state is expressed in the equation 2.28 and it will be represented as $G(v'')$.

Before introducing the rotational term values for the excited electronic state, we need to take into account the selection rules. Due to these rules, there would be O-branch, Q-branch and S-branch transitions. Therefore, the rotational term values of the excited electronic state for these three transitions can be defined as $F_Q(J_1')$, $F_O(J_2')$, and $F_S(J_3')$ where $J_1' = J''$, $J_2' = J'' - 2$ and $J_3' = J'' + 2$.

The vibrational term value for the excited electronic state be calculated using the equation 2.28 and it will be represented as $G(v')$.

After defining the ground and excited state rovibrational term values, now we can define the total term values.

The total term values for the ground state is expressed in the equation 2.27 and will be defined as S''.

The total term values for the excited state for Q-branch, O-branch, and S-branch are expressed as:

$$S'_Q = T'_e + G(v') + F_Q(J'_1), \tag{2.33}$$

$$S'_O = T'_e + G(v') + F_O(J'_2), \tag{2.34}$$

$$S'_S = T'_e + G(v') + F_S(J'_3). \tag{2.35}$$

Now that we have established the total term values for the ground and excited states, the transition energies can simply be calculated by subtracting the ground state total term values from the excited state total term values. Thus, the transition energies for Q-branch, O-branch, and S-branch are given as:

$$\nu_Q = S'_Q - S'', \tag{2.36}$$

$$\nu_O = S'_O - S'', \tag{2.37}$$

$$\nu_S = S'_S - S'', \tag{2.38}$$

Because two-photon absorption is required to excite the molecule for our $(2+1)$ REMPI process, we need to divide the transition energies by 2 in order to determine the laser wavelength for this process.

Note, up to this point, all of our calculations are conducted in cm^{-1} units using the diatomic constants for H_2 molecules in table 2.6.

2.8.2 Line intensities for H_2 $(2+1)$ REMPI spectra

The rotational line intensity, where the rotational energy distribution follows the Maxwell-Boltzmann distribution, is given by equation 2.31. In this equation, the line intensities mainly depend on the vibrational strength, also known as Franck-Condon factor, the rotational transition strength, which is also called two-photon Honl-London factor, and the state populations determined by Maxwell-Boltzmann distribution. However, in our calculations vibrational strength factor is not included because we produce our $(2+1)$ REMPI spectra using rovibrational transitions with the same vibrational state; thus, the vibrational strength factor is assumed to be constant for each rotational transition. Consequently, our calculations assume relative intensities depending on merely the Honl-London factors and Maxwell-Boltzmann distribution factor.

For our line intensity calculations, the relative rovibrational state populations are initially determined using the following expression:

$$N = g(J'')\exp\left(\frac{-(\mathrm{G}(v'') + \mathrm{F}(J''))}{k_{\mathrm{B}}T}\right), \tag{2.39}$$

where $g(J'')$ is the spin degeneracy and equals to 3 for odd or 1 for even J'' – numbers. $\mathrm{G}(v'')$ and $\mathrm{F}(J'')$ are the ground state vibrational and rotational term respectively. k_{B} is Boltzmann constant and T is the temperature.

The two-photon Honl-London factors are shown in table 2.7 for Q-branch, O-branch and S-branch.

After establishing the rotational line strengths, we now can establish the line intensity expression involving both the Honl-London factors and Maxwell-Boltzmann factor. Therefore, the line intensities for each branch are expressed as:

$$I_{\mathrm{Q}}(J', J'') = S_{\mathrm{Q}}(J', J'')N, \tag{2.40}$$

$$I_{\mathrm{O}}(J', J'') = S_{\mathrm{O}}(J', J'')N, \tag{2.41}$$

$$I_{\mathrm{S}}(J', J'') = S_{\mathrm{S}}(J', J'')N, \tag{2.42}$$

where $I_{\mathrm{Q}}(J', J'')$, $I_{\mathrm{O}}(J', J'')$ and $I_{\mathrm{S}}(J', J'')$ are the line intensities for Q-branch, O-branch and S-branch respectively.

2.8.3 Line broadening for H_2 $(2+1)$ REMPI spectra

Real spectral lines are broadened. Three broadening mechanisms determine the spectral profile, $\phi(\nu)$. One of these mechanisms occurs due to quantum mechanical uncertainty in the energy of levels with finite lifetimes. This type of broadening is called natural or lifetime broadening, and is generally relatively small. The second type of the broadening mechanism is called collisional or pressure broadening. Collisions reduce the effective lifetime of a state; thus, this leads to broader spectral lines. High pressure also indicates that more collisions occur in a gas; consequently, this results in broader spectral lines. The other broadening mechanism is

Doppler thermal broadening, due to the thermal (or large scale turbulent) motion of individual atoms or molecules in a gas relative to the observer.

Although the dominant broadening is Doppler broadening in our work, we will give a brief description of each, and focus on the Doppler broadening.

Natural broadening

The uncertainty principle states that energy levels above ground state with energy E and lifetime Δt, has an uncertainty in energy expressed as:

$$\Delta E \Delta t \approx \hbar. \tag{2.43}$$

This means short-lived states have large uncertainties in their energy. Therefore, a photon emitted in a transition from this level to the ground state will have a range of possible frequencies given as:

$$\Delta \nu \approx \frac{\Delta E}{h} \approx \frac{1}{2\pi \Delta t}. \tag{2.44}$$

This effect is called natural broadening.

If the spontaneous decay of a state n'(to all lower energy levels n'') proceeds at a rate expressed as:

$$\gamma = \Sigma_{n''} A_{n'n''},$$

it can be shown that the line profile for transitions to the ground state is of the form:

$$\phi(\nu) = \frac{\gamma/4\pi^2}{(\nu - \nu_0)^2 + (\gamma - 4\pi)^2}. \tag{2.45}$$

This is called a Lorentzian or natural line profile.

Pressure (Collisional) broadening

Collisions randomize the phase of emitted radiation. If the collisions are frequent enough, they effectively shorten the lifetime further. Thus, this results in pressure or collisional broadening of spectral line. If the frequency of collisions is ν_{col}, then the line profile is as follows:

$$\phi(\nu) = \frac{\Gamma/4\pi^2}{(\nu - \nu_0)^2 + (\Gamma - 4\pi)^2}. \tag{2.46}$$

where $\Gamma = \gamma + 2\nu_{\text{col}}$. As seen, this is still a Lorentz line profile. Collisions dominate at high density, meaning high pressure.

Doppler broadening

Doppler broadening is typical in gaseous samples. As a well known fact, the Doppler effect results in a light frequency shift when the source is moving toward, or away from the observer. When a source emitting radiation with frequency ν_0 moves with a speed v_{z}, the observer detects radiation with a frequency as:

$$\nu = \nu_0 \left(1 \pm \frac{v_{\text{z}}}{\text{c}}\right), \tag{2.47}$$

where the sign + and − is related to an approaching and receding source, respectively.

Molecules in a gas randomly move in all directions and the observer detects the corresponding Doppler broadened spectral profile. This profile reflects the distribution of molecular velocities along the line of detection which can be designated a z – axis for simplicity.

In the case of thermal equilibrium the velocity distribution is the Maxwell-Boltzmann distribution:

$$n(v_{\text{z}})\text{d}v_{\text{z}} = \sqrt{\frac{2k_{\text{B}}T}{\pi\text{m}}}\exp\left(-\frac{\text{m}v_{\text{z}}^2}{2kT}\right), \tag{2.48}$$

where $n(v_z)dv_z$ is the relative number of atoms or molecules with velocity component v_z parallel to the light beam and m is the particle mass.

By combining equations 2.47 and 2.48, we obtain the expression for the light intensity as a function of ν:

$$I(\nu) = I_0\sqrt{\frac{4\ln 2}{\pi}}\frac{1}{\Delta\nu_D}\exp\left(-4\ln 2\frac{(\nu-\nu_0)^2}{\Delta\nu_D^2}\right) \quad \text{where} \quad \Delta\nu_D = \frac{2\nu_0}{c}\sqrt{\frac{2\ln 2kT}{m}}. \tag{2.49}$$

where $\Delta\nu_D$ is the Doppler width, full width at half maximum. The distribution (The Doppler profile) in equation 2.49 has a Gaussian form. It is seen that the Doppler width $\Delta\nu_D$ is proportional to the transition frequency ν_0, to the square root of the gas temperature T, and inverse to the square root of the particle mass.

For transitions which belong to the visible or the near-UV spectral range, when the gas temperature is around 300 K, the Doppler width is typically within one GHz. However, Hydrogen atoms and molecules have exceptionally high Doppler widths of around 30 GHz due to their low mass (high velocity). For the visible part of the spectrum the Doppler line broadening is usually much larger than the lifetime broadening. Therefore, the experimentally obtained line profiles usually have Gaussian shape. In contrast, for microwave transitions, or in conditions of high collisional broadening, the lifetime broadening becomes larger than the Doppler one resulting in Lorentz-type line profiles.

In our calculations, we determined the Doppler broadening in wavelength instead of frequency solely due to convenience.

The Doppler width at full width at half maximum (FWHM) ,$\Delta\lambda$, is multiplied by a factor of 4 in our calculations for $(2+1)$ REMPI process since it is 2 photon process [145].

We now can rearrange the Doppler broadening profile using the transition wavelengths and line intensity equations 2.40, 2.41, and 2.42. Thus, the new expressions are given as:

$$I_{\mathrm{Q}}(\lambda) = I_{\mathrm{Q}}(J', J'')\frac{\mathrm{c}}{\lambda_{\mathrm{Q}}}\sqrt{\frac{\mathrm{m}}{2\pi kT}}\exp\left(-\frac{4\ln 2(\lambda-\lambda_{\mathrm{Q}})^2}{(\Delta\lambda_{\mathrm{Q}})^2}\right),\ \Delta\lambda_{\mathrm{Q}} = 4\left(\frac{2\lambda_{\mathrm{Q}}}{\mathrm{c}}\sqrt{\frac{2\ln 2kT}{\mathrm{m}}}\right), \quad (2.50)$$

$$I_{\mathrm{O}}(\lambda) = I_{\mathrm{O}}(J', J'')\frac{\mathrm{c}}{\lambda_{\mathrm{Q}}}\sqrt{\frac{\mathrm{m}}{2\pi kT}}\exp\left(-\frac{4\ln 2(\lambda-\lambda_{\mathrm{O}})^2}{(\Delta\lambda_{\mathrm{O}})^2}\right),\ \Delta\lambda_{\mathrm{O}} = 4\left(\frac{2\lambda_{\mathrm{O}}}{\mathrm{c}}\sqrt{\frac{2\ln 2kT}{\mathrm{m}}}\right), \quad (2.51)$$

$$I_{\mathrm{S}}(\lambda) = I_{\mathrm{S}}(J', J'')\frac{\mathrm{c}}{\lambda_{\mathrm{S}}}\sqrt{\frac{\mathrm{m}}{2\pi kT}}\exp\left(-\frac{4\ln 2(\lambda-\lambda_{\mathrm{S}})^2}{(\Delta\lambda_{\mathrm{S}})^2}\right),\ \Delta\lambda_{\mathrm{S}} = 4\left(\frac{2\lambda_{\mathrm{S}}}{\mathrm{c}}\sqrt{\frac{2\ln 2kT}{\mathrm{m}}}\right), \quad (2.52)$$

where $I_{\mathrm{Q}}(\lambda)$, $I_{\mathrm{O}}(\lambda)$, and $I_{\mathrm{S}}(\lambda)$ are the line intensities of the Doppler broadened profiles and $\Delta\lambda_{\mathrm{Q}}$, $\Delta\lambda_{\mathrm{O}}$, and $\Delta\lambda_{\mathrm{S}}$ are Doppler width at FWHM of $(2+1)$ REMPI process for Q-branch, O-branch, and S-branch respectively.

As discussed, natural broadening and pressure broadening effects are not included in our work because their contribution to the line broadening is negligible compared to the Doppler broadening. However, we include the laser linewidth to the line profiles since it has a significant contribution to the spectral line broadening. Therefore, our total line broadening is combination of Doppler linewidth and laser linewidth. We assumed our laser linewidth, which is around 2 GHz, has a Gaussian profile; thus, it is included in the Doppler profile by simply adding it to the Doppler width at FWHM for our simulation. The example of the H_2 $(2+1)$ REMPI spectra at room temperature will be presented in the results section.

Chapter 3

$(2+1)$ REMPI experiment and Results in the non-equilibrium discharge

3.1 Experimental setup

In this section, we will discuss the experimental setup for our H_2 $(2+1)$ REMPI experiment in the non-equilibrium discharge. In addition, it will be implemented with a slight modification for the room temperature measurements. The experimental setup includes the laser system, optical layout, discharge cell and detection of the REMPI signal as well as the data acquisition process.

Tunable light (598 nm to 630 nm) is produced by a Rhodamine $610/640$ dye laser (Cobra-Stretch, Sirah GmbH, Germany), which is pumped by a frequency doubled Nd:YAG laser (Precision II, Continuum, USA). A portion of the dye laser output (at ω) is frequency doubled, this is then mixed with the remaining fundamental to produce a tunable UV output at the third harmonic (3ω). After spectral filtering the UV output is sent to a H_2/Ne gas cell containing two electrodes (see below). The current produced from the UV photoionisation of H_2 is detected

via a signal averaging oscilloscope (see below) as a function of the laser wavelength (3ω) and stored on a laboratory PC.

3.1.1 Laser system

A schematic diagram of the experimental setup is depicted in Figure 3.2. The laser system consists of two main parts: one is a Nd:YAG laser (Continuum Precision II), which is used to pump the Sirah dye laser, and the Sirah dye laser combined with a frequency conversion unit (FCU).

Nd:YAG laser

At the heart of our Nd:YAG laser is very high efficiency pump chamber to couple the flashlamp light into the Nd:YAG rod. Through the use of a diffuse reflector concept, the Nd:YAG laser is able to produce high gain with low heat buildup in the overall system. Therefore, the pulsed output has a stable frequency doubled at 532 nm and an available pulse energy of 400 mJ/pulse. The pulse duration is 10 ns and its repetition rate is 10 Hz.

Dye laser

The Nd:YAG laser output is guided into the Sirah dye laser to generate the required tunable laser radiation. A dye mixture of Rhodamine 610 and 640 is used to yield a wavelength range of 598 nm to 630 nm with a peak at 615 nm. The dye mixture at the oscillator consists of Rhodamine 610 (RhB) + Rhodamin 640 (Rh101) with concentrations of 0.17 and 0.04 g/l respectively. The dye mixture is diluted by 1/8 at the amplifier. After the amplifier, a conversion factor of approximately 25% for the RhB + Rh101 dye mixture yields a subsequent dye laser output.

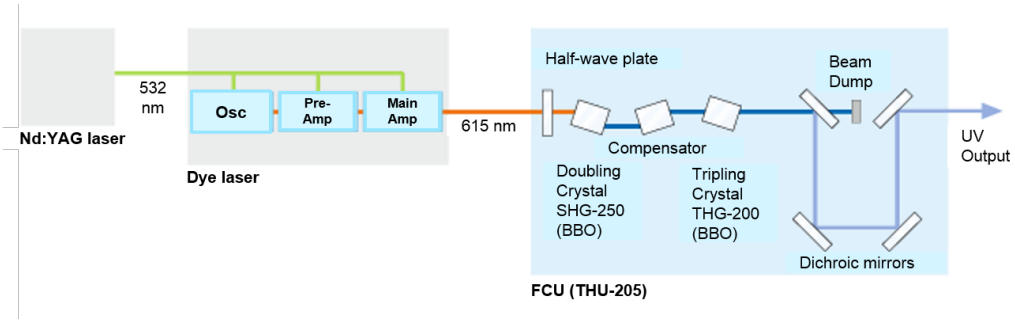

Figure 3.1: The FCU unit consists of two BBO type crystals: one is to generate the second (SHG-250) and the other one (THG-200) to generate the third harmonics of the fundamental dye laser wavelength. A half-wave plate is used to ensure the correct input polarisation for second harmonic generation. An optical compensator is used to correct for the beam shift induced by the second harmonic crystal.

Frequency conversion unit (FCU)

The Sirah FCU unit (THU-205), is designed to generate laser light in the UV wavelength range, from $197-210$ nm, by third harmonic generation (THG), as shown in figure 3.1. The dye laser is operated in the red spectral range, from 598 to 630 nm with a peak at 615 nm. Its output beam is intially frequency doubled by the FCU. Then, the resulting UV beam $(307.5$ nm$)$ is sum frequency mixed with the residual dye laser beam $(\approx 615$ nm$)$ to generate a frequency tripled beam $(\approx 205$ nm$)$. A set of 4 dichroic mirrors separate the generated UV beam $(205$ nm$)$ from the incoming light $(307.5$ nm and ≈ 615 nm$)$. Thus, we have our UV output which has a pulse energy about ≈ 1 mJ/pulse.

3.1.2 Optical layout

The optical setup is depicted in figure 3.2. After the FCU unit, the UV output still contains a small amount of residual fundamental wavelength $(615$ nm$)$. Therefore, a Pellin Broca prism

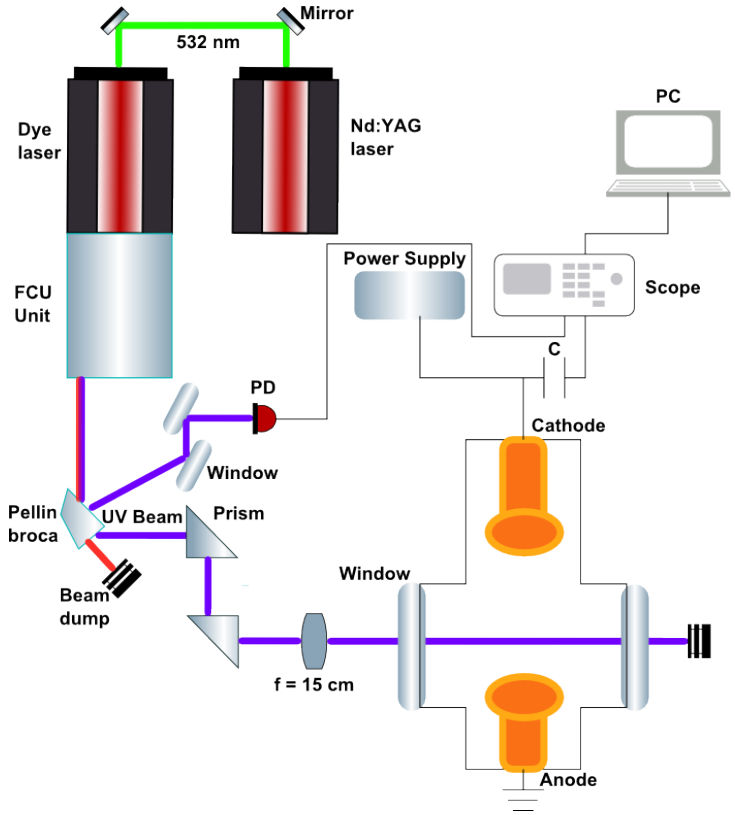

Figure 3.2: Experimental setup for H_2 $(2+1)$ REMPI experiment in the glow discharge cell. The diagram depicts the laser system combined with frequency conversion unit (FCU), optical layout and detection equipment.

is mounted at the exit of the FCU unit to separate the UV output beam $(205\ \text{nm})$ from the other wavelength. A lens is used to focus the UV output beam through a window mounted to the cell. In addition, the UV laser power was monitored on a photodiode. It should be noted that all the optics used in the UV beam optical layout have to be fused silica since ordinary glass would absorb the UV radiation.

3.1.3 Discharge cell

The $(2 + 1)$ REMPI experiment was realized in a glass cell as shown in figure 3.2. The glass cell was specifically designed to carry out the discharge experiment since a cell made of a conductive material may create unwanted discharge patterns from the electrodes to the cell walls. The glass cell, designed by our group and constructed by the UCL MAPS faculty workshop, is in the form of a 4-way cross that is 20 cm by 15 cm in length and has 3.2 cm outer diameter for each-way of the cell. Two UV fused silica windows are mounted to two sides of it in order to allow laser light to enter and exit the glass cell. In addition, two copper electrodes were designed for creating a glow discharge by applying a DC voltage across them. Copper was chosen due to its good conduction properties. The electrodes are circular in shape and 2 cm in diameter. The anode is grounded. Both electrodes are attached to a KF-25 flange which is mounted to the glass cell. The electrical feed-through is connected to the power supply and detection electronics through these flanges.

3.1.4 REMPI signal detection and data acquisition

REMPI signal detection

In our work the signal detection is conducted through the electrodes. Firstly, H_2^+ ions are produced by $(2 + 1)$ REMPI process and then they are collected via the cathode in the glass cell. To achieve this, the cathode is connected to a high voltage supply (Series EW, Glassman High Voltages, USA) and a negative voltage is supplied to the electrodes. By applying a potential difference across the electrodes, the laser induced H_2^+ ions are attracted to the cathode, thus a laser induced current is generated then it is collected, and measured on an oscilloscope (Wavepro 7300, LeCoy, USA). The oscilloscope is connected to the cathode using a BNC cable and capacitor $(4.7$ nF$)$ which can handle high voltage up to 2 kV. By placing the capacitor be-

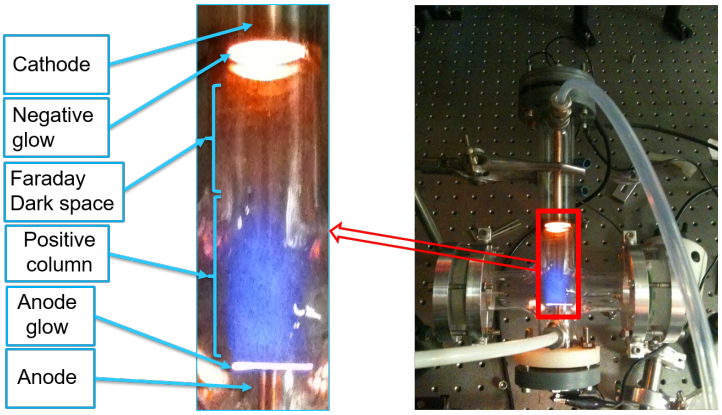

Figure 3.3: H_2 discharge and non-equilibrium positive column ($T_{\text{vib}} > T_{\text{trans}}$). The characteristic glow discharge regions are seen in the cell.

tween the cathode and scope, the latter is protected from the DC high voltage supplied by the power supply and additionally the high DC voltage is filtered from the laser induced ion signal created.

Glow discharge production

To produce H_2^+ ions, a DC glow discharge was produced in a gas mixture of 10% H_2 in Neon. To do that, the electrode separation is adjusted to be 5.5 cm. Then, a constant gas flow of the gas mixture at around $\approx$ 40 Torr pressure is maintained in the glass cell. It is crucial to have the constant gas flow in order to sustain the discharge at a constant voltage and current. After maintaining a constant gas flow in the cell, 500 volts and 23.5 mA are supplied across the electrodes. The optimum gas flow, pressure, and current characteristics for a stable discharge were found by trial and error. One can be certain that the discharge is stable when both the cathode and anode surfaces are covered by a uniform glow as depicted in figure 3.3. Some characteristic regions of the glow discharge are shown in figure 3.3. Amongst these discharge regions, the positive column is of the most importance to us because it has a non-equilibrium

characteristic ($T_{\text{vib}} > T_{\text{trans}}$). Therefore, the vibrationally excited H_2 molecules are produced in the positive column.

Data acquisition

After producing a stable glow discharge in the glass cell, we detect the vibrationally excited molecules. To achieve this, initially the dye laser is calibrated over the desired wavelength range, which requires tuning of both the SHG and THG crystals in the FCU unit. In order to obtain the rotationally resolved spectrum of vibrationally excited (v = 1) H_2, the tunable dye laser must have approximately the same intensity over the scanned wavelength range from $\approx$ 205 to 207 nm. During the data acquisition, the dye laser is scanned over the calibrated wavelength range with a 0.0004 nm, which is $\approx$ 3 GHz in frequency unit, step size to resolve the Doppler profile of the transition lines where Doppler linewidth is calculated to be $\approx$ 52 GHz using the equation 2.50 in section 2.8.3. The produced ion signals are plotted versus the corresponding laser wavelength. Each data acquisition cycle, which starts by firing a laser pulse and finishes when the ion signal produced is recorded, is initiated by a trigger pulse obtained from the pump laser (Nd:YAG laser) in our laser system. Additionally, the ion signal at each laser wavelength are averaged on the oscilloscope to reduce errors. The dye laser is scanned over a wavelength range which covers the first few rovibrationally excited states in the v' = 1 vibrational level. Primary measurements covered the wavelength range between 205.35 and the 206.60 nm. The calibrated wavelength range should be able to detect H_2 molecules in the v' = 1, J' = 0 – 3 rovibrational quantum states via the (2 + 1) REMPI process via the Q−branch lines of the $E, F^1\Sigma_g^+ - X^1\Sigma_g^+$ (1, 1) band. The H_2^+ ions produced by the (2 + 1) REMPI process are collected at the cathode and the signal is sent to the Lecoy oscilloscope for monitoring. The data collected via the Lecoy oscilloscope and recorded on a computer. The data acquisition is carried out by a Labview program developed by our group.

3.2 Characterization of H_2 via $(2+1)$ REMPI at 300 K

The characterization included investigating the $(2+1)$ REMPI signal's dependence on various parameters. These parameters consists of the pressure of the gas mixture, the voltage applied across the electrodes, the current and laser power. The main motivation for this experiment was to compare the measurements at room temperature with the expected theoretical calculations. Therefore, we could verify our methodology and apply the same methodology to the non-equilibrium discharge.

Experimental setup

The experimental setup for $(2+1)$ REMPI experiment at room temperature is the same as the experimental setup for the discharge experiment described in section 3.1. The only difference is the electrode used to collect the H_2^+ ions in the glass cell. In this case, two copper rods, which have 6.35 mm $(1/4'')$ diameter, were used with a separation of around 3 mm. A high voltage power supply, which is able to generate negative voltages up to 1000 V and current of 2 A, was used. Before the measurement, we applied a voltage just under the breakdown one, so that the laser induced ions could be easily produced. The separation of electrodes fixed at around 3 mm distance to each other, thus the required voltage was around 200 V.

Data acquisition

Data collection for room temperature measurements was conducted using a SRS Gated Integrator and Boxcar Averager (SR 250, Stanford Research Systems, USA) instead of the oscilloscope as mentioned previously, because our oscilloscope was not available. The SR 250 consists of a gate generator, a fast gated integrator, and exponential averaging circuitry. The gate generator, which is triggered externally, provides an adjustable delay from a few nanoseconds to 100 ms before it generates a continuously adjustable gate with a width between 2 ns

and 15 μs. In the experiment, the $(2+1)$ REMPI signal is initially amplified by an Ortec 575 amplifier (575, Ortec, USA), which is capable of achieving amplification gains ranging from 10 to 500. After the amplification, the signal is sent to the gated integrator and boxcar averager, in which 30 samples are averaged. Then, the averaged output is sent to a computer interface module (SR 245). The digital output of the computer interface is connected to a computer via an RS-232 cable. REMPI spectra are recorded by scanning the dye laser wavelength from ≈ 201 to 204 nm, the REMPI signal for each wavelength step was averaged for 30 laser shots.

3.2.1 Results of characterization measurements at room temperature

Characterization measurements of the $(2+1)$ REMPI experiment at room temperature were carried out using the $Q_1(0,0)$ rovibrational transition. This transition is chosen because the $J''=1$ rotational state is the most populated state in H_2 at room temperature $(300\ \mathrm{K})$ since para- and ortho-H_2 spin multiplicity contributes to population distribution as discussed in section 2.4. Q-branch transitions are detected only since the O- and S-branch transitions are approximately 30 times are less probable compared to the Q-branch transitions due to the Holn-London factors as states in equation 2.40 and shown in table 2.7 [146, 147].

Gas pressure vs $(2+1)$ REMPI signal

As has already been discussed in section 2.7, the ion yield for the $(2+1)$ REMPI process is given by equation 2.23 where the ion yield is directly proportional to the pressure of the gas, which is proportional to N_0, the ground rovibronic state number density. In figure 3.4(a), the signal is measured over a range of gas pressures (other experimental parameters are constant, such as, laser intensity, voltage across electrodes). The signal becomes very insignificant around 5 Torr and it increases as the pressure goes up. The reason we conducted pressure measurements was because we wanted to identify an optimum pressure for the characteriza-

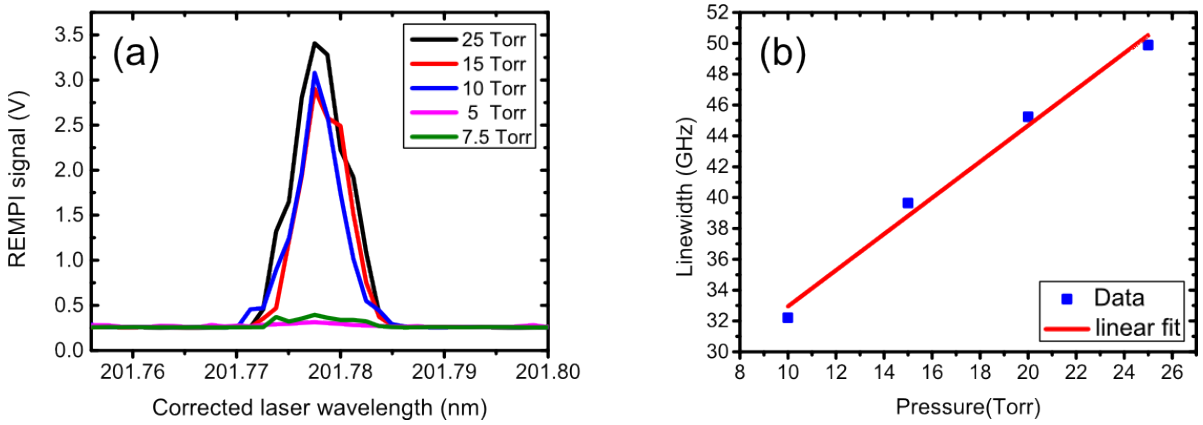

Figure 3.4: (a) shows the dependence of the signal with gas pressure at 300 K. (b) shows the FWHM of the signal versus gas pressure.

tion measurements. As a result, the optimum gas pressure was chosen to be around 15 torr. Pressures above 25 torr were not practical as the pressure increases the breakdown voltage increases and the resulting ion signal becomes very laser. This could cause saturation of our detection equipment.

Figure 3.4(b) shows the variation in the FWHM of the REMPI signal with pressure. The measurement confirms that the correlation between the linewidth and the gas pressure is linear. The measured linewidths are generated by fitting the raw data to a Gaussian function in Origin Lab.

Amplification gain vs $(2+1)$ REMPI signal

In figure 3.5(a), the variation in the signal with the amplification gain from the Ortec 575 amplifier is displayed. The purpose of this measurement is to characterize the gain setting on the amplifier so that we could operate the $(2+1)$ REMPI experiment at optimum voltage-amplification as well as ensure that the amplifier operates linearly. The integrated area under measured signal with respect to gain is shown in the figure 3.5(b). A linear response was

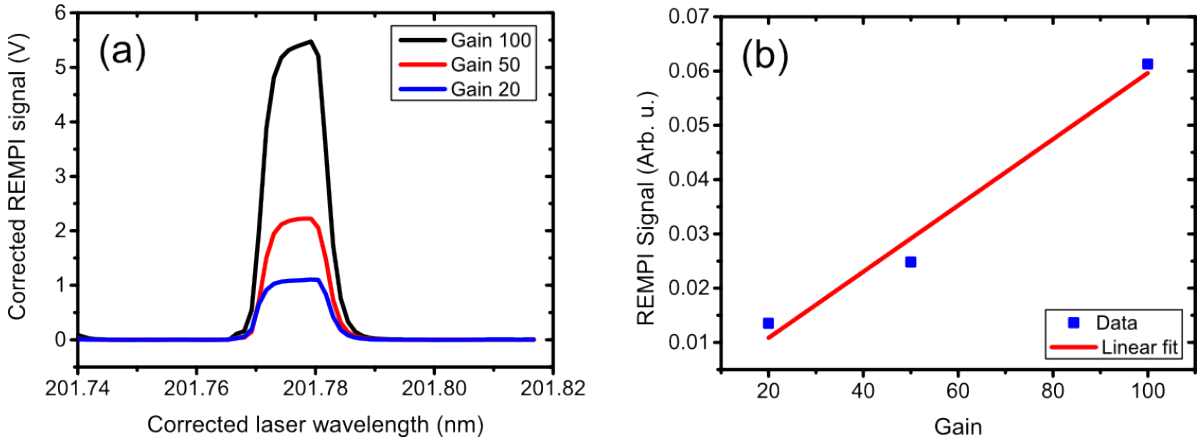

Figure 3.5: (a) shows the variation in the signal with amplification gain at 300 K. (b) shows the integrated peak area of the signal with respect to the gain.

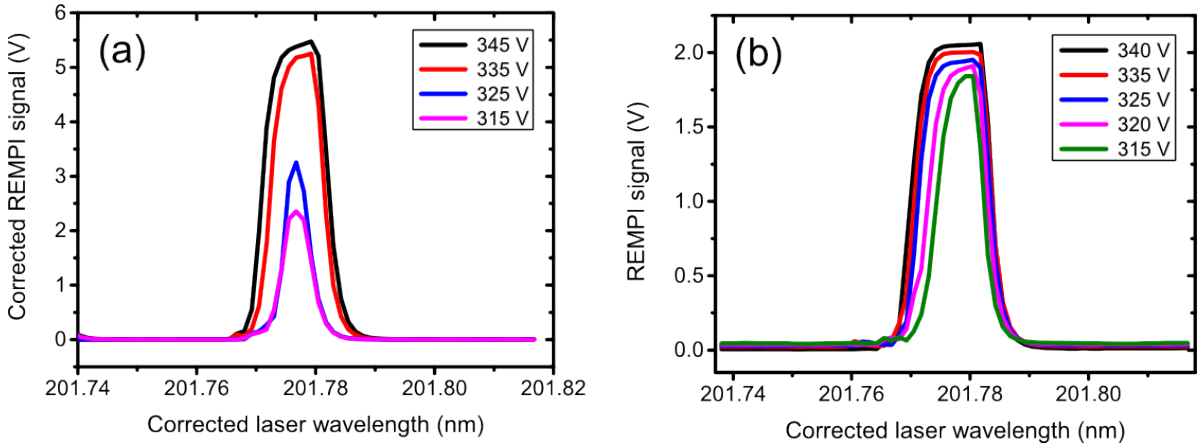

Figure 3.6: (a) shows the variation in signal with voltage across electrodes at 300 K, with a gain factor of 100. The signal level increases as the voltage across the electrodes rise and it saturates at around 345 V. (b) shows a close up to the saturation effect with various voltages.

obtained and a gain of 100 was chosen for our measurements.

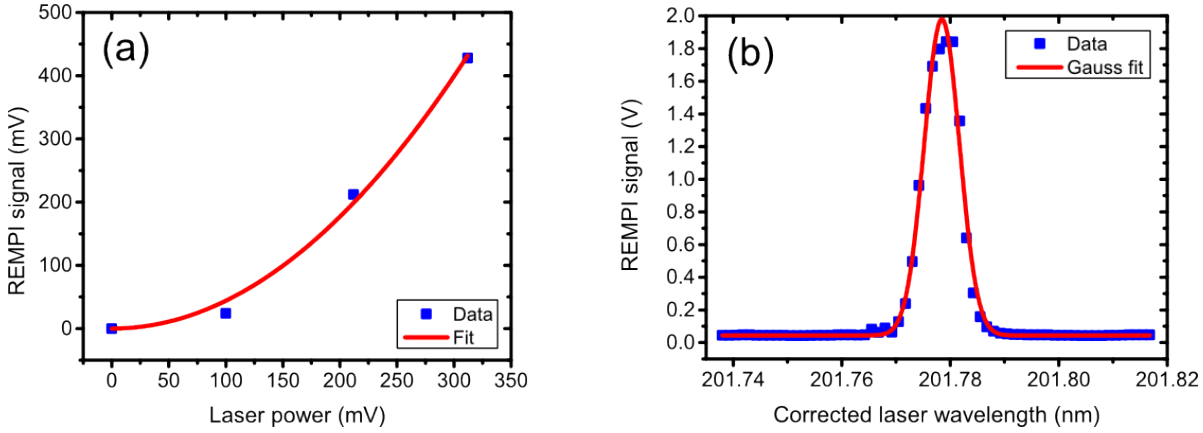

Figure 3.7: (a) shows the signal's dependence on laser power at 300 K. (b) shows the doppler broadening measurement at 300 K. H_2 $Q_1(0,0)$ transition line is scanned for this measurement and the measured linewidth at FWHM is 57.0 ± 1.5 GHz.

Voltage vs $(2+1)$ REMPI signal

In figure 3.6(a), the REMPI signal is recorded at various electrode voltages. The applied voltage across the electrodes and the signal are correlated such that as the voltage is increased, the signal value rises. Note, during the characterization experiment we had to carefully adjust the voltage. Since otherwise, the signal detection electronics (i.e. boxcar averager or oscilloscope) might be saturated and thus the full signal may be missed. This effect of detection electronics saturation can be seen in the figure 3.6(b). In order avoid the saturation, we conducted our measurements at round 300 V.

Laser power vs $(2+1)$ REMPI signal

The signal with respect to laser power is measured. For this measurement, the laser wavelength is fixed to the peak at $Q_1(0,0)$ transition. The laser power is measured by a photodiode (PD) in a configuration as shown in the figure 3.2. The UV laser output power was varied by turning

the half-wave plate in the FCU unit as shown in figure 3.1. Each data point is averaged on the scope for 20 laser shots. The measured data points were fitted to a power function in Origin lab, as shown in figure 3.7(a). As a result, it is found that the signal scales with a power of 2.0 ± 0.2 with respect to the laser power. These findings are in agreement with the equation 2.23 in which the REMPI signal is predicted to be proportional to the square of the laser power.

Doppler broadening

The linewidth measurement at room temperature was conducted at $Q_1(0,0)$ transition line, shown in figure 3.7(b). As explained in subsection 2.8.3, the Doppler profile is Gaussian shape. Thus, the measured data is fitted to a Gaussian function in Origin lab in order to determine the linewidth of the transition. The measured linewidth is found to be $\Delta\lambda = 0.0077 \pm 0.0002$ nm at FWHM which is equal to $\Delta f = 57.0 \pm 1.5$ GHz. The theoretical value for Doppler broadening at 300 K is calculated using the equation 2.50 and is found to be $\Delta\lambda = 0.0071$ nm which corresponds to $\Delta f = 52.0$ GHz. If this is subtracted from the measured linewidth, the remaining braodening must be due to the laser linewidth since the natural and pressure broadening effects are negligible. Consequently, the laser linewidth is determined to be 0.0006 ± 0.0002 nm, which is equal to 5.0 ± 1.5 GHz.

Power broadening effect measurement

The spectral width of an atomic/molecular transition absorption line generally increases with incident laser power, a phenomenon known as power broadening [148]. Power broadening of the REMPI signal is measured by varying laser power and scanning the laser wavelength over the $Q_1(0,0)$ transition line. As can be seen in figure 3.8, the measurement is carried out for four different laser powers which are $0.3,\ 0.6,\ 0.8,$ and 1 mJ/pulse respectively. It should be noted that these values are relative to the actual laser power since we only measure

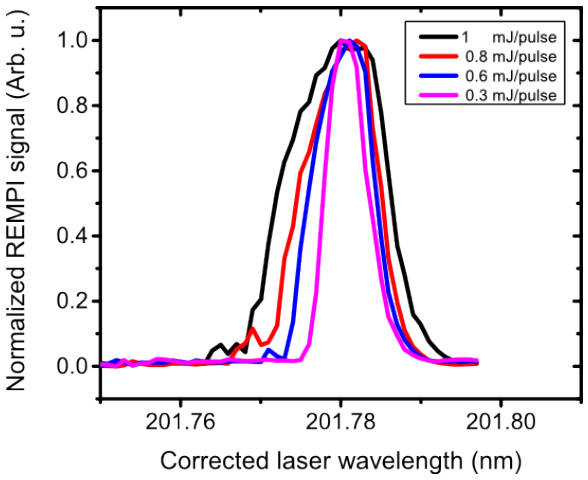

Figure 3.8: Power broadening of $Q_1(0,0)$ at 300 K. The FWHM of the REMPI signal was found to increase with laser power with values of $0.00558,\ 0.00821,\ 0.0101$ and 0.01342 nm recorded for laser pulse energies of $0.3,\ 0.6,\ 0.8$ and 1 mJ, respectively.

a small portion of the output beam on a photodiode, depicted in figure 3.2. The laser power is recorded simultaneously along with the REMPI signal as the laser is scanned. The raw data is normalized to the squared laser power because the REMPI signal is proportional to this. The signal is seen to broaden as the laser power is increased, shown in the figure 3.8. Note that the laser has a small shift in wavelength (due to the calibration) and it has to be accounted for when generating the spectra. The corrected laser wavelength is the value after this shift is accounted for and this is applied to the rest of the measurements in this thesis.

In figure 3.9, the experimental spectrum is compared to the simulation at room temperature. The measured and the simulated spectrum are in a good agreement. The comparison is established for the transitions, given as $Q_0(0,0),\ Q_1(0,0),\ Q_2(0,0),\ Q_3(0,0)$ and $Q_4(0,0)$ respectively. Although in the simulated spectrum, the $Q_4(0,0)$ line has a very small fraction of population, this could not be detected. The difference in line strengths are mainly due to the non-uniform laser intensity over the scanned wavelength range. Even though the REMPI sig-

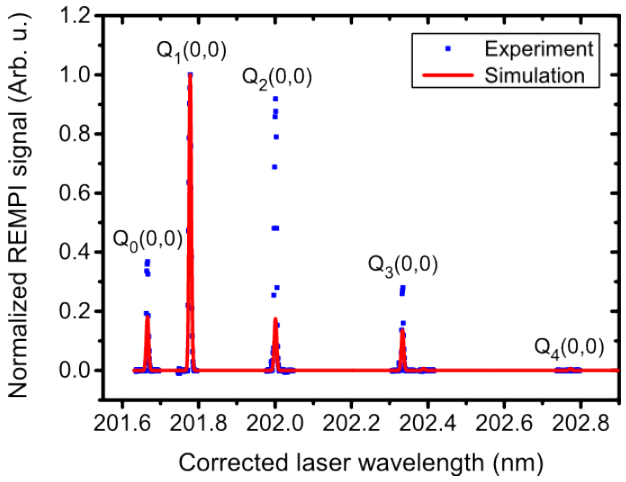

Figure 3.9: The measured H_2 $(2+1)$ REMPI spectrum vs simulation at 300 K. The measured and simulated spectrum show a good agreement (lines assigned according to reference [137]).

nal is normalized to the squared laser intensity, large fluctuations in laser intensity might have caused REMPI signal to be non-quadratic with respect to laser power. Thus, the difference in relative line intensities might have occurred. This difference will result in large uncertainty in the rotational temperatures.

Extraction of rotational temperature from the simulated spectrum at 300 K

The rotational temperature of the H_2 molecules can be extracted from the spectrum by using a Boltzmann plot. In order to produce the Boltzmann plot, we need to revise how we calculated the line intensities for the $(2+1)$ REMPI spectrum as discussed in subsection 2.8.2. In equation 2.40, the line intensities for Q-branch transitions are given and the relative rovibrational state populations are expressed in the equation 2.39.

Now, if we substitute the equation 2.39 into the equation 2.40, the Q-branch intensity is given by:

$$I_{\mathrm{Q}}(J', J'') = S_{\mathrm{Q}}(J', J'')g(J'')\exp\left(\frac{-(\mathrm{G}(v'') + \mathrm{F}(J''))}{k_{\mathrm{B}}T}\right).$$

From this expression we would like to determine the temperature. We rearrange to get:

$$\ln\left(\frac{I_{\mathrm{Q}}(J',J'')}{S_{\mathrm{Q}}(J',J'')g(J'')}\right) = \frac{-(\mathrm{G}(v'') + \mathrm{F}(J''))}{k_{\mathrm{B}}T}. \tag{3.1}$$

Now, if one plots the "ln" term on the left hand side versus the numerator term on the right hand side, which is essentially the rovibrational term values, the resulting plot gradient will be equal to $-\frac{1}{k_{\mathrm{B}}T}$ where k_{B} is 0.695 cm^{-1}/K and thus the temperature can be calculated. This is called Boltzmann plot method which used to determine the rotational temperature from a measured or simulated rovibrational spectrum. The temperature will be equal to the rotational as well as transnational and vibrational temperature because the gas is in equilibrium. In equation 3.1, $I_{\mathrm{Q}}(J',J'')$ can be experimantally measured and thus the rotational temperature of the gas can be determined. We verify the Boltzmann plot method on simulated data, using the term values in table 3.1. We can now employ the same method to determine the rotational temperature from the measured room temperature spectrum.

Extraction of rotational temperature from the experimental spectrum at 300 K

The rotational temperature of H_2 molecules at room temperature is determined from the measured spectrum shown in figure 3.9.

Transition line	Line intensity $(I(J))$	Rovibrational Term values (cm^{-1})
$\mathrm{Q}_0(0,0)$	0.0018	2.1703×10^3
$\mathrm{Q}_1(0,0)$	0.0098	2.2887×10^3
$\mathrm{Q}_2(0,0)$	0.0017	2.5245×10^3
$\mathrm{Q}_3(0,0)$	0.0013	2.8754×10^3
$\mathrm{Q}_4(0,0)$	6.2190×10^{-5}	3.3379×10^3
$\mathrm{Q}_5(0,0)$	1.4792×10^{-5}	3.9075×10^3

Table 3.1: Parameters extracted from the simulation of the REMPI spectrum.

A Boltzmann plot was generated by using the line intensities of the measured lines. They are determined from the area under each peak by fitting each line to a Gaussian function in Origin lab are listed in table 3.2. The fitted experimental data is shown the figure 3.10(a). The rotational temperature is then determined to be 326 ± 54 K. Although this result is in agreement with the room temperature within the error range, the uncertainty is around 17% and relatively large.

Transition line	Line intensity$(I(J))$ (Peak area)	Rovibrational Termvalues(cm^{-1})
$\text{Q}_0(0,0)$	1.02114×10^{-4}	2.1703×10^3
$\text{Q}_1(0,0)$	3.57141×10^{-4}	2.2887×10^3
$\text{Q}_2(0,0)$	2.99468×10^{-4}	2.5245×10^3
$\text{Q}_3(0,0)$	7.05623×10^{-5}	2.8754×10^3

Table 3.2: Parameters extracted from the experimental spectrum.

Simulated room temperature spectra in the v'' = 0 and v' = 1 vibrational states

The motivation for this section is to compare the population of ground and excited vibrational states at room temperature. This is shown in the figure 3.10(b). The simulation illustrates the Q-branch rovibrational transitions in H_2. When the REMPI signal strength of the both vibtarional states are compared, the former vibrational state's signal strength is at around 0.010 while the latter one is at round 2.00×10^{-11}. That means practically all the molecules are in the v'' = 0 vibrational state at 300 K. Thus, a mechanism is needed to transfer population from v'' = 0 to v' = 1 vibrational state. To achieve that, we employ non-equilibrium discharge to populate the excited vibrational state. Thus, we can detect these molecules by REMPI as discussed in chapter 1.

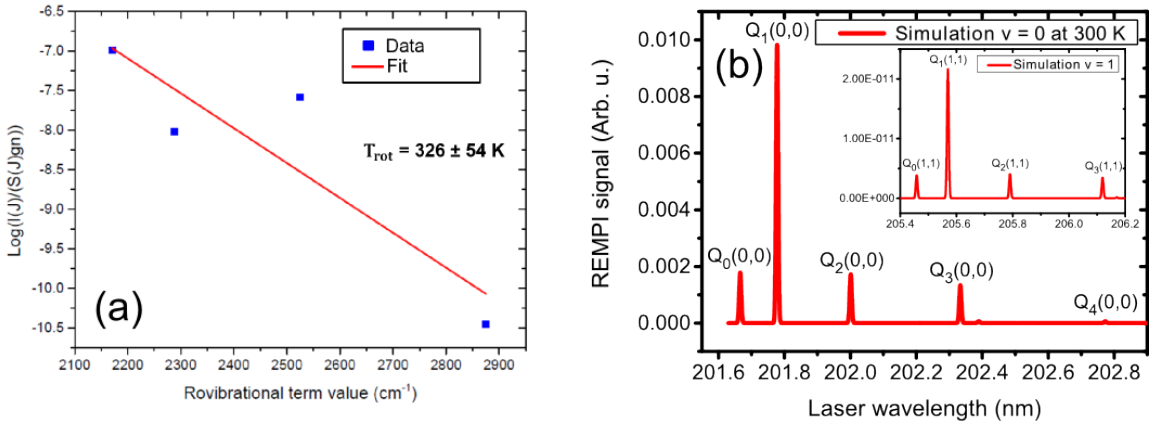

Figure 3.10: (a) shows the Boltzmann plot of the experimental spectrum at 300 K. $Q_0(0,0)$, $Q_1(0,0)$, $Q_2(0,0)$, $Q_3(0,0)$ lines are used. The rotational temperature is found to be 326 ± 54 K. (b) shows the simulated room temperature H_2 $(2+1)$ REMPI spectra in the $v'' = 0$ and $v' = 1$ (inset) vibrational states. As can be seen, at room temperature the signal strength of rovibrational transitions in the $v'' = 0$ state is much larger than in the $v' = 1$.

3.2.2 Characterization of the $(2+1)$ REMPI experiment in non-equilibrium discharge

The experimental setup for the REMPI experiment has been discussed in the section 3.1. To characterize the non-equilibrium discharge, the signal's dependence on several parameters, such as current and laser power, was first measured. The rotationally resolved REMPI spectrum in the $v'' = 0$ and $v' = 1$ states has been measured from which the vibrational, rotational and translational temperatures of H_2 in different regions of the non-equilibrium discharge can be measured. This has been measured for the fist time here at UCL.

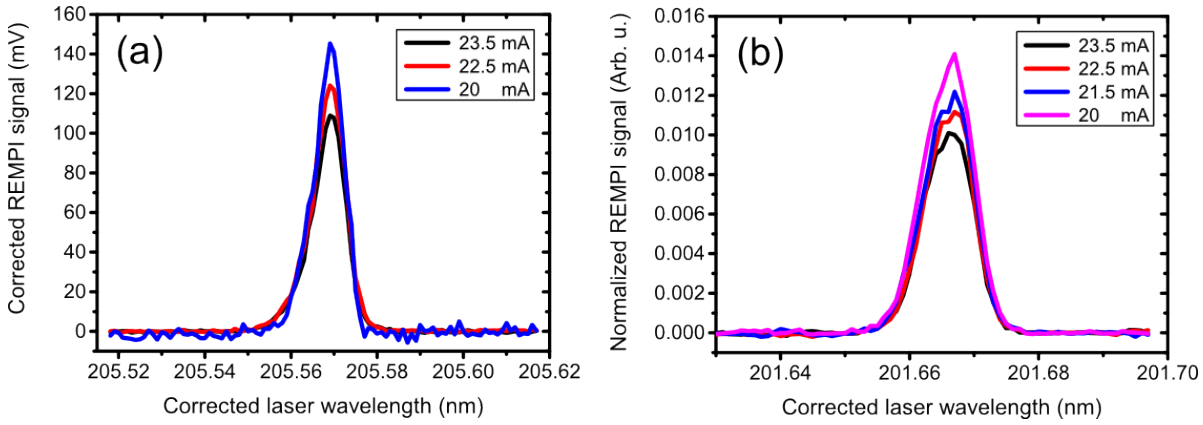

Figure 3.11: (a) shows the signal variation with current in the $v' = 1$ and $J' = 1$ rovibrational state. (b) shows the normalized signal variation with current in the $v'' = 0$ and $J'' = 0$ rovibrational state.

Current vs $(2+1)$ REMPI signal

This measurement was conducted for the H_2 $Q_1(1,1)$ line, which is the highest populated rovibrational state. In figure 3.11(a), the signal was measured with respect to various currents across the discharge. The signal increases as the current decreases, but the discharge is less stable at lower current. This can be seen in the figure as well, the base line of the signal at 20 mA has more noise compared to the other two measurements. Thus, we have done the characterization measurements in higher current which is around 23.5 mA. The gas pressure in the glass cell was kept at a constant flow of 16 Torr and the high voltage was 500 V. These values were used for the rest of measurements.

A similar measurement was carried out in the $v'' = 0$ vibrational state. This time $Q_0(0,0)$ line was measured. In addition, the signal was normalized to the squared laser intensity, as shown the figure 3.11(b). As can be seen in the figure, the normalized signal increases as the current decreases.

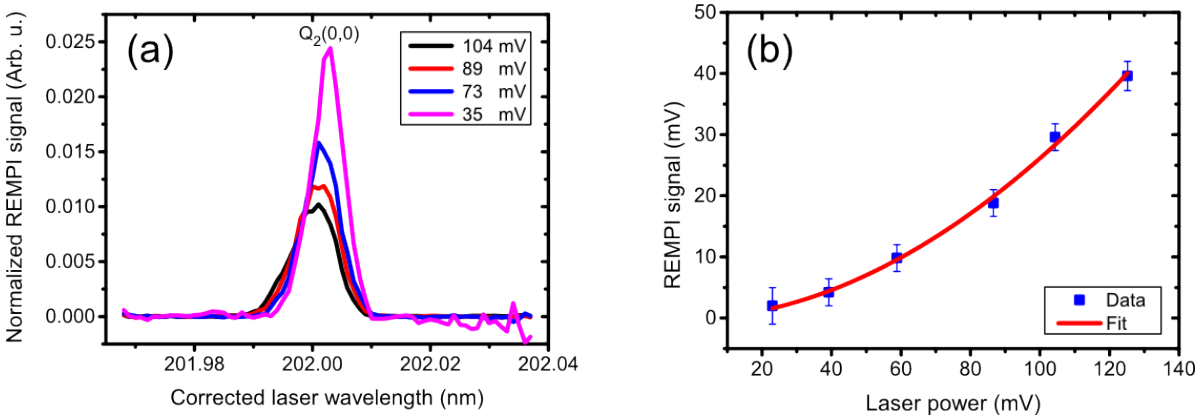

Figure 3.12: (a) The normalized signal variation with laser power is shown. The transition linewidth increases as the laser power increases. (b) The signal's dependence on the laser power is displayed in the non-equilibrium discharge.

Laser power vs $(2+1)$ REMPI signal

The normalized signal variation with laser power in non-equilibrium discharge was measured, as shown in figure 3.12(a). The measurement was carried out in the $v'' = 0$ and $J'' = 2$ rovibrational state which is denoted as $Q_2(0,0)$. The measured values range from 38 to 104 mV. Here, these values are relative to the laser power. The linewidth of the transition decreases as the laser power falls. The signal was normalized to the squared laser intensity.

The figure 3.12(b) shows the signal's dependence on the laser power in the non-equilibrium discharge. The measurement was conducted in the $v' = 1$ and $J' = 1$ rovibrational state denoted as $Q_1(1,1)$. Each data point was averaged for 20 laser shots. The resulting plot was fitted to a power function in Origin lab and the power factor was found to be 1.90 ± 0.09. This result agrees well with the theoretical square power dependence. Consequently, the measured spectral lines of H_2 molecules were normalized to the squared laser power for each measurement.

3.2.3 Full spectrum of H_2 $(2+1)$ REMPI in the $v'' = 0$ and $v' = 1$

The full spectrum of H_2 in the $v' = 1$ vibrational state in the non-equilibrium discharge is displayed in figure 3.13(a). The measurement is carried out to establish the rovibrational lines of H_2 Q-branch transitions. The first six populated rovibrational lines of the H_2 molecules in the first vibrationally excited state are successfully measured. In the experiment, each line is scanned twice to verify that each measurement repeats itself. The populated rovibrational lines are denoted as $Q_0(1,1)$, $Q_1(1,1)$, $Q_2(1,1)$, $Q_3(1,1)$, $Q_4(1,1)$, and $Q_5(1,1)$ respectively. Although the $Q_6(1,1)$ is measured, population is not detected in this level. Thus, it is concluded that the higher J levels would not be populated. Note that the signal is normalized to the squared laser power.

The full spectrum of H_2 in the $v'' = 0$ vibrational state in non-equilibrium discharge is shown in figure 3.13(b). The measurement was conducted to determine the $v'' = 0$ rovibrational populations in order to compare the population distribution with the $v' = 1$ vibrational state. The first 7 rovibrational lines in the $v'' = 0$ are measured, which are $Q_0(0,0)$, $Q_1(0,0)$, $Q_2(0,0)$, $Q_3(0,0)$, $Q_4(0,0)$, $Q_5(0,0)$ and $Q_6(0,0)$ respectively. The rovibrational levels up to $Q_5(0,0)$ are populated but no population is detected in the $Q_6(0,0)$ level. This was the case in the $v' = 1$ vibrational state and thus the number of the populated levels are consistent with each other. The $v'' = 0$ and $v' = 1$ vibrational states' total populations are compared, and with a good approximation 10% of the H_2 molecules in the $v'' = 0$ vibrational state are excited to the $v' = 1$ in the non-equilibrium discharge.

3.2.4 Rotational temperature of H_2 in the $v'' = 0$ and $v' = 1$

The rotational temperature in the $v'' = 0$ and $v' = 1$ vibrational states in the non-equilibrium discharge is calculated by employing the experimental spectra. The Boltzmann plot method is used as explained in section 3.2.1. Figure 3.14 shows the Boltzmann plot for determining the

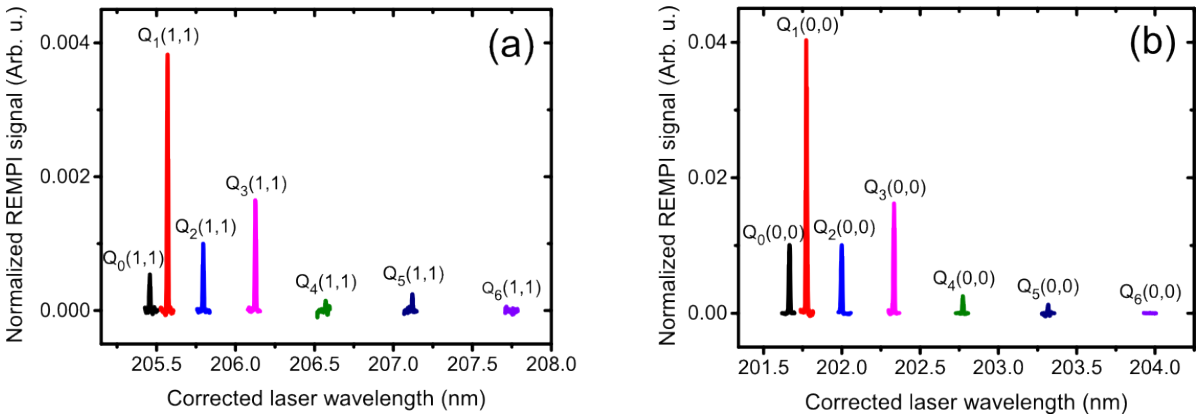

Figure 3.13: (a) shows the full spectrum of H_2 in the $v' = 1$ in the non-equilibrium discharge. (b) shows the spectrum in the $v'' = 0$.

rotational temperature of the H_2 in the $v'' = 0$ vibrational state. The line intensities from the spectrum in the figure 3.13(b) are used. The measured line intensities along with the rovibrational term values are listed in the table 3.3.

The figure 3.14(a) shows the resulting Boltzmann plot and the rotational temperature in the $v'' = 0$ in non-equilibrium discharge is found to be 488 ± 15 K. Figure 3.14(b) illustrates the resulting Boltzmann plot in which we used the experimental line intensities extracted from the spectrum in the $v' = 1$, as shown in figure 3.13. These parameters are listed in the table 3.3. The rotational temperature of the H_2 molecule in the $v' = 1$ is determined to be 529 ± 16 K.

Transition line	Line intensity $(I(J))$	Rovibrational Term values (cm^{-1})
$\text{Q}_0(0,0)$	0.01	2.1703×10^3
$\text{Q}_1(0,0)$	0.04	2.2887×10^3
$\text{Q}_2(0,0)$	0.01	2.5245×10^3
$\text{Q}_3(0,0)$	0.016	2.8754×10^3
$\text{Q}_4(0,0)$	0.0026	3.3379×10^3
$\text{Q}_5(0,0)$	0.0014	3.9075×10^3
$\text{Q}_0(1,1)$	5.5226×10^{-4}	6.3288×10^3
$\text{Q}_1(1,1)$	0.00383	6.4412×10^3
$\text{Q}_2(1,1)$	0.00101	6.6647×10^3
$\text{Q}_3(1,1)$	0.00166	6.9972×10^3
$\text{Q}_4(1,1)$	1.6170×10^{-4}	7.4352×10^3
$\text{Q}_5(1,1)$	2.5583×10^{-4}	7.9742×10^3

Table 3.3: The parameters extracted from the experimental spectrum in the $v'' = 0$ and $v' = 1$ in the non-equilibrium discharge.

3.2.5 Vibrational temperature of H_2 in the non-equilibrium discharge

We initially established how to deduce the vibrational temperature from the $(2 + 1)$ REMPI spectrum and then applied it to the measured H_2 spectra in the $v'' = 0$ and $v' = 1$ vibrational states. Since we measured two vibrational states and their rovibrational level populations, we can determine the vibrational temperature from the relative intensity of these states. Such expression will be dependent on the Franck-Condon and the Boltzmann factor as given:

$$\frac{I_{v'}}{I_{v''}} = \frac{A_{v'}}{A_{v''}} \text{e}^{-\frac{(G(v')-G(v''))}{k_\text{B} T_\text{vib}}}, \tag{3.2}$$

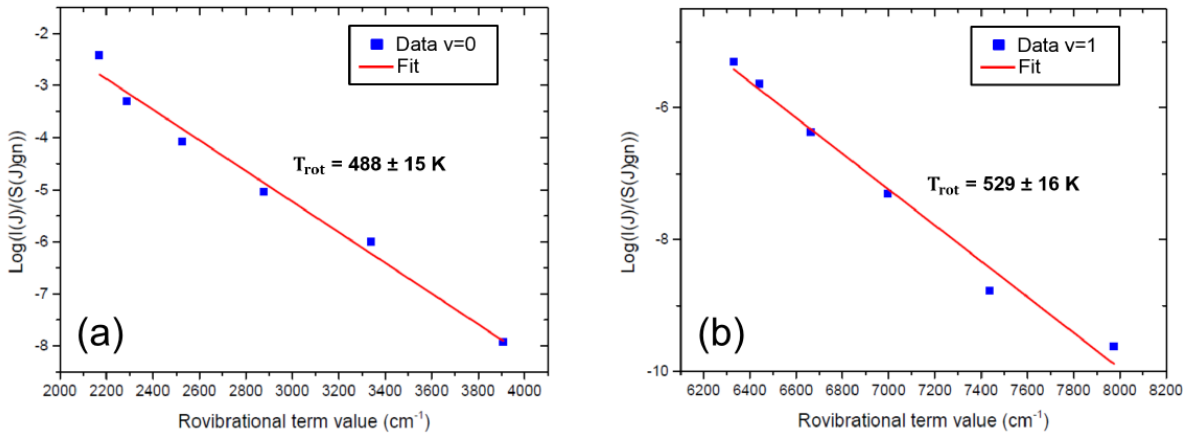

Figure 3.14: (a) shows the Boltzmann plot using the measured spectrum data in the $v'' = 0$ in the non-equilibrium discharge. The rotational temperature is calculated to be 488 ± 15 K. (b) shows the Boltzmann plot using the measured spectrum data in the $v' = 1$ in the non-equilibrium discharge. The rotational temperature is calculated to be 529 ± 16 K.

where $I_{v'}$ and $I_{v''}$ are the total rovibrational line intensities for $v' = 1$ and $v'' = 0$ vibrational states respectively. $A_{v'}$ and $A_{v''}$ are the total Franck-Condon factors for the $v' = 1$ and $v'' = 0$ respectively. $G(v')$ and $G(v'')$ are the corresponding vibrational term values for each state. Lastly, k_B and T_{vib} are expressed as Boltzmann constant and vibrational temperature. To calculate the T_{vib}, we need to rearrange the equation 3.2 as:

$$T_{vib} = -\frac{(G(v') - G(v''))}{k_B \times \ln\left(\frac{\left(\frac{I_{v'}}{I_{v''}}\right)}{\left(\frac{A_{v'}}{A_{v''}}\right)}\right)}. \tag{3.3}$$

Transition line	Line intensity $(I(J))$ (Raw data)	Line intensity $(I(J))$ (Gauss fit)
$Q_0(0,0)$	0.01026	0.01042
$Q_1(0,0)$	0.04072	0.03641
$Q_2(0,0)$	0.01019	0.01012
$Q_3(0,0)$	0.01639	0.01615
$Q_4(0,0)$	0.00267	0.00247
$Q_5(0,0)$	0.00157	0.00123
$Q_0(1,1)$	5.96267×10^{-4}	5.50136×10^{-4}
$Q_1(1,1)$	0.0039	0.00383
$Q_2(1,1)$	0.00103	9.70711×10^{-4}
$Q_3(1,1)$	0.00167	0.0165
$Q_4(1,1)$	2.10166×10^{-4}	1.49481×10^{-4}
$Q_5(1,1)$	2.7255×10^{-4}	2.48576×10^{-4}

Table 3.4: Parameters extracted from the experimental spectrum in the $v'' = 0$ and $v' = 1$ in the non-equilibrium discharge for calculating vibrational temperature.

Now we can calculate the vibrational temperature of the H_2 molecule in the non-equilibrium discharge. To achieve that, the measured total line intensities for $v'' = 0$ and $v' = 1$ are used. The Fanck-Condon factors for H_2 $E, F^1\Sigma_g^+ - X^1\Sigma_g^+$ electronic transitions are used. The total Franck-Condon factor for the $v'' = 0$ and $v' = 1$ vibrational state are $A_{v''} = 4.6750 \times 10^6$ and $A_{v'} = 8.2129 \times 10^5$ respectively [136]. Therefore, if we measure the relative line intensities for the $v'' = 0$ and $v' = 1$, the vibrational temperature can be calculated. The experimental data for the raw data total line intensities in the $v'' = 0$ is $I_{v''} = 0.0818$ and in the $v' = 1$ is $I_{v'} = 0.0077$ as given in the table 3.4. Consequently, the vibrational temperature, T_{vib}, of H_2 in the non-equilibrium discharge is calculated to be 3273 ± 380 K, using the equation 3.3.

The error in the vibrational temperature is determined by first calculating the error in the total line intensity of the rovibrational lines for $v'' = 0$ and $v' = 1$. Secondly these errors are propagated by using the error propagation relation. To do this, all the measured rovibrational lines in the both vibrational states are fitted to a Gaussian function in the Origin lab and the total intensities are determined in that case. Then, the difference between the total raw data and Gauss fit intensity is taken as the error in the total intensity for the each vibrational state.

3.2.6 Translational temperature of H_2 in the non-equilibrium discharge

The translational temperature of H_2 molecule in the $v'' = 0$ and $v' = 1$ is determined by using the measured Doppler profiles. The parameters are extracted from the measured spectrum for each state as given in the figure 3.13. First, we need to reconsider how the temperature is related to the Doppler broadening. As discussed in subsection 2.8.2, the Doppler broadening at FWHM for the $(2 + 1)$ REMPI process is expressed in equation 2.50. We can rearrange the equation for T, which will be the translational temperature and it is given as:

$$T_{\text{trans}} = \frac{\text{c}^2\text{m}(\Delta\lambda)^2}{16\lambda^2 8 k_{\text{B}} \ln(2)} \tag{3.4}$$

where $\Delta\lambda$ is the Doppler linewidth at FWHM. c, m, λ and k_{B} are the speed of light, mass of the H_2 molecule, laser wavelength and Boltzmann constant respectively.

In order to calculate the translational temperature from the experimental spectrum in the $v'' = 0$ and $v' = 1$ in the non-equilibrium discharge, the FWHM of raw and Gauss fitted data is used as listed in the table 3.5. The error in FWHM is determined by taking the difference between the FWHM of the raw and Gauss fit data for each rovibrational transition. The translational temperature is calculated by employing the equation 3.4. To do this, we require to use the Doppler linewidth at FWHM. However, as have been discussed earlier in the section 2.8.3, the measured linewith is convolution of the Doppler and laser linewidths.

Transition line	Laser wavelength (nm)	FWHM(nm) Raw data	FWHM(nm) Gauss fit	Translational Temperature(K)
$Q_0(0,0)$	201.67	0.00962	0.00907	486 ± 59
$Q_1(0,0)$	201.78	0.00831	0.00924	335 ± 86
$Q_2(0,0)$	202.00	0.00923	0.00916	442 ± 7
$Q_3(0,0)$	202.33	0.00900	0.00856	421 ± 44
$Q_4(0,0)$	202.77	0.00793	0.00726	316 ± 58
$Q_0(1,1)$	205.46	0.00849	0.00761	361 ± 80
$Q_1(1,1)$	205.57	0.00784	0.00763	299 ± 18
$Q_2(1,1)$	205.79	0.00734	0.0073	259 ± 3
$Q_3(1,1)$	206.12	0.00795	0.00784	315 ± 9
$Q_4(1,1)$	206.55	0.00834	0.0065	339 ± 159
$Q_5(1,1)$	207.09	0.00677	0.00604	219 ± 52

Table 3.5: Parameters extracted from the experimental spectrum in the v'' = 0 and v' = 1 in the non-equilibrium discharge for calculating the translational temperature.

Therefore, we can determine the measured Doppler linewidth at FWHM using the expression below:

$$\Delta\lambda_D = \Delta\lambda_R - \Delta\lambda_L \tag{3.5}$$

where $\Delta\lambda_D$ is the Doppler broadening at FWHM. $\Delta\lambda_R$ and $\Delta\lambda_L$ are the raw data and laser linewidth at FWHM respectively. As discussed in section 3.2.1, we already measured $\Delta\lambda_L$ and its value is 0.0006 ± 0.0002 nm. As a result, we have calculated the Doppler linewidth and then translational temperature of H_2 molecule in the v'' = 0 and v' = 1 as displayed in the table 3.5.

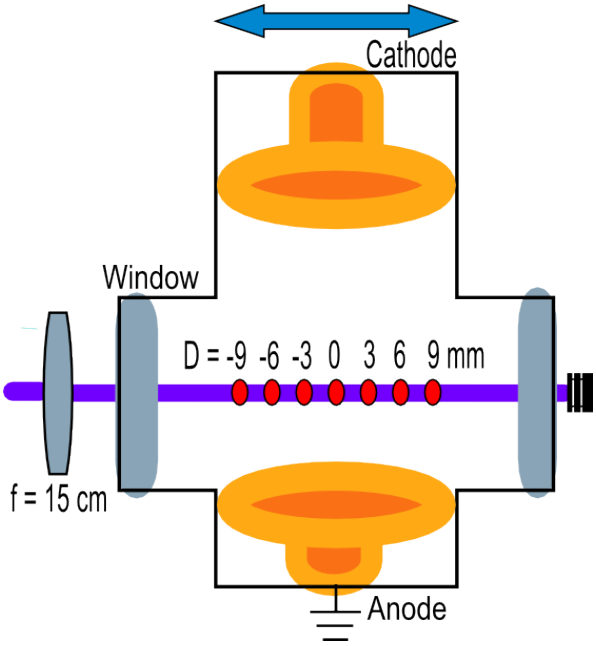

Figure 3.15: A schematic representation of the discharge cell showing the points at which the radial temperature measurements were made.

3.3 Radial temperature measurements of H_2 in the non-equilibrium discharge

The radial temperature of the H_2 molecule in the non-equilibrium discharge were investigated by the analysis $(2+1)$ REMPI spectra the determine the rotational populations in the $v'' = 0$ and $v' = 1$ vibrational levels of the $X^1\Sigma_g^+$ ground state and their transition linewidths. REMPI measurements were taken at seven different positions and the separation between each distance was chosen to be 3 mm. The diameter of the electrodes are 20 mm as described in section 3.1.3. Thus, our measurements covers 18 mm of the non-equilibrium discharge. Figure 3.15 shows the discharge cell and the different spatial positions denoted as $D = -9,\ -6,\ -3,\ 0,\ 3,\ 6$ and 9 mm respectively. Each measurement was taken in the different position by moving the glass

cell with respect to focus of the UV beam and this is indicated by two-way arrow in the figure.

The experimental setup and data acquisition process have been discussed in section 3.1. The same gas mixture of 5% H_2 in Argon was used. The gas mixture pressure was at constant flow of 16 torr throughout the measurements. The UV beam output was around ≈ 1 mJ/pulse. The current and voltage across the electrodes were 23.5 mA and 500 V respectively.

3.3.1 H_2 $(2+1)$ REMPI Spectra for radial temperature measurements

The first measured spectrum at D = 0 mm distance is shown in the figure 3.16(a) and spectrum at D = 3 mm is shown in the figure 3.16(b). The spectra of H_2 in the v'' = 0 and v' = 1 vibrational states are combined and displayed in the figure. The measured rovibrational transitions in the v'' = 0 are denoted as $Q_0(0,0)$, $Q_1(0,0)$, $Q_2(0,0)$, $Q_3(0,0)$, $Q_4(0,0)$, $Q_5(0,0)$, $Q_6(0,0)$ and $Q_7(0,0)$ respectively while the transitions in the v' = 1 are denoted as $Q_0(1,1)$, $Q_1(1,1)$, $Q_2(1,1)$, $Q_3(1,1)$, $Q_4(1,1)$, $Q_5(1,1)$ and $Q_6(1,1)$ respectively. Next measurements are carried out at D = 6 and 9 mm and the measured spectra are illustrated in figure 3.17. In another set of measurements, the radial distances were at D = -3 and -6 mm and the measured spectra are given in figure 3.18. The last measurement of the radial distance was taken at D = -9 mm in the non-equilibrium discharge and the measured spectrum is illustrated in figure 3.19.

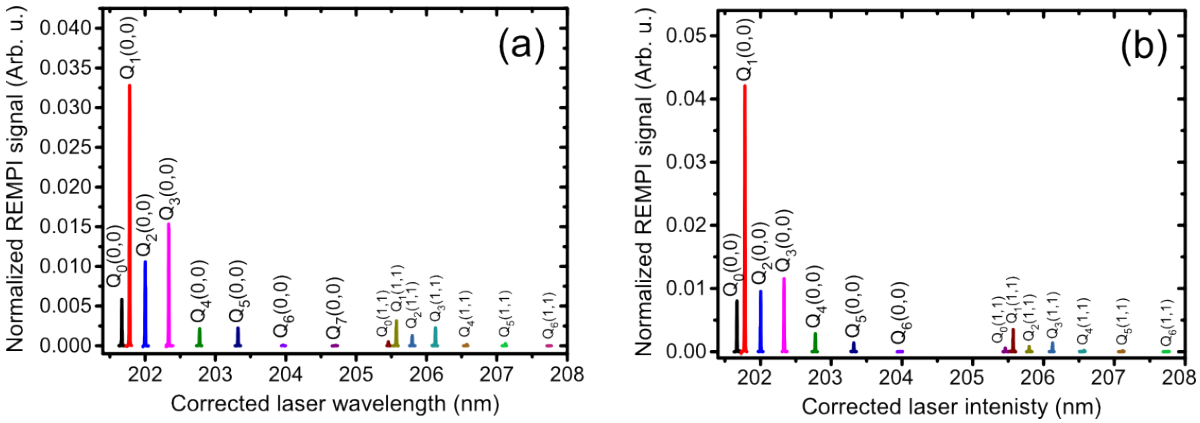

Figure 3.16: (a) shows the measured spectrum at D = 0 mm. (b) shows the spectrum at D = 3 mm.

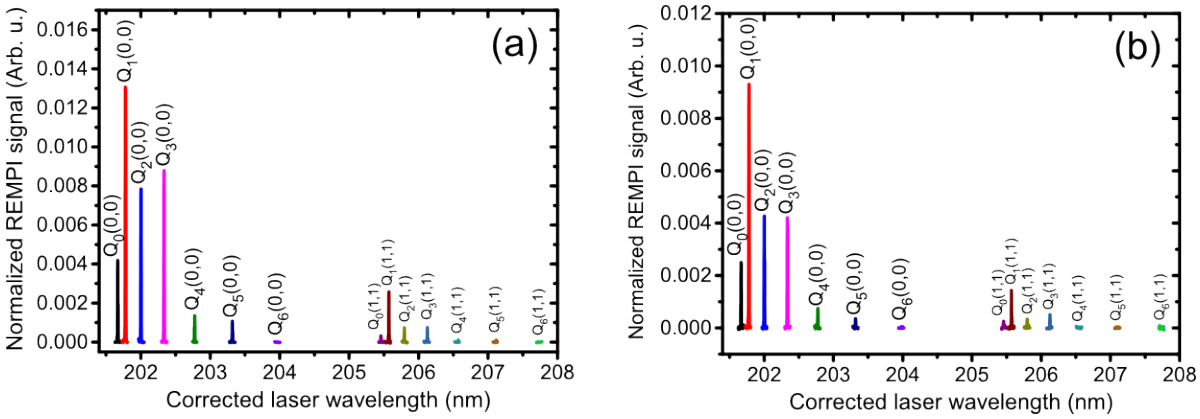

Figure 3.17: (a) shows the measured spectrum at D = 6 mm. (b) shows the spectrum at D = 9 mm.

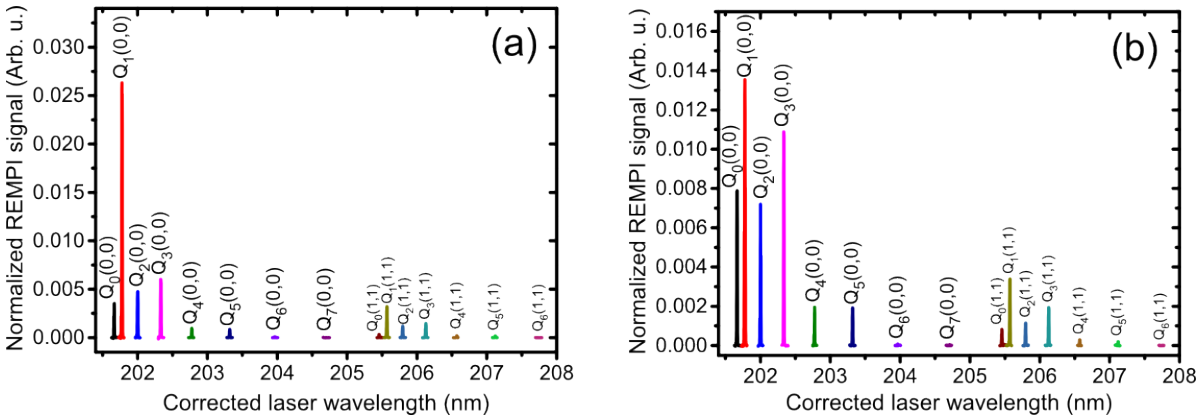

Figure 3.18: (a) shows the measured spectrum at $D = -3$ mm. (b) shows the spectrum at $D = -6$ mm.

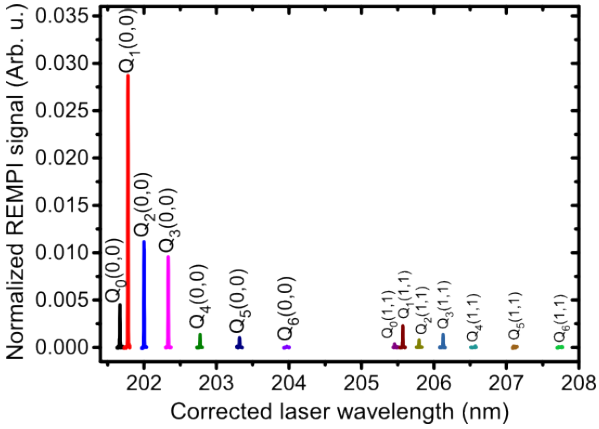

Figure 3.19: The measured spectrum at $D = -9$ mm is shown.

3.3.2 Radial rotational temperatures of the H_2 molecule in the non-equilibrium discharge

The radial rotational temperature of H_2 in the $v'' = 0$ and $v' = 1$ for the different radial distances will be determined. To achieve that, for each radial distance, the $(2 + 1)$ REMPI spectrum was

analysed and the required parameters were determined to produce a Boltzmann plot.

Firstly, the rotational temperature of H_2 at $D = 0$ mm radial distance is determined. The data from the spectrum shown in the figure 3.16 is used to calculate the parameters for the Boltzmann plot in the $v'' = 0$ and $v' = 1$. Table A.1 and A.2 illustrate the required parameters for the Boltzmann plot both in the $v'' = 0$ and $v' = 1$ vibrational states. The area under curve of the measured rovibrational lines is taken as the line intensity.

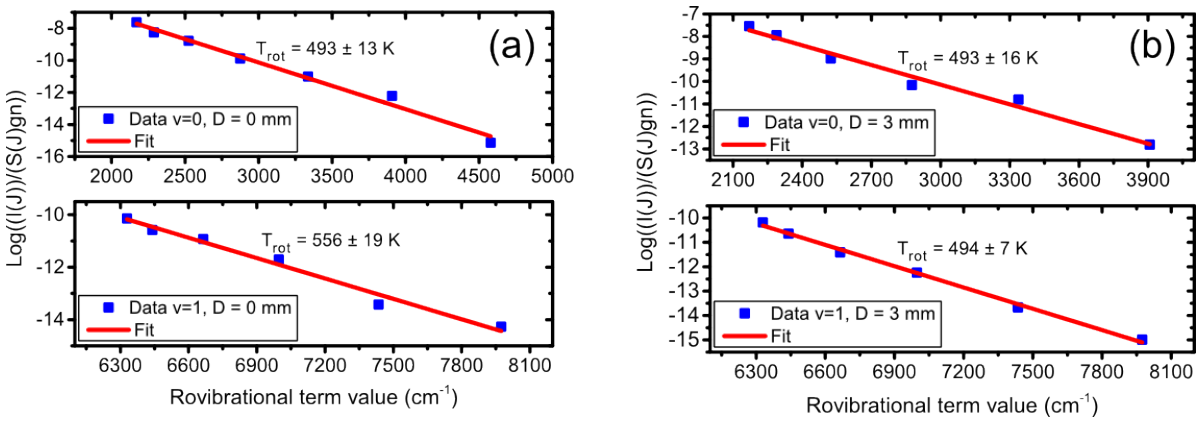

Figure 3.20: (a) shows the Boltzmann plots using the measured spectrum data at $D = 0$ mm in the $v'' = 0$ and $v' = 1$ in the non-equilibrium discharge. The rotational temperatures are found to be 493 ± 13 and 556 ± 19 K respectively. (b) show the Boltzmann plots at $D = 3$ mm and the rotational temperatures are found to be 493 ± 16 and 494 ± 7 K for $v'' = 0$ and $v' = 1$ respectively.

The Boltzmann plot is produced by plotting the rovibrational term values versus the Log term in the table. Figure 3.20(a) shows the resulting Boltzmann plots for the $v'' = 0$ and $v' = 1$ vibrational states. The slopes are $-0.00292 \pm 1.5279 \times 10^{-4}$ and $-0.00259 \pm 1.7358 \times 10^{-4}$ for $v'' = 0$ and $v' = 1$ respectively. The rotational temperature is then calculated to be 493 ± 13 K for $v'' = 0$ and 556 ± 19K for $v' = 1$. The Boltzmann plots for $v'' = 0$ and $v' = 1$ are produced to calculate the rotational temperature of the H_2 molecule as shown in figure 3.20(b). The resulting slope is $-0.00292 \pm 1.9815 \times 10^{-4}$ and $-0.00291 \pm 8.9009 \times 10^{-5}$ for $v'' = 0$ and $v' = 1$

respectively. Therefore, the rotational temperature at D = 3 mm is calculated to be 493 ± 16 K for $v'' = 0$ and 494 ± 7K for $v' = 1$.

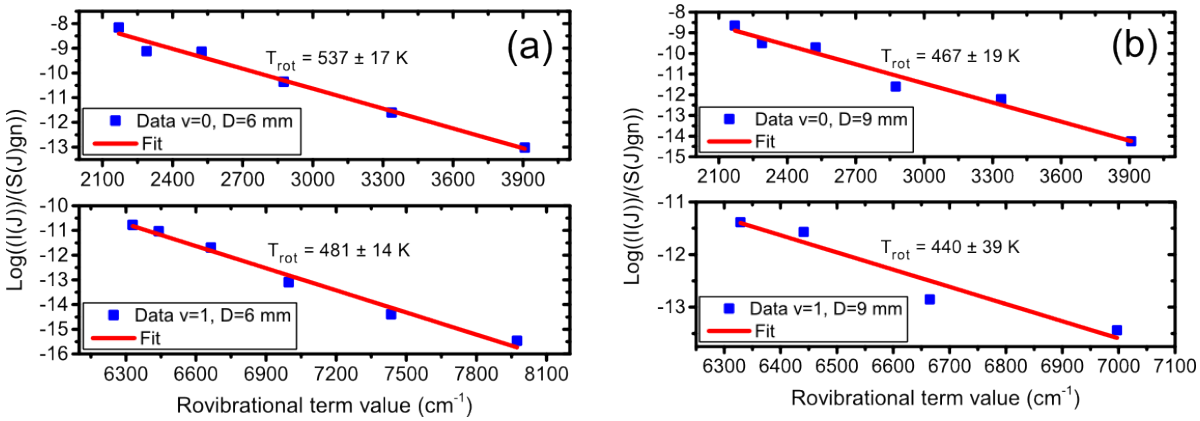

Figure 3.21: (a) shows the Boltzmann plots using the measured spectrum data at D = 6 mm in the $v'' = 0$ and $v' = 1$ in the non-equilibrium discharge. The rotational temperatures are found to be 537 ± 17 and 481 ± 14 K respectively. (b) shows the Boltzmann plots at D = 9 mm and the rotational temperatures are 467 ± 19 and 440 ± 39 K for $v'' = 0$ and $v' = 1$ respectively.

The Boltzmann plots for the $v'' = 0$ and $v' = 1$ at D = 6 mm are produced to calculate the rotational temperature of the H_2 molecule as shown in figure 3.21(a). The resulting slope is $-0.00268 \pm 1.7307 \times 10^{-4}$ and $-0.00299 \pm 1.7884 \times 10^{-4}$ for $v'' = 0$ and $v' = 1$ respectively. Therefore, the rotational temperature at D = 6 mm is calculated to be 537 ± 17 K for $v'' = 0$ and 481 ± 14K for $v' = 1$. The Boltzmann plots for the $v'' = 0$ and $v' = 1$ at D = 9 mm are produced to calculate the rotational temperature of the H_2 molecule as shown in figure 3.21(b). The resulting slope is $-0.00308 \pm 2.5212 \times 10^{-4}$ and $-0.00327 \pm 5.9821 \times 10^{-4}$ for $v'' = 0$ and $v' = 1$ respectively. Therefore, the rotational temperature at D = 9 mm is calculated to be 467 ± 19 K for $v'' = 0$ and 440 ± 39K for $v' = 1$.

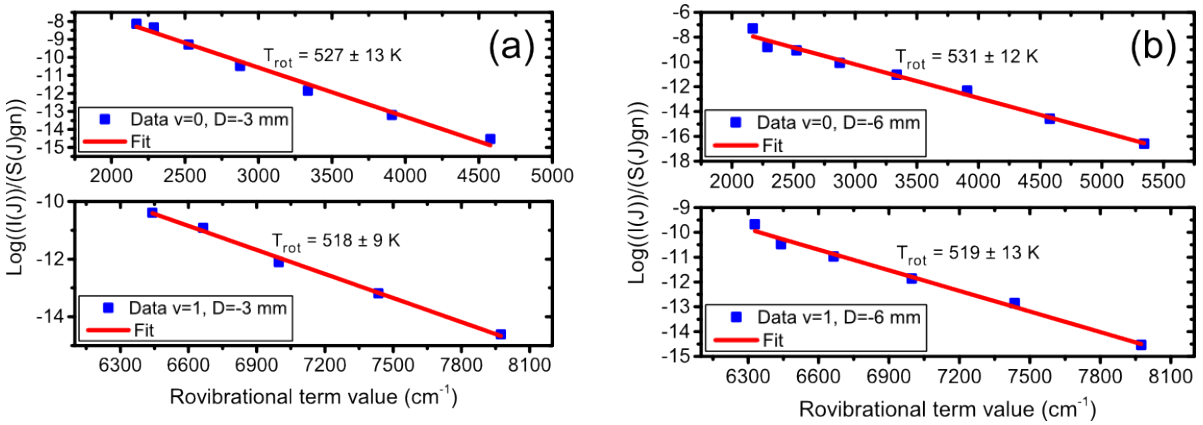

Figure 3.22: (a) shows the Boltzmann plots using the measured spectrum data at $D = -3$ mm in the $v'' = 0$ and $v' = 1$ in the non-equilibrium discharge. The rotational temperatures are 527 ± 13 and 518 ± 9 K respectively. (b) shows the Boltzmann plots at $D = -6$ mm and the rotational temperatures are found to be 531 ± 12 and 519 ± 13 K for $v'' = 0$ and $v' = 1$ respectively.

The Boltzmann plots for the $v'' = 0$ and $v' = 1$ at $D = -3$ mm is produced to calculate the rotational temperature of the H_2 molecule as shown in figure 3.22(a). The resulting slope is $-0.00273 \pm 1.3803 \times 10^{-4}$ and $-0.00278 \pm 9.4465 \times 10^{-5}$ for $v'' = 0$ and $v' = 1$ respectively. Therefore, the rotational temperature at $D = -3$ mm is calculated to be 527 ± 13 K for $v'' = 0$ and 518 ± 9K for $v' = 1$. The Boltzmann plots for the $v'' = 0$ and $v' = 1$ at $D = -6$ mm are produced to calculate the rotational temperature of the H_2 molecule as shown in figure 3.22(b). The resulting slope is $-0.00271 \pm 1.2748 \times 10^{-4}$ and $-0.00277 \pm 1.4185 \times 10^{-4}$ for $v'' = 0$ and $v' = 1$ respectively. Therefore, the rotational temperature at $D = -6$ mm is calculated to be 531 ± 12 K for $v'' = 0$ and 519 ± 13K for $v' = 1$.

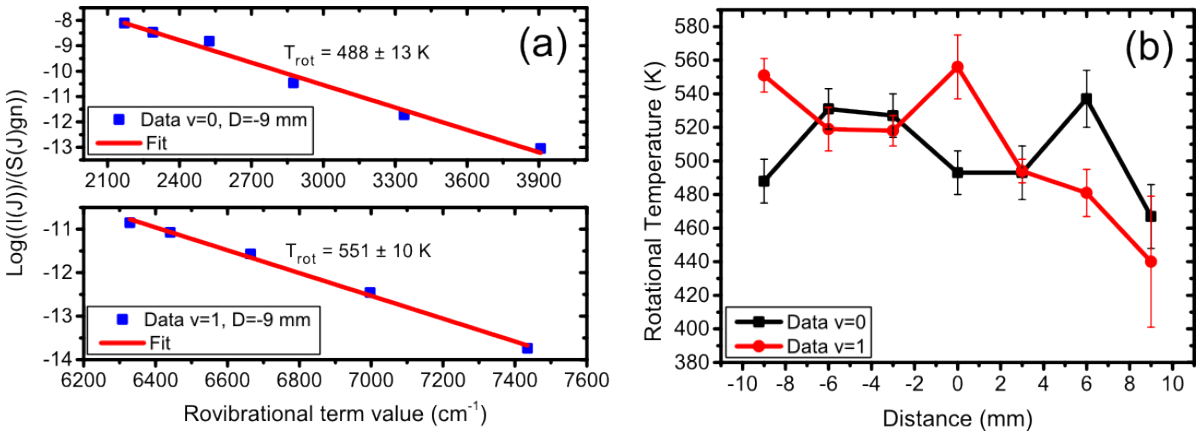

Figure 3.23: (a) shows the Boltzmann plots using the measured spectrum data at $D = -9$ mm in the $v'' = 0$ and $v' = 1$ in the non-equilibrium discharge. The rotational temperatures are found to be 488 ± 13 and 551 ± 10 K respectively. (b) shows the combined radial rotational temperatures at all measured distances.

The Boltzmann plots for the $v'' = 0$ and $v' = 1$ at $D = -9$ mm are produced to calculate the rotational temperature of the H_2 molecule as shown in figure 3.23(a). The resulting slope is $-0.00295 \pm 1.6814 \times 10^{-4}$ and $-0.00262 \pm 9.5328 \times 10^{-5}$ for $v'' = 0$ and $v' = 1$ respectively. Therefore, the rotational temperature at $D = -9$ mm is calculated to be 488 ± 13 K for $v'' = 0$ and 551 ± 10K for $v' = 1$.

After determining the rotational temperature of the H_2 molecule at measured different radial distances in the non-equilibrium discharge, we can plot the combined results of the radial distances and rotational temperatures as shown in figure 3.23(b). It can be seen that the rotational temperatures are fluctuates around 500 K for both $v'' = 0$ and $v' = 1$ vibrational states.

3.3.3 Radial vibrational temperatures of the H_2 molecule in the non-equilibrium discharge

In the vibrational temperature calculations, the areas under curve for each rovibrational line in the REMPI spectra are calculated. In order to determine the error in the vibrational temperature, the difference between the raw, as given in table A.1, A.2; and Gaussian function fitted, as given in table A.3, total line intensities is taken as the error in the total line intensity. Table 3.6 shows the measured vibrational temperatures and the total line intensities for different radial points as well as the error in the total line intensities for the $v'' = 0$ and $v' = 1$ vibrational state.

Figure 3.24 shows the radial vibrational temperature of H_2 at the different radial distances in the non-equilibrium discharge. As can be seen in the figure, the temperatures follow a trend fluctuating around ≈ 3000 K. However, two points seem to be very different from the rest, one is at $D = -6$ mm and the other is at $D = -3$ mm measurement. The error bars in these measurements are relatively high compared to the rest and around 50%. The possible reasons why the temperatures in these two point are high compared the rest may be that the error in the total line intensities as a small error in the measurements would have a very large effect in the resulting temperature as seen in equation 3.3. As we had a uniform non-equilibrium discharge, we would expect that the vibrational temperatures within it would be very similar. For the sake of the argument, if we do not take these two measurements into account, the rest of the temperatures in the non-equilibrium discharge are following a stable trend line. This result suggests that the vibrational temperatures of the H_2 molecule in the non-equilibrium discharge are nearly uniform and fluctuates around ≈ 3000 K.

D (mm)	Raw data		Gauss fit data		Error in intensity		T_{vib} (K)
	$v'' = 0$	$v' = 1$	$v'' = 0$	$v' = 1$	$v'' = 0$	$v' = 1$	
0	5.8754×10^{-4}	6.6346×10^{-5}	5.7360×10^{-4}	6.3042×10^{-5}	1.3940×10^{-5}	3.3040×10^{-6}	4621 ± 577
3	6.4014×10^{-4}	5.0879×10^{-5}	6.2770×10^{-4}	4.7420×10^{-5}	1.2440×10^{-5}	3.4590×10^{-6}	2575 ± 230
6	3.1024×10^{-4}	3.0934×10^{-5}	3.0460×10^{-4}	2.9577×10^{-5}	5.6400×10^{-6}	1.3570×10^{-6}	3606 ± 302
9	1.6536×10^{-4}	1.6576×10^{-5}	1.7135×10^{-4}	1.5575×10^{-5}	5.9900×10^{-6}	1.0010×10^{-6}	3640 ± 457
−3	4.3099×10^{-4}	6.3590×10^{-5}	4.3413×10^{-4}	5.9973×10^{-5}	3.1400×10^{-6}	3.6170×10^{-6}	11702 ± 3845
−6	4.4530×10^{-4}	6.9542×10^{-5}	4.4498×10^{-4}	6.5244×10^{-5}	3.2000×10^{-6}	4.2980×10^{-6}	17350 ± 9111
−9	4.3512×10^{-4}	3.5157×10^{-5}	4.3468×10^{-4}	3.4083×10^{-5}	4.4000×10^{-7}	1.0740×10^{-6}	2630 ± 104

Table 3.6: Radial vibrational temperature measurements of H_2 in the non-equilibrium discharge. Total line intensities in the $v'' = 0$ and $v' = 1$ for raw and Gaussian function fitted data are illustrated. The vibrational temperatures measurements at each radial distance in the non-equilibrium discharge is shown.

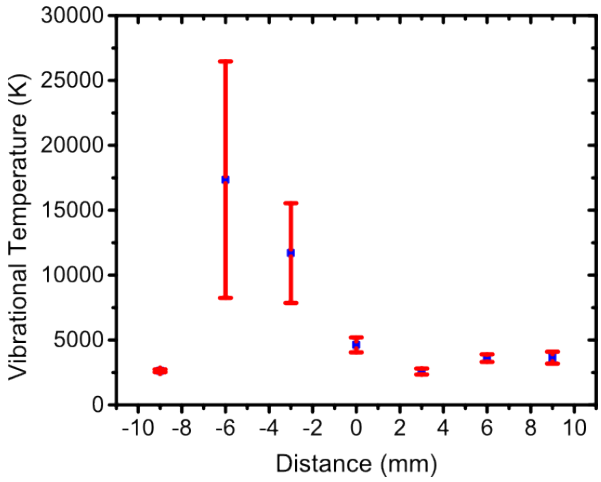

Figure 3.24: The radial vibrational temperatures of H_2 at all measured radial distances in the non-equilibrium discharge.

3.3.4 Radial translational temperatures of the H_2 molecule in the non-equilibrium discharge

Radial translational temperatures of H_2 will be established by employing the measured $(2+1)$ REMPI spectra for the $v'' = 0$ and $v' = 1$. Table A.4, A.5 and A.6 show raw and Gauss fitted linewidths at FWHM of the rovibrational transitions for the $v'' = 0$ and $v' = 1$ at $D = 0$ mm. The error in the FWHM is calculated by taking the difference between the raw and Gauss fitted FWHM data. The Doppler width for each transition is determined by subtracting the laser linewidth from the raw data. Translational temperatures are calculated by employing the Doppler width and corresponding error factor and listed in the same table.

Figure 3.25 shows the radial translational temperature distributions of H_2 in the $v'' = 0$ and $v' = 1$ in the non-equilibrium discharge. Data points in the figure are calculated as the average translational temperature for each vibrational state at the corresponding radial distance. As can be seen in the figure, the overall translational temperature in the $v'' = 0$ is higher than the

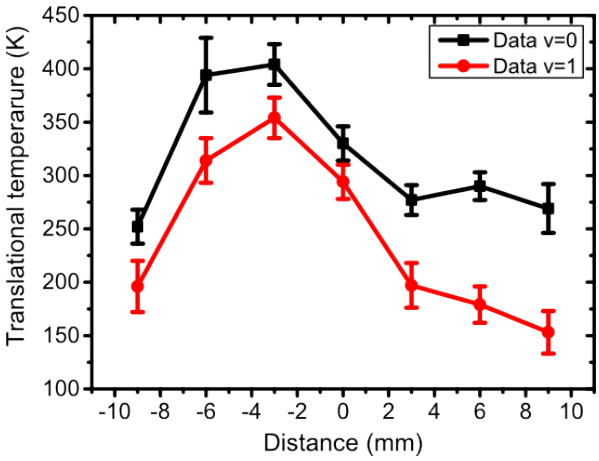

Figure 3.25: The radial translational temperatures of the H_2 molecule at all measured radial distances for both $v'' = 0$ and $v' = 1$ in the non-equilibrium discharge.

translational temperature in the $v' = 1$.

3.4 Conclusion

In this chapter, the production of the vibrationally excited H_2 molecules in the non-equilibrium discharge is achieved. The vibrationally excited H_2 molecules in the $v' = 1$ in the non-equilibrium discharge are measured by the $(2+1)$ REMPI process. This measurement verified the probe wavelength for the SRP scheme. It also proved the feasibility of the $(2+1)$ REMPI process as a detection tool. In addition, the characterization via the H_2 $(2+1)$ REMPI precess was carried out both at room temperature and in the non-equilibrium discharge. In the characterization process, H_2 $(2+1)$ REMPI spectra for the $v'' = 0$ and $v' = 1$ vibrational states in the non-equilibrium discharge was measured. These measurements are carried out for H_2 Q-branch transitions. From the measured H_2 $(2+1)$ REMPI spectra the rotational, vibrational and translational temperature of the H_2 molecule in the non-equilibrium discharge were deter-

mined. The vibrational temperature is measured to be around ≈ 3000 K whereas the rotational and translational are to be few hundred degrees only. With these findings, we conclude that we produced a non-equilibrium discharge ($T_{\text{vib}} > T_{\text{trans}}$) in which the energy gained in vibrational excitation is greater than the energy lost by vibrational to translational ($V - T$) relaxation. Furthermore, the radial temperatures of the H_2 molecule in the non-equilibrium discharge have been measured via the $(2+1)$ REMPI process for the first time.

Our temperature measurements agree with some of the other studies reported. In a study reported by Mendez et. al. [33] the vibrational temperature of H_2 molecules in low pressure ($\approx 0.008 - 0.2$ mbar) DC plasma was found to be 3000 K by using optical emission spectroscopy. Also, the H_2 rotational temperatures determined from the emission measurements were in the $300 - 350$ K range and they correspond to the gas temperature. In another study carried out by Shakhatov et. al. [31] translational, rotational and vibrational temperatures of H_2 in radio frequency inductive discharge plasmas at pressures and power release ranges of $0.5 - 8$ torrs and $0.5 - 2$ W/cm^3 have been measured by using multiplex CARS spectroscopy. The results showed that a decrease of the vibrational temperature from 4250 to 2800 K by increasing the pressure from $0.5 - 8$ torr and a corresponding increase of the rotational temperature from 525 to 750 K. In another study reported by Amorim et. al. [37], the positive column of a hydrogen glow discharge was studied under typical operating conditions: gas pressure from 0.3 up to 5 torr and discharge current from 1 up to 50 mA. Optical emission spectroscopy have been employed in order to determine the gas temperature ($300 < T_{\text{g}} < 600$ K).

Although we measured the Q-branch transitions of H_2 for the temperature measurements, the O-branch and S-branch transitions can be measured as well. Since the probability of Q-branch transitions are much greater than the O-branch and S-branch ones, the amplification of the $(2+1)$ REMPI signal might be required. The $(2+1)$ REMPI laser wavelengths for the O-branch and S-branch transitions in the H_2 molecule are given in appendix table B.2 and B.3.

Even though we have measured the vibrational temperature by establishing the H_2 $(2+1)$

REMPI spectra in the $v'' = 0$ and $v' = 1$ vibrational states, more accurate vibrational temperature can be determined by measuring the higher vibrationally excited states, such as $v = 2$. Our UV wavelength range is limited by the THG crystal which can produce UV light up to a certain range. If this limitation is overcome, the rovibrational populations of $v = 2$ vibrational state can be measured as well. The $(2 + 1)$ REMPI laser wavelengths for H_2 Q-branch transitions at $v = 2$ vibrational state are given in appendix table B.1.

Lastly, because the radial temperature measurements are carried within the non-equilibrium discharge, a significant drop in the vibrational temperature was not observed. As discussed previously, the vibrationally excited molecules start to deactivate by diffusion of the vibrationally excited H_2 molecules in the discharge wall expressed as $H_2(v) \xrightarrow{\nu_{\text{wall}}} H_2(0)$. In order to measure this effect, a few more measurements need to be conducted in the boundary between the non-equilibrium discharge and the surrounding gas in the glass cell. These new radial distances would be further than the distance that has already been measured.

Chapter 4

Raman excitation of $v = 1$ in hydrogen molecules (H_2)

One of the best optical pathways for revealing a molecule's vibrational spectrum is through coherent anti-Stokes Raman scattering (CARS) non-linear spectroscopy. In CARS, a molecule's vibrational modes are excited into motion with simultaneous interaction of pump and Stokes photons generated by pulsed lasers with high peak powers. In this chapter, Raman excitation of $v = 1$ in Hydrogen molecules by CARS spectroscopy will be explained. The reason for this experiment, as mentioned in introduction, is to determine our pump laser's wavelength to be used for the SRP scheme.

4.1 Coherent anti-Stokes Raman Spectroscopy (CARS)

Coherent anti-Stokes Raman scattering (CARS) was first observed by Terhune and Maker [149, 150]. This spectroscopic technique is one of the non-linear Raman processes that have been established with the accessibility of lasers. Examples for different Raman processes may

include techniques such as conventional, spontaneous Raman scattering [151], Resonance Raman scattering [152], Inverse Raman scattering [153], Hyper Raman scattering [154], and the Raman-induced Kerr effect [155]. CARS is one of the most powerful methods of non-linear spectroscopy, which has found many applications in gas-phase and plasma diagnostics, studies of molecular relaxation processes, temperature and concentration measurements, condensed-phase studies and, recently, in femtosecond chemistry [156, 157]. Numerous of CARS setup have become a routine tool of modern optical experiments, described comprehensively in books and reviews [158–162].

CARS is potentially a powerful method since its capacity in attaining analytical and spectroscopic information pertaining to Raman active resonances in gases, liquids, and solids. By this technique, spectral resonances corresponding to vibrational transitions could be observed by mixing together two visible laser beams. CARS is a third-order non-linear effect. In contrast to second-order non-linear processes, it is generally applicable to isotropic in addition to a non-centrosymmetric medium. Moreover, its conversion efficiency to coherently produced photons is significantly higher than conventional, spontaneous Raman scattering (CARS offers a 10^5 improvement in conversion efficiency [163]). It appears to be a practical tool for obtaining spectra of luminescent samples (fluorescent materials, impurities, combustion systems, and electric discharges) and of certain solutes in solution [157]. Due to all of the mentioned advantages, we employed CARS to experimentally determine the pump wavelength to be used in the SRP scheme.

CARS is a coherent third order non-linear optical process in which fields at ω_1 and ω_2 mix via the third order non-linear susceptibility of the medium to generate a non-linear polarisation that oscillates at $2\omega_1 - \omega_2$. This is resonance enhanced if $\omega_1 - \omega_2$ matches a Raman active (vibration-rotation transition) in the medium as depicted in figure 4.1 where ω_1 and ω_2 are ω_{pump} and ω_{Stokes} fields, respectively. The signal field generated at $2\omega_1 - \omega_2$ needs to be in phase

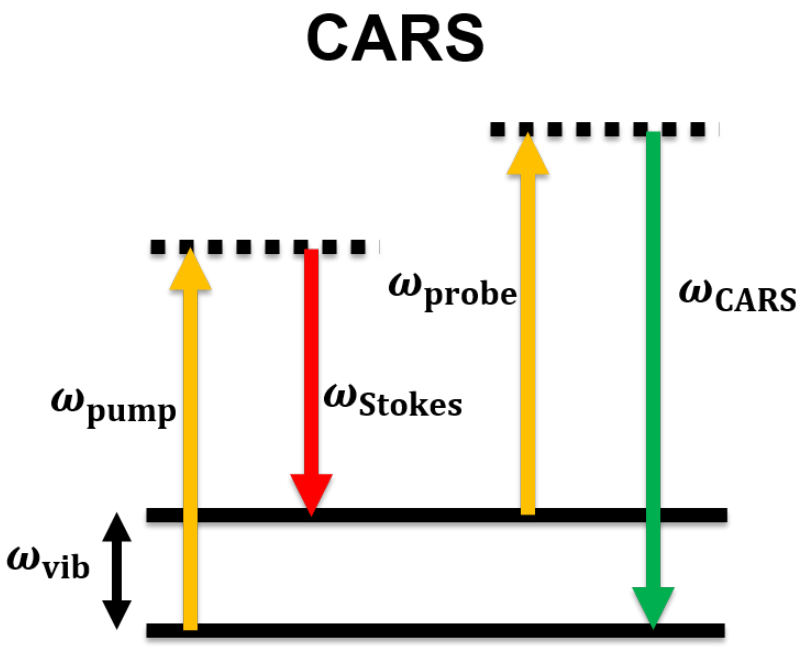

Figure 4.1: CARS energy diagram is illustrated. It is coherent third order nonlinear optical process in which fields ω_{pump} and ω_{Stokes} mix via the third order non-linear susceptibility of the medium to generate a nonlinear polarisation that oscillates at $2\omega_{\text{pump}} - \omega_{\text{Stokes}}$ this is resonantly enhanced if $\omega_{\text{pump}} - \omega_{\text{Stokes}}$ match a Raman active vibration-rotation in the medium.

with the non-linear polarisation generated by the pump fields at ω_1 and ω_2 for this to happen:

$$2\mathbf{k}(\omega_1) - \mathbf{k}(\omega_2) = \mathbf{k}(2\omega_1 - \omega_2). \tag{4.1}$$

Due to material dispersion this is not the case and the wave vector mismatch $\Delta\mathbf{k}$ is finite [164, 165], the degree of dispersion in dilute gases is not high and the coherence length (when $\Delta\mathbf{kL} = \pi$) for rotation vibration resonances in H_2 is ≈ 10 cm for a collinear geometry [165]. In the case of collinear geometry, phase matching and dependence of CARS signal on $\Delta\mathbf{k}$ are discussed in appendix section C. An alternative to a collinear geometry is BOXCARS. The

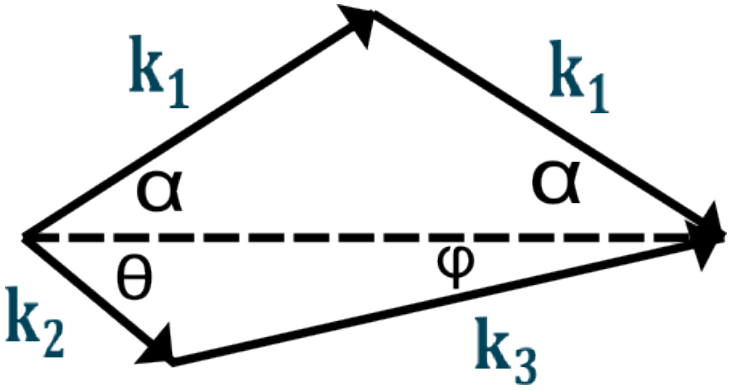

Figure 4.2: Vector diagram for non-collinear BOXCARS scheme.

BOXCARS scheme [166] satisfies phase-matching condition $(2\vec{\mathbf{k}}_1 - \vec{\mathbf{k}}_2 = \vec{\mathbf{k}}_{\text{signal}})$ with non-collinear interaction. In this scheme, the pumping beam ω_1 is split into two beams that are then forced to converge at an angle of 2α, while the beam ω_2 is oriented at an angle of θ, so that the scattering direction is determined by the angle ϕ 4.2.

The CARS technique requires two comparatively high-powered (usually pulsed) laser beams at frequencies ω_{p} and ω_{s} that are focused together in a sample. As a result of non-linear mixing two laser beams, a coherent beam resembling a low intensity laser beam at frequency, $\omega_{\text{as}} = 2\omega_{\text{p}} - \omega_{\text{s}}$, is produced in the medium. The efficiency of conversion to frequency ω_{as} depends critically upon the presence of molecular resonances at a frequency $\omega_{\text{p}} - \omega_{\text{s}}$, the laser intensities, the resonance line width, and the number density of species [167]. The theory behind the CARS process is explained in appendix C.

4.2 Calculation of CARS wavelength

There are vibrations and rotations of molecules which are visible in the Raman Spectrum, but not in the infra-red or microwave spectra. For instance, diatomic molecules such as H_2 , N_2 or O_2 can be investigated merely with Raman spectroscopy, since their rotations and vibrations

are infra-red inactive. For a molecule to be Raman active, it has to obey selection rules for ro-vibrational Raman spectrum. This process is a two-photon process. In the Raman spectrum, the selection rules are $\Delta v = \pm 1$ for vibrational transitions, where Stokes lines are assigned to $\Delta v = +1$, and anti-Stokes lines are assigned to $\Delta v = -1$. In addition, the selection rules for the rotational transitions are $\Delta J = 0, \pm 2$, where the S-branch transitions are assigned to $\Delta J = +2$, the Q-branch transitions to $\Delta J = 0$, and the O-branch transitions to $\Delta J = -2$ respectively.

In our work, CARS wavelength is calculated for H_2 molecules. In order to calculate wavelength of CARS in the Hydrogen molecule, S-branch transition which is from $v'' = 0$, $J'' = 1$ to $v' = 1$, $J' = 3$ is chosen. The ro-vibrational quantum state $v'' = 0$, $J'' = 1$ in the ground electronic state is chosen because is the most populated state at the room temperature. Vibrational constant (ω_{vib}) for this particular transition is 4712.91 cm$^{-1}(\bar{v}_v)$ [168, 169]. For simplicity, the wavenumber units is used for frequency calculation. Firstly, we determined the Stokes laser (IR laser) wavelength which is the one of the optical lattice beams as mentioned in the chapter one. Thus, the Stokes wavelength is calculated to be at 1064.555 nm which is 9393.60 cm$^{-1}(\bar{v}_{\text{s}})$ in wavenumbers. By using the expression of $\bar{v}_{\text{p}} = \bar{v}_v + \bar{v}_{\text{s}}$, where "p" and "s" subscripts are for the pump and the Stokes beam respectively. Now, we can calculate $\bar{v}_p = 14106.51$ cm^{-1} and this corresponds to 708.893 nm. Then, CARS wavelength can be calculated by the expression of $\bar{v}_{\text{cars}} = \bar{v}_v + \bar{v}_{\text{p}}$. Therefore, we are able to determine $\bar{v}_{\text{cars}} = 18819.42$ cm^{-1} which is 531.370 nm as shown in figure 4.3.

In addition to this, CARS wavelength is calculated for Q-branch transition in H_2 which is from $v'' = 0$, $J'' = 1$ to $v' = 1$, $J' = 1$. The intensity of scattering is proportional to the space-averaged squares of the transition polarisability tensor components or [159]:

$$I^{\Omega} \approx b_{J\pm 2,J}(\gamma)_0^2 \tag{4.2}$$

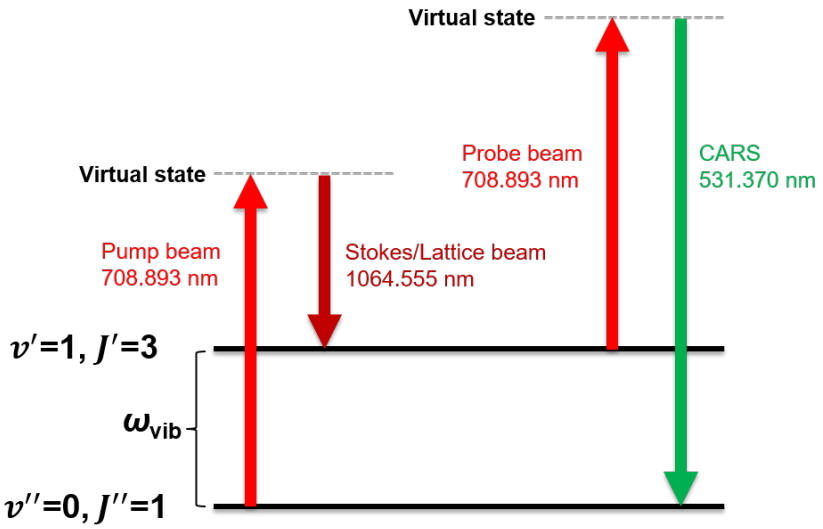

Figure 4.3: CARS process in H_2 molecule. The pump beam at 708.893 nm excites the H_2 molecule from the ground state $v'' = 0$, $J'' = 1$ to a virtual state. From there, the Stokes beam(IR lattice beam) at 1064.555 nm simultaneously takes the molecule down to the vibrationally excited state $v' = 1$, $J' = 3$. Then, the probe beam at 708.893 nm promotes the vibrationally excited molecule to a virtual state again. Next, since the molecule cannot stay in the virtual state, it will fall back instantaneously to the ground state by emitting a CARS photon at 531.370 nm.

where $b_{J\pm2,J}$ are called Placzek-Teller coefficients and give by

$$b_{J+2,J} = \frac{3(J+1)(J+2)}{2(2J+1)(2J+3)} \tag{4.3}$$

$$b_{J-2,J} = \frac{3J(J-1)}{2(2J+1)(2J-1)} \tag{4.4}$$

$$b_{J,J} = \frac{J(J+1)}{(2J-1)(2J+3)} \tag{4.5}$$

and $(\gamma)_0$ is the anisotropy of the equilibrium polarisability tensor. Since the intensity of scattering is proportional to the Placzed-Teller coefficients, the Q-branch transitions scattering intensity is higher than S-branch one. Thus, the resulting CARS signal is greater for the Q-branch

transition. Vibrational constant for this transition is 4155.25 cm^{-1} and corresponding wavelengths are calculated by the same procedure as the S-branch transition mentioned earlier in this section. Hence, assuming we have our Stokes beam (IR lattice beam) at the wavelength of 1064.555 nm, which is 9393.60 cm^{-1}, then the corresponding pump beam wavelength can be calculated to be at 738.07 nm, which is 13458.85 cm^{-1}. As a result, the CARS wavelength is found out to be at 564.84 nm, which is 17704.1 cm^{-1}. In the next section, the experimental setup, for determining the pump beam wavelength via CARS process, will be explained.

4.3 Experimental setup

This section will explain the experimental setup for the CARS experiment. To conduct the CARS experiment, two laser beams are used. One is the pump beam provided by ND6000 dye laser (ND6000, Continuum, USA) and the other one is the Stokes beam generated by the Custom laser (Custom, Continuum, USA). In order to realize the CARS process, these two beams have to be spatially and temporally overlapped in a cell that contains H_2 molecules. Now, we will initially discuss the laser system that generates the required two beams for this process.

4.3.1 Laser system

The laser system consists of a Continuum Custom laser and ND6000 dye laser. we will briefly explain the later one fist.

Dye laser

ND6000 Dye laser (Continuum) generates the pump beam required for the CARS process. The dye laser is pumped by a pulsed Nd:YAG laser (Spectra-Physics, Quanta-Ray Pro-series)

which has a frequency doubled output at 532 nm and repetition rate of 10 Hz. The operational principle of the Spectra-physics Nd:YAG laser is the same as the one in chapter 3 and its optical setup explained in details. For generating the required tunable output of the ND6000 dye laser (700 to 740 nm), LDS 750 dye solutions (in methanol) of 114 mg/l and 20 mg/l were used in the oscillator and amplifier stages respectively. This produced the required tunable output with a maximum output energy at 719 nm.

Custom-built (IR) laser

One beam of a custom-built (IR) laser is used as a Stokes beam for the CARS experiment. The custom-built high-energy chirped laser system has specifically designed for optical Stark acceleration/deceleration and developed in our research group [23, 25]. It has two pulsed outputs. The laser system is initially derived from a single 1064 nm Nd:YVO_4 microchip laser that can be rapidly frequency-tuned by an electro-optic crystal in the cavity. This output injection locks a laser diode, which is coupled into a commercial fibre amplifier that amplifies the power to 1 W. The beam then is chopped into two pulses by a commercial electro-optic pulse shaper. Then, two pulses are split and coupled into two optical fibres, one is 55 m longer than the other. The resulting difference creates a time delay of 275 ns between the pulses at the exit of the fibres, which paves a way to create a well defined frequency difference when the microchip laser is chirped. On the exit of fibres, the pulses are amplified by two sets of flash lamp pumped, pulsed Nd:YAG amplifiers to produce high intensities. This laser system is capable of producing two high power beams with flat-top temporal profiles, where the frequency difference can be chirped by up to 1.1 GHz over the pulse duration of 140 ns [25]. Before the measurements, both custom-built and ND6000 laser's wavelength are checked and calibrated with a wavemetre. WS-6 (WS-6, HighFinesse GmbH, Germany) and Burleigh (WA-2000, Burleigh Instruments, USA) wavemetres are used for ND6000 and Custom laser's beam

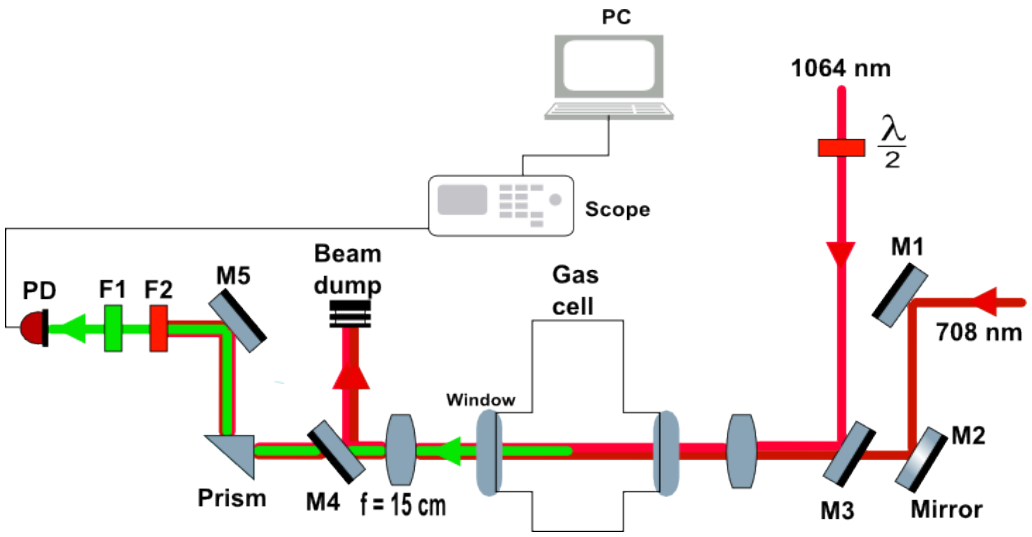

Figure 4.4: Experimental setup for CARS process in H_2 molecule. The pump beam at 708.893 nm and the Stokes beam (IR lattice beam) at 1064.555 nm are co-propagated and spatially and temporally overlapped in the H_2 gas cell. The resulting CARS beam is shown in green and detected by a photodiode (PD) after the residual pump and Stokes beams are filtered out.

respectively.

4.3.2 Optical layout

The experimental setup for CARS experiment is shown in figure 4.4. The CARS process includes two co-propagating laser beam. The IR beam at 1064 nm from the Custom laser is employed as the Stokes beam, which is also one of the lattice beams. The beam at ≈ 708 nm from the ND6000 dye laser is used as the pump beam. Since it is crucial that the pump and Stokes filed have parallel linear polarisations [170], a half-wave plate $(\frac{\lambda}{2})$ is placed in the Stokes beam path in order to parallel polarize it with respect to pump beam. When the two fileds have the same polarisations, the resulting signal is greatly enhanced. Two collinear beams

are focused into the gas cell by a 15 cm lens. After overlapping the two beams spatially and temporally at focal point, the CARS signal is generated and it is represented as green beam in the diagram. To filter the CARS beam from the residual pump and Stokes beam, some filtering optics are employed. At the exit of the gas cell another 15 cm lens is used to collimated the beams. M4 mirror is mounted after the collimating lens to filter the most of the residual pump and Stokes beam. Then, to filter the remaining the small portion Stokes and pump beam, F1 and F2 filters are employed. F2 filters the remaining Stokes beam and F1 only lets the CARS beam. At the end, only the CARS beam reaches the photodiode and this signal is sent to the scope to be detected before being recorded on PC.

4.3.3 Alignment

Spatial overlap

Since the CARS experiment consists of two co-propagating laser beams, the alignment challenge is to spatially overlap these beams in confocal point. To achieve the overlapping, a specially designed aluminium plate with a few mm hole in the middle is blue-tagged onto focussing and collimating lenses shown in the figure 4.4. Firstly, the Stokes (1064 nm) beam is aligned through the holes on the aluminium plate by walking the beam method. Once this is done, the pump beam (708 nm) is aligned though the both holes using the same method. After that, to ensure the two beams are overlapped at focal point of the focussing lens, a 50 μm pin hole on a translational stage is placed at the focal point. Initially the pin hole is adjusted where the Stokes beam is focused. Then, the pump beam is aligned through the pin hole. Thus, two beams are spatially overlapped.

Temporal overlap

The temporal overlap between the pump and Stokes pulses is achieved by employing two delay/pulse generators (Model DG535, Stanford Research Systems, USA). Both pulses are triggered from the electrical output of the custom built laser via two independently controllable delay/pulse generators (Model DG535, Stanford Research Systems, USA).The pulse outputs are detected by an amplified photodiode input to an oscilloscope (Wavepro 7300, LeCoy, USA) where the degree of overlap can be observed as the delay generator settings are adjusted.

4.3.4 CARS signal detection and data acquisition

The CARS signal is detected using a photodiode as shown in the figure 4.4. The signal is monitored on oscilloscope before data recorded on a PC. Data acquisition for CARS signal is similar to the one for the REMPI signal as explained in the section 3.1.4 of the chapter 3. In CARS experiment, the signal is obtained by the photodiode and each data point is averaged for 20 laser shots on the scope. The data acquired by scanning the ND6000 dye laser over the expected resonant peak of CARS signal and the data from the scope is recorded on PC. Before scanning the pump laser to record the signal, the expected pump beam is calculated with respect to Stokes beam and the resulting CARS wavelength is determined as shown in the figure 4.3. A Labview program controlled both the dye laser and the oscilloscope during the acquisition process.

4.4 Results

This section will explain the results obtained from the CARS experiment. Before taking the measurements, the experimental parameters were optimized. Initially, both ND6000 dye, which generates the pump beam, and Custom laser, which produces the Stokes beam, output

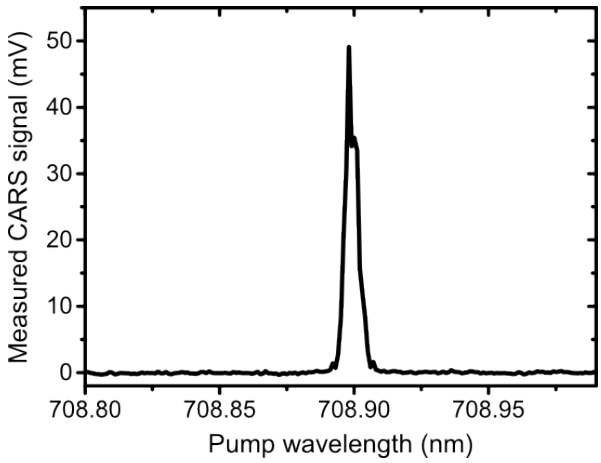

Figure 4.5: CARS signal in H_2 molecule for S-branch transition is shown in the figure. The pump and Stokes beam wavelengths are 708.899 nm and 1064.555 nm respectively. The resulting CARS signal's wavelength is at 531.370 nm which is in green spectral range.

power were optimized to be sufficiently high for the CARS process. The intensity of the beams need to be around $\approx 10^{10}$ W/cm^2 for the CARS process. ND6000 dye laser had output power of ≈ 5 mJ/pulse with pulse duration of 10 ns. Custom laser had output power of ≈ 70 mJ/pulse with pulse duration of 140 ns. The beam waists for the pump and Stokes beam were measured to be 68 μm and 46 μm respectively. Therefore, the intensities for the pump and Stokes beams at focus were calculated to be 5×10^9 W/cm^2 and 1×10^{10} W/cm^2. Gas mixture of 10% H_2 in Neon is used in the gas cell.

4.4.1 Measured CARS signal

The first measurement of the CARS signal was carried out at S-branch transition in H_2. Figure 4.5 shows the measured signal at 600 torr for the S-branch transition in H_2. In S-branch transition, the molecules are excited from $v'' = 0,\ J'' = 1$ to $v' = 1,\ J' = 3$ rovibrational level in the ground state of H_2. To produce the resonant CARS signal, the pump laser is scanned over

≈ 708.800 to 709.000 nm while the Stokes beam wavelength is being constant at 1064.555 nm. The ND6000 dye laser is scanned with 0.005 nm step size in order not to miss the resonant peak. The CARS signal is peaked at ≈ 708.90 nm which is the pump wavelength to achieve the CARS process. The corresponding CARS beam wavelength is at 531.370 nm which is in the green region of the spectrum.

4.4.2 CARS signal vs pressure

CARS signal versus gas pressure measurement is carried out to determine the dependence of the signal strength on the pressure. Figure 4.6 shows the CARS signal's dependence on pressure (number density). The measurement was conducted for a range of pressures starting from 200 to 600 torr. During these measurements, all other experimental parameters were maintained to be the same apart from the gas pressure in the cell. As can be seen in the figure, the CARS signal increases by rising the number density of molecules. When pressure is 200 torrs, the signal almost disappears. Whereas, the strength of the CARS signal improves exponentially by adding more gas molecules into the glass cell. It should be noted that we use a gas mixture of 10% H_2 in Ne. Thus, the H_2 molecules has a partial density of 10% in the gas mixture.

Figure 4.7 illustrates the CARS signal at different gas pressures. Each data point in the figure is obtained from the CARS signal dependence on pressure measurements as shown in the figure 4.6. Data points for the various pressures are fitted to an exponential function on the Origin lab. As mentioned in the theory section C, CARS signal has a square dependence on the number density of the gas. The CARS signal increases exponentially as the pressure goes up in our measurement. Thus, it is suffice to state that the CARS signal dependence on the number density measurement reflects an agreement with the theory.

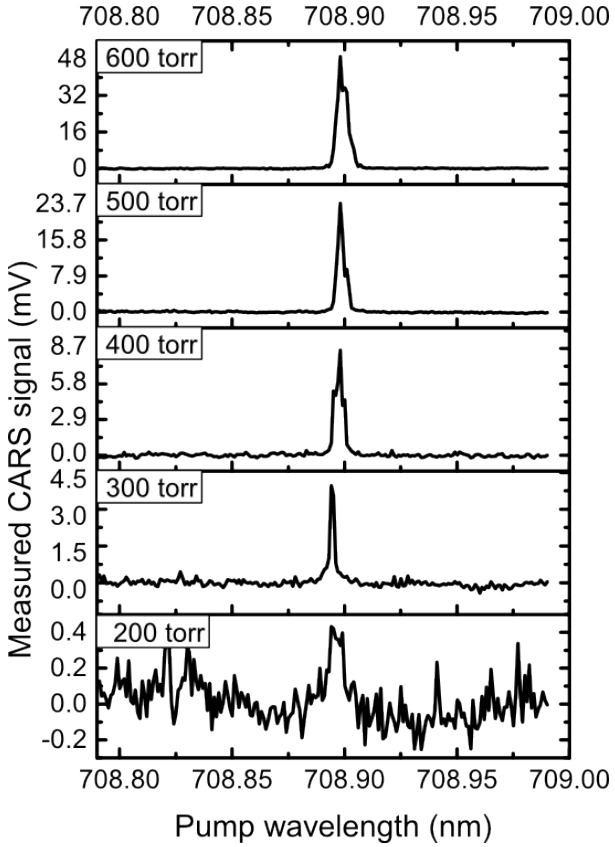

Figure 4.6: CARS signal versus different gas pressures ranging from 200 to 600 torr in H_2 molecule for S-branch transition.

4.4.3 Improved CARS signal at Q-branch transition

Improved CARS signal is produced by measuring the H_2 Q-branch transition. The signal for Q-branch is improved compared the initial measurement for the S-branch because the transition probability of Q-branch is greater than S-branch one. The measured Q-branch transition of H_2 is from $v'' = 0,\ J'' = 1$ to $v' = 1,\ J' = 1$ rovibrational level in the ground electronic state. Figure 4.8 shows the measured CARS signal for this transition. The measured pump beam is peaked at 738.070 nm while the Stokes beam wavelength is at 1064.555 nm. Thus, the resulting CARS

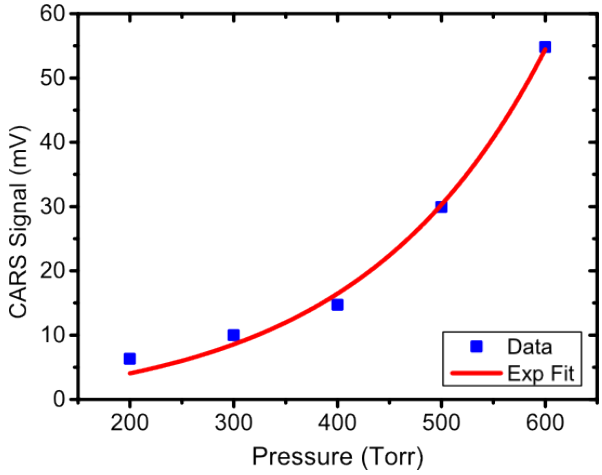

Figure 4.7: CARS signal versus different gas pressures ranging from 200 to 600 torr in H_2 molecule for S-branch transition. The data points are fitted to an exponential function.

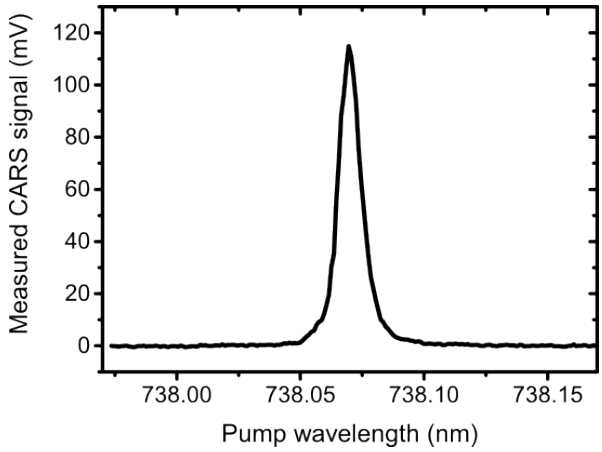

Figure 4.8: Improved CARS signal at H_2 Q-branch transition is shown in the figure. The pump beam wavelength is at 738.070 nm while the Stokes one is at 1064.555 nm. The resulting CARS beam is at 564.840 nm.

beam is at 564.840 nm which is at the green part of the visible spectrum. The CARS signal could be seen by eyes in this measurement. The fact that CARS signal is high enough to be

seen by eyes indicates a significant increase in the number of H_2 molecules excited to $v' = 1$ vibrational state.

4.5 Conclusion

In this chapter, we determine the pump wavelength to be employed in the SRP precess. CARS experiment is successfully conducted for H_2 S-branch and Q-branch transitions. The results determined not only the pump wavelength for the SRP scheme but also verified the feasibility of producing the vibrationally excited H_2 molecules at $v' = 1$ using our laser system.

Although we measured the CARS signal for H_2 S- and Q-branches for our measurements, the O-branch transition can be detected as well. In addition, CARS process can be used to determine the temperature of the molecule by determining the several rovibrational level populations of the molecule. The limitation in CARS process is that at low number densities it is not very efficient because the efficiency of the process is highly dependent on the number density of the gas.

CARS spectroscopy is a well established technique. Studies reported on determination of the vibrational, gas and rotational temperatures of H_2 in discharge plasmas [31] as well as concentration measurement in H_2 [165] by using CARS. It has also been used in part to achieve the preparation of oriented and aligned H_2 and HD by stimulated Raman pumping [170].

Chapter 5

Future outlook

In this chapter, we will outline improvements to the experimental set-up as well as suggestions to extend this work. This thesis presented work towards an efficient detection scheme for decelerated H_2 molecules in optical lattices. The feasibility of such a detection scheme has been verified by conducting two independent experiments. The first is the detection vibrationally excited H_2 molecules in the $v = 1$ state using a $(2+1)$ REMPI scheme. Here, the excited gas is produced in a non-equilibrium discharge. A second detection scheme, known as CARS, detects these same excited molecules but uses the $v = 1$ state created by laser excitation. In order to successfully implement detection of decelerated H_2 molecules, a number of improvements to the complex deceleration experiment should be considered. In this chapter a discussion on these improvements as well as a range of extension projects is presented. The detection scheme presented in this thesis has been implemented to detect H_2 in a molecular beam in our group and presented elsewhere [26]. The detection scheme utilises the stimulated Raman pumping of the H_2 molecules to the excited $v = 1$ state and subsequent ionisation via $(2 + 1)$ REMPI scheme. Therefore, one can efficiently detect only the molecules in the optical lattice where all detection beams are overlapped in the optical deceleration experiment. To achieve this, the

detection scheme needs to be improved before attempting to decelerate the molecules in the optical lattices. Since it is a non-linear process, the pump and probe laser needs to be optimized to their optimum power. Also, the detection depends on the number density quadratically, thus the density in the molecular beam needs to be sufficiently high. A study by Bartlett et. al. [29] reported that the presence of electric fields on the order of 10^7 V/cm arising from the pulsed SRP laser beams is sufficient to shift the line position of the REMPI transition to such an extent that the estimate of the pumping efficiency is overestimated unless this shift is accounted for. As we use high power laser beams, this effect needs to be considered for any future deceleration experiments.

5.1 Chirped optical Stark deceleration of H_2

Optical Stark deceleration is a technique that traps and decelerates cold molecules generated in a molecular beam and takes them to rest in the lab frame. This occurs in a two stage process. First, the molecules are cooled by collisions with rare gas atoms in a supersonic expansion reaching temperatures in the 1 K range. However, these molecules still possess a high velocity spread (few hundred m/s), so a second phase of velocity reduction is implemented in which a portion of these molecules are trapped and can be slowed. In optical Stark deceleration, the interaction between an induced dipole moment of the molecule and the intense optical field creates the potential needed for trapping the molecule. In principle, any molecule or atom can be manipulated and decelerated in this way because all molecules can be polarised in this manner. Previous experiments have demonstrated using a moving lattice potential to slow molecules where a half phase space rotation (or half oscillation) in the lattice can swiftly decelerate or accelerate molecules [171, 172]. Although this technique can produce a slowed velocity distribution, the lowest achievable energy spread is limited to the initial energy distribution of the molecular beam. Even though this is suitable for loading molecules in a trap, it is not efficient

enough for a range of collision experiments which require a narrow velocity distribution. Theoretical work on the creation of slowed energy distribution which is narrower than the initial molecular beam velocity spread has been done by using optical Stark deceleration [20]. In this scheme, a lattice, which is initially moving at the molecular beam velocity, traps molecules with a narrow energy distribution dictated by the potential well depth. An experiment like this is very advantageous because it is applicable to any molecule. But the detection of the decelerated molecule is highly challenging since they need to be distinguished from the rest in the molecular beam. Indeed, our detection scheme overcomes this challenge.

To create decelerating lattice, a linear frequency chirp is applied onto one of the near counter-propagating laser beams which interfere and produce the moving lattice beams. To realize these experiments an amplified laser has been developed in our research group as explained in chapter 1. This laser system has recently been employed to accelerate metastable argon which cooled which an magneto-optical trap (MOT) to velocities up to 191 m/s in our group [23], thus proving its capability for molecular acceleration/deceleration experiments. A system like this can be used to decelerate/accelerate any molecular or atomic species, although with differing efficiencies because of differences in the polarisability and mass of each species [173].

Within our group, the work on the dipole trapping of both metastable and ground state argon atoms has been carried out [174–176]. In this work, metastable atoms are first Doppler-cooled down to ≈ 80 μK in a MOT on the $4\mathrm{s}[3/2]_2$ to $4\mathrm{p}[5/2]_3$ transitions. A build-up cavity is used to trap cold, ground state argon atoms in a deep optical dipole trap. The atoms are loaded in the trap by quenching them from the cloud of laser cooled metastable argon atoms.

5.2 Sympathetic cooling of Hydrogen molecules

There has been an extensive research on the cooling of molecules over the years. Cold molecules can be used to conduct experiments in high resolution spectroscopy, cold chemistry and collisions. The spectroscopic resolution of a molecule can be significantly increased by internally cooling it [177–179]. Moreover, increased resolution can lead to more accurate measurement of electron's electric dipole moment and fundamental constants such as fine structure constant and ratio of m_p/m_e [180–183]. Molecules at ultracold temperatures can be used to study the chemical reactions. At such low temperatures the reaction rate can increase as quantum tunnelling effects become effective and thus reaction rates can be precisely controlled [14, 184, 185]. Ultracold temperatures also pave a way for high resolution scattering experiments by collision processes [10, 186].

The complex internal structure of molecules makes it more challenging to implement laser cooling as opposed to cooling of atomic species. Various techniques have been developed to cool molecules down to cold and ultracold temperatures. These techniques include using Feshbach resonances [187–189], photoassociation [190–193], molecular beam [194, 195], electrostatic Stark [3, 196, 197] and Zeeman deceleration [198], and buffer gas cooling [199]. However, all these techniques are limited to certain molecules and thus lack a general approach which is applicable to any species. We propose sympathetically cooling any molecule by trapping them together with a laser-cooled ground state noble gas (i.e. Argon) in an optical dipole trap. In principle, sympathetic cooling of molecules simply involves using thermalising elastic collisions between molecular sample and the colder atomic species. Thermalising of these species leads to an overall cooling of the molecules, which are initially hotter.

The Hydrogen molecule is a good candidate for sympathetic cooling because of its importance in astrophysics. Its collisional properties without the presence of a trapping field is easily determined and the high polarisabilty to mass ratio makes it one of the most effective species to

decelerate using optical Stark deceleration [171, 172]. Furthermore, the work came out of this thesis. Work on calculating cold and ultracold cross section for H_2 with He, and Ar have been done [200, 201]. This has been extended to include all the stable rare gas atoms which can be laser cooled and trapped [202, 203]. H_2 is a good case to study as the scattering energy is very low compared to the vibrational-rotational excitation energies, and therefore, merely allowed channel is the elastic one. Under these conditions, the scattering of rare gas - H_2 was modelled as a two-body process [203, 204]. The high collisional cross sections for ^{4}He – H_2 and Ar – H_2 are comparable to those used in sympathetic cooling experiments between cold alkalis [205]. These values stay relatively constant over a wide temperature range [173]. In another study, simulations of Ar – H_2 interactions were studied and revealed thermalisation between the two species on a timescale of several seconds [206]. In this study, calculations were carried out for various atomic and molecular density arrangements and final temperatures of 330 ± 30 μK were determined for one particular case.

Appendices

Appendix A

Radial temperature measurement data in the non-equilibrium discharge

A.1 Data for radial rotational temperatures of H_2

Transition line	Term values (cm^{-1})	$I(J)$ D = 0 mm	$I(J)$ D = 3 mm	$I(J)$ D = 6 mm	$I(J)$ D = 9 mm	$I(J)$ D = −3 mm
$Q_0(0,0)$	2.1703×10^3	5.43943×10^{-5}	5.92244×10^{-5}	3.18272×10^{-5}	1.94636×10^{-5}	3.27003×10^{-5}
$Q_1(0,0)$	2.2887×10^3	2.80997×10^{-4}	3.80484×10^{-4}	1.18998×10^{-4}	8.02251×10^{-8}	2.60038×10^{-4}
$Q_2(0,0)$	2.5245×10^3	9.02391×10^{-5}	7.41071×10^{-5}	6.29137×10^{-5}	3.56357×10^{-5}	5.37808×10^{-5}
$Q_3(0,0)$	2.8754×10^3	1.12028×10^{-4}	9.44935×10^{-5}	7.8337×10^{-5}	2.23159×10^{-5}	6.912×10^{-5}
$Q_4(0,0)$	3.3379×10^3	1.72825×10^{-5}	2.13373×10^{-5}	9.64682×10^{-6}	5.22017×10^{-6}	7.49287×10^{-6}
$Q_5(0,0)$	3.9075×10^3	1.91977×10^{-5}	1.04984×10^{-5}	8.52172×10^{-6}	2.50166×10^{-6}	7.11701×10^{-6}
$Q_6(0,0)$	4.5787×10^3	4.02859×10^{-7}	$--$	$--$	$--$	7.43092×10^{-7}
$Q_0(1,1)$	6.3288×10^3	4.38046×10^{-6}	4.21866×10^{-6}	2.31203×10^{-6}	1.26222×10^{-6}	2.53458×10^{-6}
$Q_1(1,1)$	6.4412×10^3	2.73041×10^{-5}	2.58893×10^{-5}	1.73643×10^{-5}	1.01962×10^{-5}	3.32474×10^{-5}
$Q_2(1,1)$	6.6647×10^3	1.05272×10^{-5}	6.49785×10^{-6}	4.90758×10^{-6}	1.53721×10^{-6}	1.06033×10^{-5}
$Q_3(1,1)$	6.9972×10^3	2.01376×10^{-5}	1.18731×10^{-5}	5.02676×10^{-6}	3.58027×10^{-6}	1.34991×10^{-5}
$Q_4(1,1)$	7.4352×10^3	1.55304×10^{-6}	1.21463×10^{-6}	5.85989×10^{-7}	$--$	1.97000×10^{-6}
$Q_5(1,1)$	7.9742×10^3	2.44369×10^{-6}	1.18541×10^{-6}	7.34092×10^{-7}	$--$	1.73603×10^{-6}

Table A.1: Parameters extracted from the experimental H_2 spectrum in the $v'' = 0$ and $v' = 1$ in the non-equilibrium discharge for the radial distances at $D = 0,\ 3,\ 6,\ 9,\ -3$ mm.

Transition line	Term values (cm^{-1})	$I(J)$ D = −6 mm	$I(J)$ D = −9 mm
$Q_0(0,0)$	2.1703×10^3	7.49572×10^{-5}	3.34868×10^{-5}
$Q_1(0,0)$	2.2887×10^3	1.64496×10^{-4}	2.27488×10^{-4}
$Q_2(0,0)$	2.5245×10^3	6.79339×10^{-5}	8.70499×10^{-5}
$Q_3(0,0)$	2.8754×10^3	1.02586×10^{-4}	7.02798×10^{-5}
$Q_4(0,0)$	3.3379×10^3	1.71291×10^{-5}	8.48521×10^{-6}
$Q_5(0,0)$	3.9075×10^3	1.71737×10^{-5}	8.32543×10^{-6}
$Q_6(0,0)$	4.5787×10^3	7.02495×10^{-7}	$--$
$Q_7(0,0)$	5.3446×10^3	3.2467×10^{-7}	$--$
$Q_0(1,1)$	6.3288×10^3	7.00436×10^{-6}	2.15295×10^{-6}
$Q_1(1,1)$	6.4412×10^3	3.05075×10^{-5}	1.67757×10^{-5}
$Q_2(1,1)$	6.6647×10^3	1.00558×10^{-5}	5.55046×10^{-6}
$Q_3(1,1)$	6.9972×10^3	1.73607×10^{-5}	9.54336×10^{-6}
$Q_4(1,1)$	7.4352×10^3	2.74872×10^{-6}	1.13495×10^{-6}
$Q_5(1,1)$	7.9742×10^3	1.86449×10^{-6}	$--$

Table A.2: Parameters extracted from the experimental H_2 spectrum in the $v'' = 0$ and $v' = 1$ in the non-equilibrium discharge for the radial distances at $D = -6$ and -9 mm.

A.2 Data for radial vibrational temperatures of H_2

Transition line	$I(J)$ D = 0 mm	$I(J)$ D = 3 mm	$I(J)$ D = 6 mm	$I(J)$ D = 9 mm	$I(J)$ D = −3 mm	$I(J)$ D = −6 mm	$I(J)$ D = −9 mm
$Q_0(0,0)$	5.43846×10^{-5}	5.78772×10^{-5}	3.05592×10^{-5}	1.93639×10^{-5}	3.15292×10^{-5}	7.32498×10^{-5}	3.40719×10^{-5}
$Q_1(0,0)$	2.71255×10^{-4}	3.71876×10^{-4}	1.17500×10^{-4}	7.76238×10^{-5}	2.63238×10^{-4}	1.66186×10^{-4}	2.28421×10^{-4}
$Q_2(0,0)$	8.96319×10^{-5}	7.30333×10^{-5}	6.19614×10^{-5}	3.48580×10^{-5}	5.53052×10^{-5}	6.72079×10^{-5}	8.67691×10^{-5}
$Q_3(0,0)$	1.22847×10^{-4}	9.44852×10^{-5}	7.72339×10^{-5}	3.22702×10^{-5}	6.92115×10^{-5}	1.04458×10^{-4}	6.92807×10^{-5}
$Q_4(0,0)$	1.65338×10^{-5}	2.06479×10^{-5}	9.20639×10^{-6}	5.10310×10^{-6}	7.28842×10^{-6}	1.62596×10^{-5}	8.26290×10^{-6}
$Q_5(0,0)$	1.85283×10^{-5}	9.81522×10^{-6}	8.13454×10^{-6}	2.10360×10^{-6}	6.89080×10^{-6}	1.67760×10^{-5}	7.87351×10^{-6}
$Q_6(0,0)$	4.24053×10^{-7}	−−	−−	−−	6.71851×10^{-7}	5.26398×10^{-7}	−−
$Q_7(0,0)$	−−	−−	−−	−−	−−	3.20326×10^{-7}	−−
$Q_0(1,1)$	3.9800×10^{-6}	3.38742×10^{-6}	2.19373×10^{-6}	1.36693×10^{-6}	2.42254×10^{-6}	6.63228×10^{-6}	1.86478×10^{-6}
$Q_1(1,1)$	2.58239×10^{-5}	2.44453×10^{-5}	1.64416×10^{-5}	9.62557×10^{-6}	3.14929×10^{-5}	2.86870×10^{-5}	1.65000×10^{-5}
$Q_2(1,1)$	1.01344×10^{-5}	6.13173×10^{-6}	4.73668×10^{-6}	1.59925×10^{-6}	9.82794×10^{-6}	9.08667×10^{-6}	5.39545×10^{-6}
$Q_3(1,1)$	1.94378×10^{-5}	1.14209×10^{-5}	4.96411×10^{-6}	2.98346×10^{-6}	1.30135×10^{-5}	1.66569×10^{-5}	9.31727×10^{-6}
$Q_4(1,1)$	1.40526×10^{-6}	1.04552×10^{-6}	5.67570×10^{-7}	−−	1.83449×10^{-6}	2.50880×10^{-6}	1.00525×10^{-6}
$Q_5(1,1)$	2.26029×10^{-6}	9.89481×10^{-7}	6.72874×10^{-7}	−−	1.38252×10^{-6}	1.67193×10^{-6}	−−

Table A.3: The Gauss fit line intensity data at all measured radial distances in the $v'' = 0$ and $v' = 1$ in the non-equilibrium discharge for calculating the vibrational temperature of H_2 molecule.

A.3 Data for radial translational temperatures of H_2

		D = 0 mm			D = 3 mm			D = 6 mm		
Transition line	λ(nm)	$\Delta\lambda$(nm) Raw	$\Delta\lambda$(nm) Gauss fit	T_{trans}(K)	$\Delta\lambda$(nm) Raw	$\Delta\lambda$(nm) Gauss fit	T_{trans}(K)	$\Delta\lambda$(nm) Raw	$\Delta\lambda$(nm) Gauss fit	T_{trans}(K)
$Q_0(0,0)$	201.67	0.00899	0.00853	422 ± 46	0.00680	0.00707	230 ± 20	0.00697	0.00684	244 ± 10
$Q_1(0,0)$	201.78	0.00765	0.00782	298 ± 14	0.00864	0.00862	388 ± 2	0.00866	0.00844	389 ± 21
$Q_2(0,0)$	202.00	0.00832	0.00831	357 ± 1	0.00735	0.00711	273 ± 19	0.00737	0.00747	274 ± 8
$Q_3(0,0)$	202.33	0.00773	0.00769	303 ± 3	0.00787	0.00764	315 ± 20	0.00832	0.00818	355 ± 13
$Q_4(0,0)$	202.77	0.00756	0.00732	288 ± 20	0.00689	0.00702	235 ± 10	0.00654	0.00647	209 ± 5
$Q_5(0,0)$	203.32	0.00786	0.00799	311 ± 11	0.00673	0.00693	222 ± 15	0.00735	0.00710	267 ± 20
$Q_0(1,1)$	205.46	0.00794	0.00758	312 ± 30	0.00582	0.00556	158 ± 16	0.00649	0.00623	201 ± 18
$Q_1(1,1)$	205.57	0.00771	0.00784	292 ± 11	0.00657	0.00667	206 ± 7	0.00641	0.00638	195 ± 2
$Q_2(1,1)$	205.79	0.0073	0.00758	259 ± 22	0.00688	0.00700	227 ± 9	0.00602	0.00634	169 ± 20
$Q_3(1,1)$	206.12	0.00819	0.00806	331 ± 11	0.00769	0.00766	289 ± 2	0.00638	0.00643	192 ± 3
$Q_4(1,1)$	206.55	0.00721	0.00711	250 ± 8	0.00427	0.00445	77 ± 8	0.00545	0.00482	135 ± 35
$Q_5(1,1)$	207.09	0.00806	0.00812	317 ± 5	0.00688	0.00573	224 ± 86	0.00625	0.00659	182 ± 22

Table A.4: The linewith at FWHM data from the experimental spectrum at D = 0, 3 and 6 mm in the v'' = 0 and v' = 1 in the non-equilibrium discharge and corresponding radial translational temperatures of H_2.

	D = 9 mm			D = −3 mm			D = −6 mm		
Transition line	$\Delta\lambda$(nm) Raw	$\Delta\lambda$(nm) Gauss fit	T_{trans}(K)	$\Delta\lambda$(nm) Raw	$\Delta\lambda$(nm) Gauss fit	T_{trans}(K)	$\Delta\lambda$(nm) Raw	$\Delta\lambda$(nm) Gauss fit	T_{trans}(K)
$Q_0(0,0)$	0.00780	0.00725	311±48	0.00834	0.00824	360 ± 9	0.00886	0.00861	409±25
$Q_1(0,0)$	0.00810	0.00799	337±10	0.00942	0.00913	466±31	0.01200	0.01130	779±96
$Q_2(0,0)$	0.00777	0.00758	308±16	0.01089	0.01050	633±48	0.00903	0.00895	425 ± 8
$Q_3(0,0)$	0.00717	0.00713	257 ± 3	0.01034	0.01035	566 ± 1	0.00903	0.00864	423±39
$Q_4(0,0)$	0.00653	0.00626	209±19	0.00726	0.00704	263±17	0.00785	0.00805	312±17
$Q_5(0,0)$	0.00632	0.00573	193±40	0.00769	0.00780	297 ± 9	0.00820	0.00821	341 ± 1
$Q_6(0,0)$	−−	−−	−−	0.00707	0.00685	246±17	0.00762	0.00651	289±91
$Q_7(0,0)$	−−	−−	−−	−−	−−	−−	0.00608	0.00603	175 ± 3
$Q_0(1,1)$	0.00536	0.00499	131±20	0.00686	0.00729	227±31	0.00780	0.00809	300±24
$Q_1(1,1)$	0.00656	0.00670	205±10	0.00950	0.00952	457±21	0.00816	0.00841	330±22
$Q_2(1,1)$	0.00459	0.00439	92 ± 9	0.00796	0.00821	312±21	0.00771	0.00769	291 ± 2
$Q_3(1,1)$	0.00627	0.00567	184±39	0.00879	0.00870	385 ± 9	0.00831	0.00839	342 ± 7
$Q_4(1,1)$	−−	−−	−−	0.00891	0.00862	395±28	0.00802	0.00857	315±47
$Q_5(1,1)$	−−	−−	−−	0.00840	0.00835	346 ± 4	0.00792	0.00765	305±23

Table A.5: The linewith at FWHM data from the experimental spectrum at D = 9, −3 and −6 mm in the v'' = 0 and v' = 1 in the non-equilibrium discharge and corresponding radial translational temperatures of H_2.

	D = −9 mm		
Transition line	$\Delta\lambda$(nm) Raw	$\Delta\lambda$(nm) Gauss fit	T_{trans}(K)
$Q_0(0,0)$	0.00736	0.00701	274±28
$Q_1(0,0)$	0.00763	0.00744	269±16
$Q_2(0,0)$	0.00725	0.00729	264 ± 3
$Q_3(0,0)$	0.00678	0.00670	228 ± 6
$Q_4(0,0)$	0.00574	0.00585	157 ± 7
$Q_5(0,0)$	0.00765	0.00721	293±37
$Q_0(1,1)$	0.00610	0.00520	175±57
$Q_1(1,1)$	0.00685	0.00657	226±20
$Q_2(1,1)$	0.00642	0.00639	195 ± 2
$Q_3(1,1)$	0.00659	0.00646	206 ± 9
$Q_4(1,1)$	0.00621	0.00570	180±33

Table A.6: The linewith at FWHM data from the experimental spectrum at D = −9 mm in the v'' = 0 and v' = 1 in the non-equilibrium discharge and corresponding radial translational temperatures of H_2.

Appendix B

Laser wavelengths for the H_2 $(2 + 1)$ REMPI process

Transition line	Laser wavelength (nm)
$Q_0(2,2)$	209.4368
$Q_1(2,2)$	209.5466
$Q_2(2,2)$	209.7653
$Q_3(2,2)$	210.0908
$Q_4(2,2)$	210.5204
$Q_5(2,2)$	211.0502
$Q_6(2,2)$	211.6751

Table B.1: Table displays H_2 Q-branch laser wavelengths for $(2 + 1)$ REMPI process at v' = 2.

Transition line	Laser wavelength (nm)
$S_0(0,0)$	201.2808
$S_1(0,0)$	201.1397
$S_2(0,0)$	201.1143
$S_3(0,0)$	201.2044
$S_4(0,0)$	201.4090
$S_5(0,0)$	201.7263
$S_6(0,0)$	202.1535
$S_7(0,0)$	202.6872
$S_8(0,0)$	203.3228
$S_9(0,0)$	204.0548
$S_0(1,1)$	205.0817
$S_1(1,1)$	204.9453
$S_2(1,1)$	204.9237
$S_3(1,1)$	205.0169
$S_4(1,1)$	205.2237
$S_5(1,1)$	205.5421
$S_6(1,1)$	205.9694
$S_7(1,1)$	206.5018
$S_8(1,1)$	207.1345
$S_9(1,1)$	207.8617

Table B.2: Table displays H_2 S-branch laser wavelengths for $(2+1)$ REMPI process at v'' = 0 and v' = 1.

Transition line	Laser wavelength (nm)
$O_0(0,0)$	201.5371
$O_1(0,0)$	201.9072
$O_2(0,0)$	202.3890
$O_3(0,0)$	202.9793
$O_4(0,0)$	203.6742
$O_5(0,0)$	204.4686
$O_6(0,0)$	205.3563
$O_7(0,0)$	206.3299
$O_8(0,0)$	207.3807
$O_9(0,0)$	208.4983
$O_0(1,1)$	205.3324
$O_1(1,1)$	205.6960
$O_2(1,1)$	206.1700
$O_3(1,1)$	206.7511
$O_4(1,1)$	207.4350
$O_5(1,1)$	208.2163
$O_6(1,1)$	209.0884
$O_7(1,1)$	210.0434
$O_8(1,1)$	211.0719
$O_9(1,1)$	212.1629

Table B.3: Table displays H_2 O-branch laser wavelengths for $(2+1)$ REMPI process at $v'' = 0$ and $v' = 1$.

Appendix C

Theory of CARS

A brief discussion of the basic theory behind CARS is presented here in order to explain the process. A more complete account of the theory could be found in the literature [135, 207–210]. Conversion of two laser beams into the anti-Stokes component at $\omega_{as} = 2\omega_p - \omega_s$ is a direct result of the nonlinear dielectric properties of materials. The efficiency of this process is considered for both plane wave and focused beam and also an expression is established that relates this efficiency to the normal Raman cross section [167].

Initially, a theoretical description of non-linear mixing will be given. The polarisation of a medium in an electric field may commonly be expressed as a power series:

$$\vec{P}(\omega) = \chi^{(i)}(\omega)\vec{E}(\omega) + \chi^{(2)}\vec{E}^2(\omega) + \chi^{(3)}\vec{E}^3(\omega) \tag{C.1}$$

where $\vec{P}$ is the macroscopic polarization vector, $\chi^{(i)}$ is the dielectric susceptibility tensor of rank $i + 1$ associated with the ith order of the electric field. The subscripts denoting the tensor properties of the susceptibility have been eradicated for simplicity. At low intensity fields, only the first order terms become significant and is the elementary for classical, linear optics including normal Raman scattering. The higher order terms become significant as the field strength approach very high levels, a fact that explains why the entire field of nonlinear optics accom-

plished exponential progression immediately following the advent of laser. The first nonlinear term depends on the square of the field strength and is accountable for second harmonic generation (doubling of laser frequencies), sum and difference frequency generation, hyper-Raman effect and parametric oscillation. The third term is responsible for third harmonic generation $(3\omega_1 \rightarrow \omega_3)$ and other processes, e. g. $2\omega_1 + \omega_2 \rightarrow \omega_3$, $2\omega_1 - \omega_2 \rightarrow \omega_3$ etc. It is the last mentioned process, explicitly, $2\omega_1 - \omega_2 \rightarrow \omega_3$ which is designated as CARS. An isotropic medium such as a liquid or gas exhibits inversion symmetry in its macroscopic dielectric properties. Inspection of equation C.1 under the inversion operation discloses that $\chi^{(2)}$ must be identically equal to zero for such a medium. Therefore, the lowest order nonlinearity which may be present in a liquid or gas is due to the third-order susceptibility, $\chi^{(3)}$.

We will assume that the direction of all electric fields involved are along the same axis and treat each field as scalar quantity. Employing complex notation, we may express the magnitude of the electric field at angular frequency $\omega_i (= \frac{2\pi c}{\lambda_i})$ as:

$$E_i(\omega_i) = \frac{1}{2}\left[\varepsilon_i e^{\mathrm{i}(k_i z - \omega_i t)} + \text{c.c.}\right] \tag{C.2}$$

where ε_i is the amplitude, k_i is the momentum vector equal to $\frac{(\omega_i n_i)}{c}$, t is time, z is distance along the direction of propagation, n_i is the index of refraction at ε_i and c.c. is the complex conjugate. Generally, E may consists of a sum of a number of different frequencies. For the process designated as CARS, merely two frequencies at ω_1 and ω_2 are introduced, and resulting polarization at frequency $2\omega_1 - \omega_2$ will be examined. Conventions vary in the literature concerning the introduction of a factor of 3. If $E = E_1 + E_2$, the third-order term in equation C.1 has a component of magnitude $3E_1^2 E_2$. It is important to note that this factor of 3 is the source of some confusion when relating results from various articles. For clarity, the relationships derived here explicitly express this factor of 3 as a multiplicative coefficient related to the value for susceptibility. Hence, retaining merely those terms in which the polarization differs

by $\omega_3 = 2\omega_1 - \omega_2$,

$$\mathbf{P}^{(3)} = \frac{1}{8}\left[3\chi^{(3)}(-\omega_3, \omega_1, \omega_1, -\omega_2)\right]\left\{\varepsilon_1^2\varepsilon_2^* e^{\mathrm{i}[2k_1 - k_2]z - (2\omega_1 - \omega_2)t} + \text{c.c.}\right\} \tag{C.3}$$

where the usual notation of Bloembergen [211] is used such that $\chi^{(3)}(-\omega_\mathrm{a}, \omega_\mathrm{b}, \omega_\mathrm{c}, \omega_\mathrm{d})$ denotes the susceptibility for the process in which $\omega_\mathrm{a} = \omega_\mathrm{b} + \omega_\mathrm{c} + \omega_\mathrm{d}$.

Substituting the equation C.3 into Maxwells equations gives the gain equation for plane waves [165, 212];

$$d\varepsilon_\mathrm{as} = \frac{-\mathrm{i}\pi\omega_\mathrm{as}}{2cn_\mathrm{as}}\varepsilon_\mathrm{p}^2\varepsilon_\mathrm{s}^*\left(3\chi^{(3)}\right)e^{\mathrm{i}[2k_\mathrm{p} - k_\mathrm{s} - k_\mathrm{as}]Z}dZ \tag{C.4}$$

where the previous subscripts 1, 2, and 3 are exchanged by "p", "s" and "as" to indicate the pump laser frequency, Stokes frequency, and the anti-Stokes frequency, respectively. Introducing the standard relationship between electric field and intensity $\left[I_i = \frac{c}{8\pi} \mid \varepsilon_i \mid^2\right]$, combination of the equation C.4 gives:

$$\epsilon = \frac{I_\mathrm{as}}{I_\mathrm{s}} = \frac{P_\mathrm{as}}{P_\mathrm{s}} = \left(\frac{4\pi^2\omega_\mathrm{as}}{n_\mathrm{as}c^2}\right)^2 \mid 3\chi^{(3)} \mid^2 I_\mathrm{p}^2 L^2 \left[\frac{\sin\left(\frac{\Delta kL}{2}\right)}{\frac{\Delta kL}{2}}\right]^2 \tag{C.5}$$

where ϵ the efficiency of the process, P is the power of the respective beams, L is the length over which the beams are mixed through the sample and $\Delta k = 2k_\mathrm{p} - k_\mathrm{s} - k_\mathrm{as}$. The momentum mismatch Δk is a direct result of the fact that the propagating waves move in and out of phase due to dispersion in the medium. As can be realised from the equation C.5, conversion efficiency for a length of path L is much greater for $\Delta k = 0$, the phase-matched condition. As dispersion in gases is generally quite small, especially for low-pressure conditions, phase matching over modest path lengths (many centimetres) is readily accomplished. For condanced media, $\Delta k \neq 0$ even over small paths. In this case, phase matching is achieved, nevertheless, if the beams are overlapped at angle θ, the phase matching angle. This angle is determined from the geometry showed in figure C.1. It could be noted that when this is done, the CARS beam

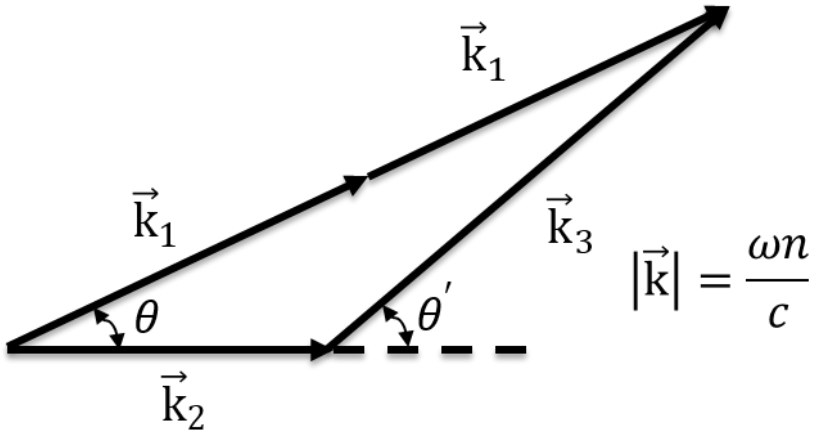

$$\omega_3 = 2\omega_1 - \omega_2$$

Figure C.1: Wave vector diagram for phase matching ($\Delta k = 0$). $\vec{k}_1$, $\vec{k}_2$, and $\vec{k}_3$ are the wave vectors for the pump, the Stokes, and anti-Stokes photons respectively.

occurs at a second angle θ', which aids in spatial filtering. It is clear that if the beams are overlapped, the interaction length is now limited by the beam walk-off. The phase matching angle, θ, is usually very small ($\sim 1^\circ$ for benzene at 992 cm^{-1}) but increases rapidly with Raman shift or for conditions near electronic absorption as encountered in resonance CARS enhancement.

If the beams are not overlapped and $\Delta k \neq 0$, then according to the equation C.5, the CARS signal will vary sinusoidally with path length. In order to have path length to reach maximum conversion efficiency we define as coherence length, $L = L_c$ which occurs when $\frac{\Delta k L_c}{2} = \frac{\pi}{2}$ or $\Delta k = \frac{\pi}{L_c}$. Hence, conversion efficiency varies with path length for collinear beams and coherence length.

We can consider the question of the impacts of focusing on conversion efficiency. In one approximation [213] the focal region is assumed to be a cylinder of plane waves and because of the fortuitous cancellation of terms, the subsequent expression $(\Delta k = 0)$ for the efficiency

is independent of focal length:

$$\epsilon = \left(\frac{2}{\lambda_{\mathrm{p}}}\right)^2 \left(\frac{4\pi^2\omega_{\mathrm{as}}}{n_{\mathrm{as}}c^2}\right)^2 \mid 3\chi^{(3)} \mid^2 P_{\mathrm{p}}^2 \tag{C.6}$$

in another approach to the problem, one adopts a functional form for the beam area but maintains the plane wave approximation for the field. The beam diameter $d(z)$ can then be stated as usual Gaussian form:

$$d(z)^2 = d_0^2\left(1 + \left(\frac{4\lambda z}{\pi d_0^2}\right)^2\right) \tag{C.7}$$

where z is the longitudinal distance from the focal point and d_0 is the minimum diameter of the beam waist. For a lens of focal length f and an unfocused beam diameter d and wavelength λ, it can be expressed [214] as:

$$d_0 = \frac{4\lambda f}{\pi d} \tag{C.8}$$

The beam diameter defined here denotes the $\frac{1}{e}$ value of electric field or $\frac{1}{e^2}$ value of the intensity. If the intensity is assumed to be constant in a beam profile of diameter $d(z)$, an approximate solution to the equation C.4 may be attained for the conversion efficiency:

$$\epsilon = \frac{P_{\mathrm{as}}}{P_{\mathrm{s}}} \approx \left[\frac{2\tan^{-1}\left(\frac{2L\lambda}{\pi d_0^2}\right)}{\lambda n_{\mathrm{as}}}\right]^2 \left(\frac{4\pi^2\omega_{\mathrm{as}}}{c^2}\right)^2 \mid 3\chi^{(3)} \mid^2 P_{\mathrm{p}}^2 \tag{C.9}$$

where λ is some average wavelength taken to be λ_{p}. This relation indicates that 71% of the maximum conversion takes place over length L equal to $\frac{2\pi d_0^2}{\lambda}$. Implicit assumption in this derivation is the plane wave approximation and a beam at ω_{as} which has the same spatial distribution as that of the beams at ω_{p} and ω_{s}.

Lastly, the magnitude of $\chi^{(3)}$ will be briefly discussed. The effect of an intense field on matter is to polarize it in nonlinear fashion. The magnitude if the third-order nonlinear susceptibility given in the equation C.1 is a measure of the conversion efficiency of the process

$\omega_{as} = 2\omega_p - \omega_s$. This conversion of laser power into anti-Stokes radiation occurs in any medium, including noble gases. Nevertheless, when there is a vibrational resonance present, the conversion efficiency increases dramatically when $\omega_v = \omega_p - \omega_s$. In this case, the total susceptibility is a total of a frequency-dependent resonant part and a nearly frequency-independent nonresonant part:

$$\chi^{(3)} \equiv \chi = \chi^{res} + \chi^{NR} \tag{C.10}$$

where for simplicity the superscript 3 has been removed, and throughout the text we are concerned with the third-order susceptibility related to the process $\omega_{as} = 2\omega_p - \omega_s$. It is to be noted that when χ^{res} is comparatively small because there is no nearby resonances or if the number density of resonant species is very small, then the CARS emission is dictated by the nonresonant susceptibility, which generally arises from the solvent or diluted gases. It is due to this nonresonant term χ^{NR}, which restricts the sensitivity of the technique, since one can record Raman spectra merely to an extent χ^{res} surpasses χ^{NR}. For now, nevertheless, we will demonstrate how χ^{res} is associated with spectral properties of Raman transitions.

Expressions for the resonant part of χ could be derived from classical or quantum mechanical approaches. The outcomes let χ to be stated in terms of the normal Raman cross section. Moreover, the numerous resonances present in χ are explicitly expressed in the quantum mechanical results. The harmonic oscillator aids as a model for the classical approach. Placzek's development [215] relates the polarizability, α, of a molecule to a bond stretching coordinate, q:

$$\alpha = \alpha_0 + \left(\frac{\partial \alpha}{\partial q}\right)_0 q + \ldots \tag{C.11}$$

The force created on the oscillator by a field because of this polarizability is:

$$F = \frac{1}{2}\left(\frac{\partial \alpha}{\partial q}\right)_0 E^2 \tag{C.12}$$

The equation of motion for the simple damped harmonic oscillator is thus [216]:

$$\ddot{q} + \Gamma\dot{q} + \omega_v^2 q = \frac{1}{2m}\left(\frac{\partial\alpha}{\partial q}\right)_0 E^2 \tag{C.13}$$

where Γ is a damping constant and ω_v the resonant frequency. By applying the field $E = E_{\mathrm{p}}+E_{\mathrm{s}}$, where E_i has the form given in the equation C.2, it is noted that q is determined not only at ω_{p} and ω_{s} but also at $\omega_{\mathrm{p}} - \omega_{\mathrm{s}}$. The solution of the equation C.13 for $q(\omega_{\mathrm{p}} - \omega_{\mathrm{s}})$ gives rise to a polarization at the anti-Stokes frequency due to the relation: $P = \chi E = N\left(\frac{\partial\alpha}{\partial q}\right)_0 q(\omega_{\mathrm{p}} - \omega_{\mathrm{s}})E_{\mathrm{p}}$, where N is the molecular number density. A direct comparison of these expressions then produces the following relation for the susceptibility [217]:

$$3\chi^{(3)}(\omega_{\mathrm{as}}) = \frac{N}{m}\left(\frac{\partial\alpha}{\partial q}\right)_0^2 \frac{\Delta_j}{\omega_v^2 - (\omega_{\mathrm{p}} - \omega_{\mathrm{s}})^2 - \mathrm{i}\Gamma(\omega_{\mathrm{p}} - \omega_{\mathrm{s}})} \tag{C.14}$$

where $N\Delta_j$, the difference in population in the lower and upper states for a specific transition j. The term, Δ_j, is an integral part of quantum mechanical approach by density matrix methods [218].

Electromagnetic scattering theory gives the differential scattering cross section, $\frac{d\sigma}{d\Omega}$, of a molecule exposed to electromagnetic radiation [219, 220]:

$$\frac{d\sigma}{d\Omega} = (\alpha')^2\left(\frac{\omega}{c}\right)^4 \tag{C.15}$$

where, for Raman Stokes frequency:

$$(\alpha')^2 = \left(\frac{\partial\alpha}{\partial q}\right)^2 < q^2 > \tag{C.16}$$

This relation ignores contributions to $\frac{d\sigma}{d\Omega}$ from anisotropic scattering, for which a 5 to 10% correction can be included when desired [219].

The quantum mechanical expression of $< q^2 >$ for a harmonic oscillator is:

$$< q^2 >= \frac{\hbar}{2m\omega_v} \tag{C.17}$$

By combining the three previous expressions, we obtain:

$$\frac{d\sigma}{d\Omega} = \frac{\hbar}{2m\omega_v}\left(\frac{\partial\alpha}{\partial q}\right)^2 \frac{\omega^4}{c^4} \tag{C.18}$$

The polarizability derivative in this expression can be substituted into the equation C.14 to attain $\chi^{(3)}$ in terms of the normal Raman differential cross section:

$$3\chi^{(3)} = \frac{2Nc^4}{\hbar\omega_{\mathrm{s}}^4}\left(\frac{d\sigma}{d\Omega}\right)\frac{\omega_v\Delta_j}{(\omega_v^2 - (\omega_{\mathrm{p}} - \omega_{\mathrm{s}})^2 - \mathrm{i}\Gamma(\omega_{\mathrm{p}} - \omega_{\mathrm{s}})} \tag{C.19}$$

Note that the resonant third-order susceptibility is a complex quantity which can be divided into a real and an imaginary part. These characteristics, the added nonresonant contribution, and the the squared dependence of susceptibility on CARS signal create uncommon spectral properties compared with normal, spontaneous Raman effect.

If we define $\Delta\omega \equiv \omega_v - (\omega_{\mathrm{p}} - \omega_{\mathrm{s}})$ and assume that $\frac{\Delta\omega}{\omega_v} \ll 1$, which is generally a very valid approximation in the vicinity of a resonance, then the equation C.19 simplifies to:

$$3\chi^{(3)} = A\left[\frac{1}{2\Delta\omega - \mathrm{i}\Gamma}\right]$$

where

$$A = \frac{2Nc^4}{\hbar\omega_s^4}\left(\frac{d\sigma}{d\Omega}\right)\Delta_j \tag{C.20}$$

According to the equations C.5, C.6 and C.9, the CARS signal or efficiency is proportional to the square of modulus of $\chi^{(3)}$ or:

$$|\,3\chi^{(3)}\,|^2 = \frac{A^2}{4\Delta\omega^2 + \Gamma^2} \tag{C.21}$$

For the integrated area over the CARS band, the equation C.21 becomes

$$\int |\,3\chi^{(3)}\,|^2\, d(\Delta\omega) = \frac{\pi A^2}{2\Gamma} \tag{C.22}$$

While at the peak of emission $(\Delta\omega = 0)$, the relation becomes:

$$|\,3\chi^{(3)}\,|^2_{(\Delta\omega=0)} = \frac{A^2}{\Gamma^2} \tag{C.23}$$

In an alternative approach, one derives an expression for $\chi^{(3)}$ from quantum mechanical considerations. Armstrong et al. [208], Maker and Terhune [150] obtain expressions deploying a third-order perturbation development. DeWitt et al. [218] have derived relations for the third-order susceptibility by the density matrix method. From all of these developments, it is clear that there are resonant denominators which express that $\chi^{(3)}$ is enhanced as the anti-Stokes signal or the laser frequency spectrally approaches an electronic resonance. Such an effect is analogous to resonance Raman Effect in orthodox Raman spectroscopy [154, 220].

To conclude, the comparison of CARS with normal Raman scattering will be briefly discussed. As mentioned earlier, CARS is associated with the normal Raman cross section and, thus, all molecular vibrations that are active in normal Raman spectroscopy are CARS active [167]. However there are a few differences between CARS and normal Raman spectroscopy. One of these differences is the efficiency of them. By combining the equation C.23 for peak CARS conversion with the equation C.9 for CARS efficiency (with long paths and focused beams), we obtain anti-Stokes power of [167]:

$$P_{\text{as}} = \left(\frac{16\pi\lambda_{\text{s}}^4}{hc\lambda_{\text{p}}\lambda_{\text{as}}}\right)^2 \left[\frac{N\Delta_j}{\Gamma}\left(\frac{d\sigma}{d\Omega}\right)\right]^2 P_{\text{p}}^2 P_{\text{s}} \tag{C.24}$$

where centimetre-gram-second units are used and Γ is full width at half-maximum in radians. For normal Raman emission the power scattered in the laser beam is:

$$P_{\text{Raman}} = NL\Omega\left(\frac{d\sigma}{d\Omega}\right) P_{\text{p}} \tag{C.25}$$

where, as previously, N is the number density, L is the length of the focal region, Ω is the solid angle collected, and $\left(\frac{d\sigma}{d\Omega}\right)$ is the differential Raman cross section. These equations indicate that CARS signals increases rapidly with laser power (cubic dependence on laser power), whereas normal Raman scattering increases linearly with laser power. It is also indicated by these equations that CARS output increases rapidly with number density (square dependence on number density), an effect which can be counterbraced with increased laser power to the point of saturation.

References

[1] G. Scoles, D. Bassi, U. Buck, and U. Valbusa. *Atomic and molecular beam methods*, volume 1 and 2. Oxford University Press New York, 1988.

[2] S. Y. T. Van De Meerakker, H. L. Bethlem, and G. Meijer. Taming molecular beams. *Nature Physics*, 4(8):595–602, 2008.

[3] S. D. Hogan, C. Seiler, and F. Merkt. Rydberg-state-enabled deceleration and trapping of cold molecules. *Physical review letters*, 103(12):123001, 2009.

[4] N. Vanhaecke, U. Meier, M. Andrist, B. H. Meier, and F. Merkt. Multistage zeeman deceleration of hydrogen atoms. *Physical Review-Series A-*, 75(3):031402, 2007.

[5] J. V. Prodan, W. D. Phillips, and H. Metcalf. Laser production of a very slow monoenergetic atomic beam. *Phys. Rev. Lett.*, 49:1149–1153, Oct 1982.

[6] R. Fulton, A. I. Bishop, M. N. Shneider, and P. F. Barker. Controlling the motion of cold molecules with deep periodic optical potentials. *Nature Physics*, 2(7):465–468, 2006.

[7] M. Gupta and D. Herschbach. A mechanical means to produce intense beams of slow molecules. *The Journal of Physical Chemistry A*, 103(50):10670–10673, 1999.

[8] M. Gupta and D. Herschbach. Slowing and speeding molecular beams by means of a rapidly rotating source. *The Journal of Physical Chemistry A*, 105(9):1626–1637, 2001.

[9] M. Qiu, Z. Ren, L. Che, D. Dai, S. A. Harich, X. Wang, X. Yang, C. Xu, D. Xie, M. Gustafsson, et al. Observation of feshbach resonances in the f+ h2 hf+ h reaction. *Science*, 311(5766):1440–1443, 2006.

[10] J. J. Gilijamse, S. Hoekstra, S. Y. T. van de Meerakker, G. C. Groenenboom, and G. Meijer. Near-threshold inelastic collisions using molecular beams with a tunable velocity. *Science*, 313(5793):1617–1620, 2006.

[11] K. S. Johnson, J. H. Thywissen, N. H. Dekker, K. K. Berggren, A. P. Chu, R. Younkin, and M. Prentiss. Localization of metastable atom beams with optical standing waves: nanolithography at the heisenberg limit. *Science*, 280(5369):1583–1586, 1998.

[12] D. Meschede. Atomic nanofabrication: perspectives for serial and parallel deposition. *J. Phys.: Conf. Ser.*, 19:118–124, 2005.

[13] B. P. Anderson and M. A. Kasevich. Macroscopic quantum interference from atomic tunnel arrays. *Science*, 282(5394):1686–1689, 1998.

[14] R. V. Krems. Cold controlled chemistry. *Physical Chemistry Chemical Physics*, 10(28):4079–4092, 2008.

[15] R. Krems, B. Friedrich, and W. C. Stwalley. *Cold molecules: theory, experiment, applications*. CRC press, 2010.

[16] R. V. Krems. Molecules near absolute zero and external field control of atomic and molecular dynamics. *International Reviews in Physical Chemistry*, 24(1):99–118, 2005.

[17] B. J. Sussman, D. Townsend, M. Y. Ivanov, and A. Stolow. Dynamic stark control of photochemical processes. *Science*, 314(5797):278–281, 2006.

[18] T. Takekoshi, J. R. Yeh, and R. J. Knize. Quasi-electrostatic trap for neutral atoms. *Optics communications*, 114(5):421–424, 1995.

[19] A. I. Bishop, L. Wang, and P. F. Barker. Creating cold stationary molecular gases by optical stark deceleration. *New Journal of Physics*, 12(7):073028, 2010.

[20] P. Barker and M. Shneider. Slowing molecules by optical microlinear deceleration. *Physical Review A*, 66(6):4–7, December 2002.

[21] P. Barker and M. Shneider. Optical microlinear accelerator for molecules and atoms. *Physical Review A*, 64(3):1–9, August 2001.

[22] B. Friedrich and G. Meijer. Ultracold physics: Molecules riding waves. *Nature Physics*, 2(7):437–438, 2006.

[23] C. Maher-McWilliams, P. Douglas, and P. F. Barker. Laser-driven acceleration of neutral particles. *Nature Photonics*, 6(6):386–390, 2012.

[24] C. Maher-McWilliams. *Creation, trapping and manipulation of a cold argon gas*. PhD thesis, UCL (University College London), 2013.

[25] N. Coppendale, L. Wang, P. Douglas, and P. F. Barker. A high-energy, chirped laser system for optical stark deceleration. *Applied Physics B*, 104(3):569–576, 2011.

[26] A. Gerakis. *Controlling and probing molecular motion with optical lattices*. PhD thesis, UCL (University College London), 2014.

[27] D. A. V. Kliner and R. N. Zare. D+ h2 (v= 1, j= 1): rovibronic state to rovibronic state reaction dynamics. *The Journal of chemical physics*, 92(3):2107–2109, 1990.

[28] D. A. V. Kliner, D. E. Adelman, and R. N. Zare. Comparison of experimental and theoretical integral cross sections for d+ h2 (v= 1, j= 1) hd (v= 1, j)+ h. *The Journal of chemical physics*, 95(3):1648–1662, 1991.

[29] N. C-M. Bartlett, J. Jankunas, and R. N. Zare. False estimates of stimulated raman pumping efficiency caused by the optical stark effect. *The Journal of chemical physics*, 134(23):234310, 2011.

[30] J. A. Shirley and R. J. Hall. Vibrational excitation in h2 and d2 electric discharges. *The Journal of Chemical Physics*, 67(6):2419–2421, 1977.

[31] V. A. Shakhatov, O. De Pascale, M. Capitelli, K. Hassouni, G. Lombardi, and A. Gicquel. Measurement of vibrational, gas, and rotational temperatures of h {sub 2}(x {sup 1}{sigma}{sub g}{sup+}) in radio frequency inductive discharge plasma by multiplex coherent anti-stokes raman scattering spectroscopy technique. *Physics of plasmas*, 12(2), 2005.

[32] G. L. Majstorović. Spectroscopic study of hydrogen rotational, vibrational and translational temperatures in a hollow cathode glow discharge. In *Journal of Physics: Conference Series*, volume 133, page 012022. IOP Publishing, 2008.

[33] I. Méndez, F. J. Gordillo-Vázquez, V. J. Herrero, and I. Tanarro. Atom and ion chemistry in low pressure hydrogen dc plasmas. *The Journal of Physical Chemistry A*, 110(18):6060–6066, 2006.

[34] D. B. Graves and D. Humbird. Surface chemistry associated with plasma etching processes. *Applied surface science*, 192(1):72–87, 2002.

[35] T. Nakano. Some recent topics of non-equilibrium discharge plasma technologies-their

widespread use from low pressure to atmospheric pressure. *Dielectrics and Electrical Insulation, IEEE Transactions on*, 14(5):1081–1087, 2007.

[36] A. Bogaerts, E. Neyts, R. Gijbels, and J. van der Mullen. Gas discharge plasmas and their applications. *Spectrochimica Acta Part B: Atomic Spectroscopy*, 57(4):609–658, 2002.

[37] J. Amorim, J. Loureiro, G. Baravian, and M. Touzeau. Experimental and theoretical study of dissociation in the positive column of a hydrogen glow discharge. *Journal of applied physics*, 82(6):2795–2804, 1997.

[38] I. Langmuir. Oscillations in ionized gases. *Proceedings of the National Academy of Sciences*, 14(8):627–637, 1928.

[39] L. Tonks and I. Langmuir. A general theory of the plasma of an arc. *Physical Review*, 34(6):876, 1929.

[40] T. L. Ferrell, T. A. Callcott, and R. J. Warmack. Plasmons and surfaces. *American Scientist*, 73:344–353, August 1985.

[41] R. A. Robinson and R. H. Stokes. *Electrolyte Solutions: The Measurement and Interpretation of Conductance, Chemical Potential and Diffusion in Solutions of Simple Electrolytes, by R. A. Robinson and R. H. Stokes*. Butterworths [1965, reprinted 1970], 1965.

[42] W. B. Kunkel. *Plasma Physics in Theory and Application*. New York: McGraw-Hill, 1966.

[43] J. J. Lowke and D. K. Davies. Properties of electric discharges sustained by a uniform source of ionization. *Journal of Applied Physics*, 48(12), 1977.

[44] D. B. Gurevich, M. A. Kanatenko, and I. V. Podmoshenskii. Breakdown formation in a photoionized nitrogen plasma. *Sov. J. Plasma Phys*, 5:760, 1979.

[45] N. W. Harris, F. O'Neill, and W. T. Whitney. Operation of a 15-atm electron-beam-controlled co2 laser. *Applied Physics Letters*, 25(3):148–151, 1974.

[46] E. P. Velikhov, S. A. Golubev, I. K. Zemtsov, A. F. Pal, I. G. Persiantsev, V. D. Pismennyi, and A. T. Rakhimov. Non-self-sustaining stationary gas discharge induced by electron-beam ionization in n2-co2 mixtures at atmospheric pressure. *Zhurnal Eksperimentalnoi i Teoreticheskoi Fiziki*, 65:543–549, 1973.

[47] F. Llewellyn-Jones. *The glow discharge: and an introduction to plasma physics*. Methuen New York, 1966.

[48] Y. P. Raizer, V. I. Kisin, and J. E. Allen. *Gas discharge physics*, volume 1. Springer-Verlag Berlin, 1991.

[49] J. R. Roth, J. Rahel, X. Dai, and D. M. Sherman. The physics and phenomenology of one atmosphere uniform glow discharge plasma (oaugdp) reactors for surface treatment applications. *Journal of Physics D: Applied Physics*, 38(4):555, 2005.

[50] E. Temmerman, Y. Akishev, N. Trushkin, C. Leys, and J. Verschuren. Surface modification with a remote atmospheric pressure plasma: dc glow discharge and surface streamer regime. *Journal of Physics D: Applied Physics*, 38(4):505, 2005.

[51] K. H. Becker, K. H. Schoenbach, and J. G. Eden. Microplasmas and applications. *Journal of Physics D: Applied Physics*, 39(3):R55, 2006.

[52] D. Dudek, N. Bibinov, J. Engemann, and P. Awakowicz. Direct current plasma jet needle source. *Journal of Physics D: Applied Physics*, 40(23):7367, 2007.

[53] F. Iza, Gon J. Kim, S. M. Lee, J. K. Lee, J. L. Walsh, Y. T. Zhang, and M. G. Kong. Microplasmas: Sources, particle kinetics, and biomedical applications. *Plasma Processes and Polymers*, 5(4):322–344, 2008.

[54] J. Tynan, V. J. Law, P. Ward, A. M. Hynes, J. Cullen, G. Byrne, S. Daniels, and D. P. Dowling. Comparison of pilot and industrial scale atmospheric pressure glow discharge systems including a novel electro-acoustic technique for process monitoring. *Plasma Sources Sci. Technol*, 19(015015):015015, 2010.

[55] B. R. Locke and K-Y. Shih. Review of the methods to form hydrogen peroxide in electrical discharge plasma with liquid water. *Plasma Sources Science and Technology*, 20(3):034006, 2011.

[56] E. E. Kunhardt. Generation of large-volume, atmospheric-pressure, nonequilibrium plasmas. *Plasma Science, IEEE Transactions on*, 28(1):189–200, 2000.

[57] A. Schutze, J. Y. Jeong, S. E. Babayan, J. Park, G. S. Selwyn, and R. F. Hicks. The atmospheric-pressure plasma jet: a review and comparison to other plasma sources. *Plasma Science, IEEE Transactions on*, 26(6):1685–1694, 1998.

[58] D. Staack, B. Farouk, A. Gutsol, and A. Fridman. Characterization of a dc atmospheric pressure normal glow discharge. *Plasma Sources Science and Technology*, 14(4):700, 2005.

[59] V. K. Mehta and R. Mehta. *Principle Of Elect. Engg. & Electronics (ME)*. S. Chand, 2006.

[60] M. E. Van Valkenburg. *Reference data for engineers: radio, electronics, computers and communications*. Newnes, 2001.

[61] Y. P. Raizer and J. E. Allen. *Gas discharge physics*, volume 2. Springer Berlin, 1997.

[62] M. Capitelli and C. Gorse. Plasma technology. 1992.

[63] M. Capitelli. Nonequilibrium vibrational kinetics. *Nonequilibrium Vibrational Kinetics. Series: Topics in Current Physics, ISBN: 978-3-642-48617-3. Springer Berlin Heidelberg (Berlin, Heidelberg), Edited by Mario Capitelli, vol. 39*, 39, 1986.

[64] M. Capitelli, C. M. Ferreira, B. F. Gordiets, A. I. Osipov, M. Capitelli, C. M. Ferreira, and B. F. Gordiets. *Plasma kinetics in atmospheric gases*, volume 99. Springer Berlin, 2000.

[65] W. Lochte-Holtgreven. *Plasma Diagnostics*. New York: American Elsevier, 1968.

[66] M. Pealat, J-P. E. Taran, M. Bacal, and F. Hillion. Rovibrational molecular populations, atoms, and negative ions in h2 and d2 magnetic multicusp discharges. *The Journal of chemical physics*, 82(11):4943–4953, 1985.

[67] W. Biel, M. Bröse, M. David, H. Kempkens, and J. Uhlenbusch. Determination of atomic and molecular particle densities and temperatures in a low-pressure hydrogen hollow cathode discharge. *Plasma physics and controlled fusion*, 39(5):661, 1997.

[68] H. N. Chu, E. A. Den Hartog, A. R. Lefkow, J. Jacobs, L. W. Anderson, M. G. Lagally, and J. E. Lawler. Measurements of the gas kinetic temperature in a ch 4-h 2 discharge during the growth of diamond. *Physical Review A*, 44(6):3796, 1991.

[69] A. Gicquel, K. Hassouni, Y. Breton, M. Chenevier, and J. C. Cubertafon. Gas temperature measurements by laser spectroscopic techniques and by optical emission spectroscopy. *Diamond and related materials*, 5(3):366–372, 1996.

[70] S. I. Gritsinin, I. A. Kossyi, N. I. Malykh, V. G. Ral'Chenko, K. F. Sergeichev, V. P. Silakov, I. A. Sychev, N. M. Tarasova, and A. V. Chebotarev. Determination of the gas temperature in high-pressure microwave discharges in hydrogen. *Journal of Physics D: Applied Physics*, 31(20):2942, 1998.

[71] T. Gans, V. Schulz-von der Gathen, and H. F. Döbele. Time dependence of rotational state populations of excited hydrogen molecules in an rf excited plasma reactor. *Plasma Sources Science and Technology*, 10(1):17, 2001.

[72] A. N. Goyette, W. B. Jameson, L. W. Anderson, and J. E. Lawler. An experimental comparison of rotational temperature and gas kinetic temperature in a discharge. *Journal of Physics D: Applied Physics*, 29(5):1197, 1996.

[73] G. L. Majstorović, N. M. Šišović, and N. Konjević. Rotational and vibrational temperatures of molecular hydrogen in a hollow cathode glow discharge. *Plasma Sources Science and Technology*, 16(4):750, 2007.

[74] R. Hippler, S. Pfau, M. Schmidt, and K. H. Schoenbach. Low temperature plasma physics: fundamental aspects and applications. *Low Temperature Plasma Physics: Fundamental Aspects and Applications, by Rainer Hippler (Editor), Sigismund Pfau (Editor), Martin Schmidt (Editor), Karl H. Schoenbach (Editor), pp. 530. ISBN 3-527-28887-2. Wiley-VCH, June 2001.*, 1, 2001.

[75] G. Herzberg. Molecular spectra and molecular structure. vol. 1: Spectra of diatomic molecules. *New York: Van Nostrand Reinhold, 1950, 2nd ed.*, 1, 1950.

[76] J. Röpcke, M. Käning, and B. P. Lavrov. Spectroscopical diagnostics of molecular microwave plasmas. *Le Journal de Physique IV*, 8(PR7):Pr7–207, 1998.

[77] C. Gorse, M. Capitelli, and A. Ricard. On the coupling of electron and vibrational energy distributions in h2, n2, and co post discharges. *The Journal of chemical physics*, 82(4):1900–1906, 1985.

[78] C. Gorse, M. Capitelli, M. Bacal, J. Bretagne, and A. Lagana. Progress in the non-equilibrium vibrational kinetics of hydrogen in magnetic multicusp h- ion sources. *Chemical physics*, 117(2):177–195, 1987.

[79] C. Gorse, R. Celiberto, M. Cacciatore, A. Lagana, and M. Capitelli. From dynamics to modeling of plasma complex systems: negative ion (h-) sources. *Chemical physics*, 161(1):211–227, 1992.

[80] K. Hassouni, A. Gicquel, M. Capitelli, and J. Loureiro. Chemical kinetics and energy transfer in moderate pressure h2 plasmas used in diamond mpacvd processes. *Plasma Sources Science and Technology*, 8(3):494, 1999.

[81] S. Longo and A. Milella. A one-dimensional, self-consistent model of charged particle transport and vibrational kinetics in weakly ionized hydrogen. *Chemical physics*, 274(2):219–229, 2001.

[82] T. G. Beuthe and J-S. Chang. Chemical kinetic modelling of non-equilibrium ar-h2 thermal plasmas. *Japanese journal of applied physics*, 38(7S):4576, 1999.

[83] G. M. Petrov and T. Petrova. Formation of negative hydrogen ions in a ne–h2 hollow cathode discharge. *Plasma chemistry and plasma processing*, 22(4):573–605, 2002.

[84] P. Berlemont, D. A. Skinner, and M. Bacal. Negative ion volume production model: State of the experimental confirmation. *Review of scientific instruments*, 64(10):2721–2728, 1993.

[85] M. Capitelli and J. N. Bardsley. *Nonequilibrium processes in partially ionized gases*. Plenum Pub Corp, 1990.

[86] C. Gorse, M. Capitelli, J. Bretagne, and M. Bacal. Vibrational excitation and negative-ion production in magnetic multicusp hydrogen discharges. *Chemical physics*, 93(1):1–12, 1985.

[87] N. P. Curran, M. B. Hopkins, D. Vender, and B. W. James. The effect of the addition of noble gases on h-production in a dc filament discharge in hydrogen. *Plasma Sources Science and Technology*, 9(2):169, 2000.

[88] J. L. Giuliani, V. A. Shamamian, R. E. Thomas, J. P. Apruzese, M. Mulbrandon, R. A. Rudder, R. C. Hendry, and A. E. Robson. Two-dimensional model of a large area, inductively coupled, rectangular plasma source for chemical vapor deposition. *Plasma Science, IEEE Transactions on*, 27(5):1317–1328, 1999.

[89] K. Hassouni, T. A. Grotjohn, and A. Gicquel. Self-consistent microwave field and plasma discharge simulations for a moderate pressure hydrogen discharge reactor. *Journal of Applied Physics*, 86(1):134–151, 1999.

[90] H. Rau. Monte carlo simulation of a microwave plasma in hydrogen. *Journal of Physics D: Applied Physics*, 33(24):3214, 2000.

[91] P. André, J. Aubreton, M-F. Elchinger, P. Fauchais, and A. Lefort. A new modified pseudoequilibrium calculation to determine the composition of hydrogen and nitrogen plasmas at atmospheric pressure. *Plasma Chemistry and Plasma Processing*, 21(1):83–105, 2001.

[92] A. Lacoste, L. L. Alves, C. M. Ferreira, and G. Gousset. Simulation of pulsed high-frequency breakdown in hydrogen. *Journal of Applied Physics*, 88(6):3170–3181, 2000.

[93] C-H. Yang, K. Itoh, H. Tomita, and M. Obara. Effects of penning reactions and excitation rate on the pulsed transverse-discharge neon laser for photodynamic therapy. *Journal of applied physics*, 78(1):30–38, 1995.

[94] G. M. Petrov. A theoretical and experimental study of a penning recombination laser operating in a hollow cathode discharge. *Journal of Physics D: Applied Physics*, 30(1):67, 1997.

[95] O. Fukumasa. Effects of the energy distribution of fast electrons on h2 vibrational excitation in a tandem negative ion source. *Journal of applied physics*, 71(7):3193–3196, 1992.

[96] J. Loureiro and C. M. Ferreira. Electron and vibrational kinetics in the hydrogen positive column. *Journal of Physics D: Applied Physics*, 22(11):1680, 1989.

[97] A. Garscadden and R. Nagpal. Non-equilibrium electronic and vibrational kinetics in h2-n2 and h2 discharges. *Plasma Sources Science and Technology*, 4(2):268, 1995.

[98] J. Loureiro and A. Ricard. Electron and vibrational kinetics in an n2-h2 glow discharge with application to surface processes. *Journal of Physics D: Applied Physics*, 26(2):163, 1993.

[99] R. Winkler, J. Wilhelm, S. I. Krasheninnikov, and V. V. Starykh. Impact of the vibrationally excited states on the macroscopic behaviour of the band-like electron beam discharge plasma in h/h2-mixture. *Annalen der Physik*, 494(3):216–232, 1982.

[100] M. Cacciatore. Gas-phase and gas-surface interactions of vibrationally excited hydrogen molecules. In *Nonequilibrium Processes in Partially Ionized Gases*, pages 485–497. Springer, 1990.

[101] S. J. Buckman and A. V. Phelps. Vibrational excitation of d2 by low energy electrons. *The Journal of chemical physics*, 82(11):4999–5011, 1985.

[102] H. Tawara, Y. Itikawa, H. Nishimura, and M. Yoshino. Cross sections and related data for electron collisions with hydrogen molecules and molecular ions. *Journal of Physical and Chemical Reference Data*, 19(3):617–636, 1990.

[103] C. Mündel, M. Berman, and W. Domcke. Nuclear dynamics in resonant electron-molecule scattering beyond the local approximation: Vibrational excitation and dissociative attachment in h 2 and d 2. *Physical Review A*, 32(1):181, 1985.

[104] A. U. Hazi. Impact-parameter method for electronic excitation of molecules by electron impact. *Physical Review A*, 23(5):2232, 1981.

[105] W. T. Miles, R. Thompson, and A. E. S. Green. Electron-impact cross sections and energy deposition in molecular hydrogen. *Journal of Applied Physics*, 43(2):678–686, 1972.

[106] J. R. Hiskes. Cross sections for the vibrational excitation of the h2 (x1+ g) state via electron collisional excitation of the higher singlet states. *Journal of Applied Physics*, 51(9):4592–4594, 1980.

[107] L. S. Frost and A. V. Phelps. Rotational excitation and momentum transfer cross sections for electrons in h 2 and n 2 from transport coefficients. *Physical Review*, 127(5):1621, 1962.

[108] B. H. Bransden and C. J. Joachain. *Physics of atoms and molecules*. Pearson Education India, 2003.

[109] M. Mizushima et al. *Theory of rotating diatomic molecules*. Wiley, 1975.

[110] H. Haken and H. C. Wolf. *Molecular physics and elements of quantum chemistry: introduction to experiments and theory*. Springer Science & Business Media, 2013.

[111] G. Buntkowsky, B. Walaszek, A. Adamczyk, Y. Xu, H-H. Limbach, and B. Chaudret. Mechanism of nuclear spin initiated para-h 2 to ortho-h 2 conversion. *Physical Chemistry Chemical Physics*, 8(16):1929–1935, 2006.

[112] J. T. Kummer. Ortho- and para-hydrogen conversion by metal surfaces 21 k. *The Journal of Physical Chemistry*, 66(9):1715–1719, 1962.

[113] G. E. Schmauch and A. H. Singleton. Technical aspects of ortho-parahydrogen conversion. *Industrial & Engineering Chemistry*, 56(5):20–31, 1964.

[114] M. Göppert-Mayer. Über elementarakte mit zwei quantensprüngen. *Annalen der Physik*, 401(3):273–294, 1931.

[115] M. N. R. Ashfold and J. D. Howe. Multiphoton spectroscopy of molecular species. *Annual Review of Physical Chemistry*, 45(1):57–82, 1994.

[116] M. N. R. Ashfold. Multiphoton probing of molecular rydberg states. *Molecular Physics*, 58(1):1–20, 1986.

[117] S. H. Lin. *Multiphoton spectroscopy of molecules*. Elsevier, 2012.

[118] H. Rottke and K. H. Welge. Singlet gerade rydberg states of molecular hydrogen. *The Journal of chemical physics*, 97(2):908–926, 1992.

[119] K-D. Rinnen, M. A. Buntine, D. A. V. Kliner, R. N. Zare, and W. M. Huo. Quantitative determination of h2, hd, and d2 internal-state distributions by (2+ 1) resonance-enhanced multiphoton ionization. *The Journal of chemical physics*, 95(1):214–225, 1991.

[120] A. Sur, C. V. Ramana, W. A. Chupka, and S. D. Colson. Rydberg–valence interactions in the πg states of o2. *The Journal of chemical physics*, 84(1):69–72, 1986.

[121] E. E. Marinero, C. T. Rettner, and R. N. Zare. H+ d2 reaction dynamics. determination of the product state distributions at a collision energy of 1.3 ev. *The Journal of chemical physics*, 80(9):4142–4156, 1984.

[122] T. N. Kitsopoulos, M. A. Buntine, D. P. Baldwin, R. N. Zare, and D. W. Chandler. Reaction product imaging: the h+ d2 reaction. *Science*, 260(5114):1605–1610, 1993.

[123] M. Balooch, M. J. Cardillo, D. R. Miller, and R. E. Stickney. Molecular beam study of the apparent activation barrier associated with adsorption and desorption of hydrogen on copper. *Surface Science*, 46(2):358 – 392, 1974.

[124] D. G. Truhlar and C. J. Horowitz. Functional representation of liu and siegbahns accurate abinitio potential energy calculations for h+h2. *The Journal of Chemical Physics*, 68(5), 1978.

[125] D. J. Rose and M. Clark. *Plasmas and controlled fusion*. 1961.

[126] T. E. Sharp. Potential-energy curves for molecular hydrogen and its ions. *Atomic Data and Nuclear Data Tables*, 2:119–169, 1970.

[127] M. J. Berry. Chloroethylene photochemical lasers: Vibrational energy content of the hcl molecular elimination products. *The Journal of Chemical Physics*, 61(8), 1974.

[128] R. N. Zare and P. J. Dagdigian. Tunable laser fluorescence method for product state analysis. *Science*, 185(4153):739–747, 1974.

[129] B. P. Stoicheff. High resolution raman spectroscopy of gases: Ix. spectra of h2, hd, and d2. *Canadian Journal of Physics*, 35(6):730–741, 1957.

[130] H. Mori and C. Dankert. Spectroscopy of h2 + n2mixture in rarefied flows. *AIP Conference Proceedings*, 663(1):170–177, 2003.

[131] D. J. Kligler and C. K. Rhodes. Observation of two-photon excitation of the h 2 e, f σ g+ 1 state. *Physical Review Letters*, 40(5):309, 1978.

[132] H. Zacharias. Laser spectroscopy of desorbing molecules. *Applied Physics A*, 47(1):37–54, 1988.

[133] V. Letokhov. *Laser photoionization spectroscopy*. Elsevier, 2012.

[134] R. W. Terhune and P. D. Maker. Nonlinear optics. *Bull. Am. Phys. Soc*, 8:359, 1963.

[135] W. Meier, H. Rottke, H. Zacharias, and K. H. Welge. Rotational state selective photoionization of the h2 molecule from b 1σ+ u (v= 0, 3) states. *The Journal of chemical physics*, 83(9):4360–4363, 1985.

[136] U. Fantz and D. Wünderlich. Franck–condon factors, transition probabilities, and radiative lifetimes for hydrogen molecules and their isotopomeres. *Atomic Data and Nuclear Data Tables*, 92(6):853–973, 2006.

[137] G. Pozgainer, L. Windholz, and A. Winkler. Rovibrational state-specific detection of desorbing hydrogen molecules using multiphoton ionization (rempi). *Measurement Science and Technology*, 5(8):947, 1994.

[138] W. Demtröder. *Laser spectroscopy: basic concepts and instrumentation*. Number 2674. Springer, 2003.

[139] V. S. Letokhov. *Laser analytical spectrochemistry*. CRC Press, 1986.

[140] K. P. Huber and G. Herzberg. Constants of diatomic molecules, molecular spectra and molecular structure vol. iv, 1979.

[141] J. M. Hollas. *Modern spectroscopy*. John Wiley & Sons, 2004.

[142] K. P. Huber and G. Herzberg. Constants of diatomic molecules (data prepared by jw gallagher and rd johnson, iii) in nist chemistry webbook, nist standard reference database number 69, eds. *PJ Linstrom and WG Mallard, July, National Institute of Standards and Technology, Gaithersburg MD, 20899, http://webbook.nist.gov, (retrieved March 10, 2014)*, 2001.

[143] E. E. Marinero, C. T. Rettner, and R. N. Zare. Quantum-state-specific detection of molecular hydrogen by three-photon ionization. *Phys. Rev. Lett.*, 48:1323–1326, 1982.

[144] R. G. Bray and R-M. Hochstrasser. Two-photon absorption by rotating diatomic molecules. *Molecular Physics*, 31(4):1199–1211, 1976.

[145] J. A. Smith. *Laser diagnostics of a diamond depositing chemical vapour deposition gas-phase environment*. PhD thesis, University of Bristol, 2002.

[146] G. Požgainer, K. D. Rendulic, and A. Winkler. Laser spectroscopy on hydrogen desorbing from nickel. *Surface science*, 307:344–349, 1994.

[147] D. J. Kligler, J. Bokor, and C. K. Rhodes. Collisional and radiative properties of the h 2 e, f σ g 1+ state. *Physical Review A*, 21(2):607, 1980.

[148] N. V. Vitanov, B. W. Shore, L. Yatsenko, K. Böhmer, T. Halfmann, T. Rickes, and K. Bergmann. Power broadening revisited: theory and experiment. *Optics communications*, 199(1):117–126, 2001.

[149] R. W. Terhune and P. D. Maker. Nonlinear optics. *Bull. Am. Phys. Soc*, 8:359, 1963.

[150] P. D. Maker and R. W. Terhune. Study of optical effects due to an induced polarization third order in the electric field strength. *Physical Review*, 137(3A):A801, 1965.

[151] A. Anderson (Ed.). *The Raman Effect*, volume 1 and 2. Dekker, New York, 1971.

[152] W. Kiefer and H. J. Bernstein. The resonance raman effect of the permanganate and chromate ions. *Molecular Physics*, 23(5):835–851, 1972.

[153] E. S. Yeung. Inverse raman effect: A quantitative spectroscopic technique. *Journal of Molecular Spectroscopy*, 53(3):379–392, 1974.

[154] J. F. Verdieck, S. H. Peterson, C. M. Savage, and P. D. Maker. Hyper-raman spectra of methane, ethane and ethylene in gas phase. *Chemical Physics Letters*, 7(2):219 – 222, 1970.

[155] D. Heiman, R. W. Hellwarth, M. D. Levenson, and G. Martin. Raman-induced kerr effect. *Physical Review Letters*, 36(4):189, 1976.

[156] A. M. Zheltikov. Coherent anti-stokes raman scattering: from proof-of-the-principle experiments to femtosecond cars and higher order wave-mixing generalizations. *Journal of Raman Spectroscopy*, 31(8-9):653–667, 2000.

[157] W. M. Tolles, J. W. Nibler, J. R. McDonald, and A. B. Harvey. A review of the theory and application of coherent anti-stokes raman spectroscopy (cars). *Applied Spectroscopy*, 31(4):253–271, 1977.

[158] G. L. Eesley. *Coherent Raman Spectroscopy*. Elsevier, 2013.

[159] A. C. Eckbreth. *Laser diagnostics for combustion temperature and species*, volume 3. CRC Press, 1996.

[160] A. B. Harvey and J. W. Nibler. Coherent anti-stokes raman spectroscopy of gases. *Applied Spectroscopy Reviews*, 14(1):101–143, 1978.

[161] S. A. J. Druet and J-P. E. Taran. Cars spectroscopy. *Progress in quantum Electronics*, 7(1):1–72, 1981.

[162] W. Kifer. Active raman spectroscopy: high resolution molecular spectroscopical methods. *Journal of Molecular Structure*, 59:305–319, 1980.

[163] R. F. Begley. Coherent anti-Stokes Raman spectroscopy. *Applied Physics Letters*, 25(7):387, 1974.

[164] V. N. Ochkin. *Spectroscopy of low temperature plasma*. John Wiley & Sons, 2009.

[165] P. R. Regnier, F. Moya, and J-P. E. Taran. Gas concentration measurement by coherent raman anti-stokes scattering. *AIAA Journal*, 12(6):826–831, 1974.

[166] A. C. Eckbreth. Boxcars: Crossed-beam phase-matched cars generation in gases. *Applied Physics Letters*, 32(7):421–423, 1978.

[167] W. M. Tolles, J. W. Nibler, J. R. McDonald, and A. B. Harvey. A review of the theory and application of coherent anti-stokes raman spectroscopy (cars). *Applied Spectroscopy*, 31(4):253–271, 1977.

[168] I. Dabrowski. The lyman and werner bands of h2. *Canadian Journal of Physics*, 62(12):1639–1664, 1984.

[169] J. Turner, K. Kirby-Docken, and A. Dalgarno. The quadrupole vibration-rotation transition probabilities of molecular hydrogen. *The Astrophysical Journal Supplement Series*, 35:281, 1977.

[170] N. C. M. Bartlett, D. J. Miller, R. N. Zare, D. Sofikitis, T. P. Rakitzis, and A. J. Alexander. Preparation of oriented and aligned h 2 and hd by stimulated raman pumping. *The Journal of chemical physics*, 129:084312, 2008.

[171] R. Fulton, A. I. Bishop, and P. F. Barker. Optical stark decelerator for molecules. *Physical review letters*, 93(24):243004, 2004.

[172] R. Fulton, A. I. Bishop, M. N. Shneider, and P. F. Barker. Controlling the motion of cold molecules with deep periodic optical potentials. *Nature Physics*, 2(7):465–468, 2006.

[173] P. F. Barker, S. M. Purcell, P. Douglas, P. Barletta, N. Coppendale, C. Maher-McWilliams, and J. Tennyson. Sympathetic cooling by collisions with ultracold rare gas atoms, and recent progress in optical stark deceleration. *Faraday discussions*, 142:175–190, 2009.

[174] P. D. Edmunds. *Trapping ultracold argon atoms*. PhD thesis, UCL (University College London), 2015.

[175] P. D. Edmunds and P. F. Barker. A deep optical cavity trap for atoms and molecules with rapid frequency and intensity modulation. *Review of Scientific Instruments*, 84(8):083101, 2013.

[176] P. D. Edmunds and P. F. Barker. Trapping cold ground state argon atoms. *Physical review letters*, 113(18):183001, 2014.

[177] J. van Veldhoven, J. Küpper, H. L. Bethlem, B. Sartakov, A. J. A. van Roij, and G. Meijer. Decelerated molecular beams for high-resolution spectroscopy. *The European Physical Journal D-Atomic, Molecular, Optical and Plasma Physics*, 31(2):337–349, 2004.

[178] J. J. Gilijamse, S. Hoekstra, S. A. Meek, M. Metsala, S. Y. T. van de Meerakker, G. Meijer, and G. C. Groenenboom. The radiative lifetime of metastable co ($a3\backslash$ pi, v= 0). $arXivpreprintarXiv : 0710.2240, 2007$.

[179] S. Y. T. van de Meerakker, N. Vanhaecke, M. P. J. van der Loo, G. C. Groenenboom, and G. Meijer. Direct measurement of the radiative lifetime of vibrationally excited oh radicals. *Physical review letters*, 95(1):013003, 2005.

[180] E. R. Hudson, H. J. Lewandowski, B. C. Sawyer, and J. Ye. Cold molecule spectroscopy for constraining the evolution of the fine structure constant. *Physical review letters*, 96(14):143004, 2006.

[181] M. Kajita, G. Gopakumar, M. Abe, and M. Hada. Accuracy estimations of overtone vibrational transition frequencies of optically trapped 174 yb 6 li molecules. *Physical Review A*, 85(6):062519, 2012.

[182] P. A. Bolokhov, M. Pospelov, and M. Romalis. Electric dipole moments as probes of c p t invariance. *Physical Review D*, 78(5):057702, 2008.

[183] J. Baron, W. C. Campbell, D. DeMille, J. M. Doyle, G. Gabrielse, Y. V. Gurevich, P. W. Hess, N. R. Hutzler, E. Kirilov, I. Kozyryev, et al. Order of magnitude smaller limit on the electric dipole moment of the electron. *Science*, 343(6168):269–272, 2014.

[184] J. M. Hutson. Ultracold chemistry. *Science.*, 327(5967):788–789, 2010.

[185] S. Ospelkaus, K-K. Ni, D. Wang, M. H. G. De Miranda, B. Neyenhuis, G. Quéméner, P. S. Julienne, J. L. Bohn, D. S. Jin, and J. Ye. Quantum-state controlled chemical reactions of ultracold potassium-rubidium molecules. *Science*, 327(5967):853–857, 2010.

[186] B. C. Sawyer, B. K. Stuhl, D. Wang, M. Yeo, and J. Ye. Molecular beam collisions with a magnetically trapped target. *Physical review letters*, 101(20):203203, 2008.

[187] S. Jochim, M. Bartenstein, A. Altmeyer, G. Hendl, S. Riedl, C. Chin, J. H. Denschlag, and R. Grimm. Bose-einstein condensation of molecules. *Science*, 302(5653):2101–2103, 2003.

[188] J. G. Danzl, E. Haller, M. Gustavsson, M. J. Mark, R. Hart, N. Bouloufa, O. Dulieu, H. Ritsch, and H-C. Nägerl. Quantum gas of deeply bound ground state molecules. *Science*, 321(5892):1062–1066, 2008.

[189] K-K. Ni, S. Ospelkaus, M. H. G. De Miranda, A. Pe'er, B. Neyenhuis, J. J. Zirbel, S. Kotochigova, P. S. Julienne, D. S. Jin, and J. Ye. A high phase-space-density gas of polar molecules. *science*, 322(5899):231–235, 2008.

[190] P. D. Lett, K. Helmerson, W. D. Phillips, L. P. Ratliff, S. L. Rolston, and M. E. Wagshul. Spectroscopy of na 2 by photoassociation of laser-cooled na. *Physical review letters*, 71(14):2200, 1993.

[191] A. N. Nikolov, J. R. Ensher, E. E. Eyler, H. Wang, W. C. Stwalley, and P. L. Gould. Efficient production of ground-state potassium molecules at sub-mk temperatures by two-step photoassociation. *Physical review letters*, 84(2):246, 2000.

[192] J. M. Sage, S. Sainis, T. Bergeman, and D. DeMille. Optical production of ultracold polar molecules. *Physical review letters*, 94(20):203001, 2005.

[193] J. Deiglmayr, A. Grochola, M. Repp, K. Mörtlbauer, C. Glück, J. Lange, O. Dulieu, R. Wester, and M. Weidemüller. Formation of ultracold polar molecules in the rovibrational ground state. *Physical review letters*, 101(13):133004, 2008.

[194] S. Y. T. Van De Meerakker, H. L. Bethlem, and G. Meijer. Taming molecular beams. *Nature Physics*, 4(8):595–602, 2008.

[195] D. H. Levy. Laser spectroscopy of cold gas-phase molecules. *Annual Review of Physical Chemistry*, 31(1):197–225, 1980.

[196] Y. Yamakita, S. R. Procter, A. L. Goodgame, T. P. Softley, and F. Merkt. Deflection and deceleration of hydrogen rydberg molecules in inhomogeneous electric fields. *The Journal of chemical physics*, 121(3):1419–1431, 2004.

[197] C. Seiler, S. D. Hogan, and F. Merkt. Trapping cold molecular hydrogen. *Physical Chemistry Chemical Physics*, 13(42):19000–19012, 2011.

[198] E. Narevicius, A. Libson, C. G. Parthey, I. Chavez, J. Narevicius, U. Even, and M. G. Raizen. Stopping supersonic beams with a series of pulsed electromagnetic coils: an atomic coilgun. *Physical review letters*, 100(9):093003, 2008.

[199] J. D. Weinstein, T. Guillet, B. Friedrich, J. M. Doyle, et al. Magnetic trapping of calcium monohydride molecules at millikelvin temperatures. *Nature*, 395(6698):148–150, 1998.

[200] J. C. Flasher and R. C. Forrey. Cold collisions between argon atoms and hydrogen molecules. *Physical Review A*, 65(3):032710, 2002.

[201] A. Mack, T. K. Clark, R. C. Forrey, N. Balakrishnan, T-G. Lee, and P. C. Stancil. Cold he+ h 2 collisions near dissociation. *Physical Review A*, 74(5):052718, 2006.

[202] P. Barletta, J. Tennyson, and P. F. Barker. Creating ultracold molecules by collisions with ultracold rare-gas atoms in an optical trap. *Physical Review A*, 78(5):052707, 2008.

[203] P. Barletta. Comparative study of rare gas-h2 triatomic complexes. *The European Physical Journal D*, 53(1):33–40, 2009.

[204] F. A. Gianturco, T. Gonzalez-Lezana, G. Delgado-Barrio, and P. Villarreal. The binding of he4 and he3 to a hydrogen molecule: A computational study for ph2 and oh2. *The Journal of chemical physics*, 122(8):084308, 2005.

[205] A. Mosk, S. Kraft, M. Mudrich, K. Singer, W. Wohlleben, R. Grimm, and M. Weidemüller. Mixture of ultracold lithium and cesium atoms in an optical dipole trap. *Applied Physics B*, 73(8):791–799, 2001.

[206] P. Barletta, J. Tennyson, and P. F. Barker. Direct monte carlo simulation of the sympathetic cooling of trapped molecules by ultracold argon atoms. *New Journal of Physics*, 12(11):113002, 2010.

[207] R. W. Terhune, P. D. Maker, and A. K. Levine(Ed). *Lasers*, volume 2. Dekker, New York, 1968.

[208] J. A. Armstrong, N. Bloembergen, J. Ducuing, and P. S. Pershan. Interactions between light waves in a nonlinear dielectric. *Physical Review*, 127(6):1918, 1962.

[209] R. W. Minck, R. W. Terhune, and C. C. Wang. Nonlinear optics. *Applied optics*, 5(10):1595–1612, 1966.

[210] A. Yariv. *Introduction to optical electronics*. Holt, Rinehart and Winston, Inc., New York, NY, 1976.

[211] N. Bloembergen. *Nonlinear optics*. New York: Benjamin, 1965.

[212] P. Regnier. Application of coherent anti-stokes raman scattering to gas concentration measurements and to flow visualization. *ONERA, Technical Note*, (215):92320, 1973.

[213] P. R. Regnier, J-P. E. Taran, M. Lapp, and C. M. Penney. *Laser Raman gas diagnostics*. Plenum Press, Inc., New York, p. 87, 1974.

[214] H. Kogelnik and T. Li. Laser beams and resonators. *Applied Optics*, 5(10):1550–1567, 1966.

[215] G. Placzek. *In E. Marx, Ed., Handbuch der Radiologie*. Akademische Verlagsgesellschaft, Leipzig, 1934.

[216] R. H. Pantell and H. E. Puthoff. *Fundamentals of quantum electronics*. John Wiley & Sons, 1969.

[217] G. Hauchecorne, F. Kerherve, and G. Mayer. Mesure des interactions entre ondes lumineuses dans diverses substances. *Journal de physique*, 32(1):47–62, 1971.

[218] R. N. DeWitt, A. B. Harvey, and W. M. Tolles. Theoretical development of third-order susceptibility as related to coherent antistokes raman spectroscopy (cars). *Naval Research Lab. Report*, 1, 1976.

[219] W. F. Murphy, W. Holzer, and H. J. Bernstein. Gas phase raman intensities: A review of. *Applied Spectroscopy*, 23(3):211–218, 1969.

[220] D. L. Jeanmaire, M. R. Suchanski, and R. P. Van Duyne. Resonance raman spectroelectrochemistry. i. tetracyanoethylene anion radical. *Journal of the American Chemical Society*, 97(7):1699–1707, 1975.